Title
Engineered Microgel Technologies for Modulation and Assessment of Immune Response

Author
Archang, Maani Meshkin

Publication Date
2021

Peer reviewed|Thesis/dissertation

UNIVERSITY OF CALIFORNIA

Los Angeles

Engineered Microgel Technologies for Modulation and Assessment of Immune Response

A dissertation submitted in partial satisfaction of the

requirements for the degree Doctor of Philosophy

in Bioengineering

by

Maani Meshkin Archang

2021

ABSTRACT OF THE DISSERTATION

Engineered Microgel Technologies for Modulation and Assessment of Immune Response

by

Maani Meshkin Archang

Doctor of Philosophy in Bioengineering

University of California, Los Angeles 2021

Professor Dino Di Carlo, Chair

Advances in the field of immunology have created many avenues for the development of novel immunotherapies for conditions from autoimmune disorders and tissue defects to vaccine development. Immune system involvement in health maintenance is multifaceted and generally highly localized. Most of the recently developed treatments, however, are applied systemically which leads to hyperactivation or suppression of the immune system at non-target sites. Development of biomaterial scaffolds that can recruit relevant subclasses of the immune system cells and locally modify their phenotype in a controlled manner can reduce the side effects of immunotherapeutics and improve their efficacy.

For biomaterials to be successful as local immunomodulatory scaffolds, they should be biodegradable and biocompatible, evading the foreign body response, yet encourage rapid immune cell infiltration, by providing immediate macroporosity. They should also synergize with other developing therapeutics by providing a large cargo capacity and mechanism for tunable controlled release. Finally, such biomaterials should be injectable and have a long shelf-

life for ease of clinical application. Many biomaterials have been developed to possess these features; however, all fall short in one aspect or another.

Our group has previously developed a novel biomaterial, microporous annealed particle gels, an injectable hydrogel scaffold, that provides immediate porosity to enable cell infiltration and improved wound closure. Here I introduce two novel immunomodulatory hydrogels based on the MAP technology with their applications in tissue regeneration and vaccination. For the first hydrogel technology, I present data on incorporating a minor change in MAP, by crosslinking hydrogels with unnatural D-chirality peptides (D-MAP) which made MAP immunogenic, resulting in type 2 response with IL33 producing macrophages, leading to regenerative healing of the skin. Notably, I show that this response was dependent on the adaptive immunity, without use of immunomodulatory agents or growth factors, highlighting utility of biomaterials in regenerative healing through activation of adaptive immunity.

For the second hydrogel technology, I show that incorporation of antigens in the microfluidic fabrication of MAP (VaxMAP) can lead to a robust germinal center development and humoral response. Furthermore, by incorporation of polymeric nanoparticles carrying CpG ODN adjuvants in MAP, I was able to induce class switching of the antibodies to a T-helper 1 dependent isotype. Finally, I showed MAP's unique capability of inducing different immune responses to two antigens within one vaccination. Together, these studies showcase the utility of MAP in immunomodulatory applications ranging from tissue regeneration to vaccination.

At the other end of the spectrum for development of immunotherapeutics, is the in vitro study of immune cells for development of biologic immunotherapies, such as monoclonal antibodies. Phenotypic study of immune cells with single cell resolution is essential for development of such therapeutics. Microscale approaches to study antibody producing cells

(APCs) with single cell resolution have been developed but none provide a widely accessible method to isolate target cells at high throughput, and generally require complicated assay formats for phenotypic studies. As such, labor intensive, time consuming, and costly techniques such as hybridoma technology remain the mainstream methods for development of therapeutics.

Microgel technologies combined with microfluidic techniques hold promise to resolve these limitations. In the last chapter, I introduce the utility of a novel microparticle platform, nanovials, for performing plate-based secretion assays at single cell level. The nanovials are hydrogel-based cup shaped microparticles which play the role of nanoliter-sizes well plates and can be loaded with individual APCs to capture and assess antigen-specificity of their secreted antibodies. The nanovials are compatible with commercial fluorescence-assisted flowcytometry systems and can be used to sort APCs with a throughput of more than two million APCs in one day. The APCs are sorted alive and can be used for downstream work such as sequencing for antibody discovery, and further functional analysis for study of their biology.

The dissertation of Maani Meshkin Archang is approved.

Timothy J. Deming

Stephanie K. Seidlits

Philip O. Scumpia

Dino Di Carlo, Committee Chair

University of California, Los Angeles

2021

DEDICATION

To the memory of my beloved father.

TABLE OF CONTENTS

TABLE OF FIGURES

ACKNOWLEDGEMENTS

Chapter 2 in a reprint of the work Griffin DR, Archang MM, et al. Engineered adaptive immune response from a hydrogel scaffold imparts regenerative wound healing. Nature Materials, 2020. D.R.G., P.O.S., and T.S. conceived the experiments. D.R.G., W.M.W, E.S., M.M.A., and J.K. carried out microfluidic design and fabrication, and D.D.C. oversaw microfluidic design and fabrication. D.R.G., M.M.A., C.H.K., W.M.W, J.S.W., A.C.F., E.S., A.R., V.R., P.O.S. performed experiments. D.R.G., M.M.A., J.S.W., A.R., M.V.P., T.S. and P.O.S. analyzed and interpreted data. D.R.G., M.M.A., P.O.S., and T.S. wrote the manuscript. D.R.G. and M.M.A. contributed equally to this work.

Chapter 3 has sections from a work in preparation by Archang MM et al. titled Microporous annealed particle scaffolds as a novel vaccination platform, as well as sections from: Fang J, Koh J, et al. Injectable Drug-Releasing Microporous Annealed Particle Scaffolds for Treating Myocardial Infarction. Advanced Functional Materials, 2020.

Chapter 4 contains sections from a work in preparation by Archang MM et al. entitled Microporous annealed particle scaffolds as a novel vaccination platform. I would like to acknowledge Olivia Antao for her help performing the ELISA and flowcytometry assays, and Dino Di Carlo, Philip O Scumpia, and Jason Weinstein for leading the work as principal investigators.

Chapter 5 contains sections from the work by de Rutte, et al. titled Sorting single-cell microcarriers using commercial flow cytometer, submitted to SLAS at the time of this writing and the work by de Rutte, et al. titled Suspendable microcontainers for massively parallel single-cell functional analysis and sorting, in preparation as of the time of this writing.

ADDITIONAL ACKNOWLEDGEMENT

During my doctoral study at UCLA, many people have mentored and inspired me to whom I owe much gratitude. First, I'd like to thank my PhD advisor, Dr. Dino Di Carlo for being an amazing mentor. Dino has always provided me with the freedom and resources to pursue my ideas, while always providing invaluable guidance and support. I am very grateful to have had the opportunity to work in his lab.

I would like to thank my co-PI, Dr. Philip O. Scumpia, who has consistently pushed me to learn and think more critically of my work, as well as my thesis committee members Dr. Timothy Deming and Dr. Stephanie Seidlits for their advice and mentorship and allowing me to use their laboratory facilities.

I also want to thank Dr. Peter Butler and Dr. Tatyana Gurlo at the Larry Hillblom Islet Research Center for being amazing role models, so invested in the education of their trainees, and teaching me so much in being methodical in research.

Having Dino and Phil as my Co-PIs, and Dr. Peter Butler and Tatyana as mentors, has given me the best training I could ask for and allowed me to learn all aspects of multidisciplinary projects and think of engineering solutions to challenges of different fields. I am very grateful for the mentorship of all of you.

I also like to give a shout out to my other mentors, Dr. Hai Quan Mao, my mentor at Johns Hopkins University, Dr. Dottie Sherling, my mentor at Irvine Valley College, and Dr. David Dawson and Dr. Carlos Portera-Cailliau, my advisors at the UCLA medical scientist training program.

I would like to thank members of the Di Carlo Lab, Scumpia Lab, and Larry Hillblom Islet Research Center, who have taught me so much, have been great friends, and made the PhD

work more fun. I would like to acknowledge the support of the Medical Scientist Training Program T32 grant, as well as the Dermatology scientist training program T32 grant which have supported me in my MD and PhD studies, respectively.

I would like to thank my amazing family, especially my uncle, Rasoul Dorri, who supported me in my decision to leave medical school in Iran, and start over in the US, my aunt and uncle, Farzaneh and Masoud Akhavi, who offered their endless support when I moved here 10 years ago. They made it possible for me to pursue my dream career. Also, a big shout out to all my dear friends, especially Roozbeh, Hirbod, Maryam, Soheil, Amir, Negar, Mohammad, Tina, Ashkan, Paniz, Nariman, Shayan, and Peter, and many others for bringing so much fun and love into my life. And a special thank you to two special people who helped me so much through the toughest time of my life while caring for my dad, my amazing mom, and Mohammad Malekzadeh, my great friend, and the most selfless person I have had the pleasure of knowing.

I owe a great debt of gratitude to my late father, who raised me single handedly, always gave me his unconditional love and was an amazing role model and a source of inspiration. I love you so much and miss you every day.

Finally, I would like to thank my amazing wife, Hana. I am inspired by all the obstacles you have overcome in your life and all you accomplish year after year. I would not be where I am today if it wasn't for your endless love, support, patience, and selflessness. I feel so lucky to have you as my partner and best friend, and I love you more than everything in the world combined, bacon included!

VITA

EDUCATION

University of California Los Angeles, David Geffen School of Medicine — Los Angeles, CA
MD-PhD, Physician Scientist Training Program — Expected May 20

Johns Hopkins University — Baltimore, MD
B.S. in Materials Science & Engineering/Biomaterials Track — May 2014
Graduated with General and Departmental Honors, Dean's List Every Semester, GPA: 3.92

Irvine Valley College/Saddleback College — Irvine, CA
Graduated *summa cum laude*, Dean's List Every Semester, GPA: 4.0 — August 2010 – May 2012

RESEARCH APPOINTMENTS

University of California Los Angeles, Los Angeles, CA
PhD Student, Di Carlo Lab and Scumpia Lab, Departments of Bioengineering and Medicine — 2018 – Present
Researcher, Larry L. Hillblom Islet Research Center, Department of Medicine — 2019 – Present
Researcher, Wu Lab, Department of Molecular and Medical Pharmacology — 2016 – 2017

Johns Hopkins University, Baltimore, MD
Researcher, Radiation Oncology Department, Sidney Kimmel Comprehensive Cancer Center — 2014 – 2015
Researcher, Mao Lab, Institute for NanoBioTechnology — 2012 – 2015

School of Medicine, Tehran University of Medical Sciences, Tehran, Iran
Research Assistant, Dehpour Research Group, Neuro-psycho-pharmacodynamics Institute — 2008 – 2010

PUBLICATIONS AND PATENTS

***** Equal contribution as co-first authors

In preparation

Archang MM*, Antao O*, Eichenbaum J, Weinstein J, Di Carlo D, Scumpia P. Microporous annealed particle gels as a novel vaccination platform.

de Rutte J*, Dimatteo R*, Koo D, Zhu S, **Archang MM**, Eichenbaum J, Damoiseaux R, Di Carlo D. Massively parallel encapsulation of single cells with structured microparticles and secretion-based flow sorting.

Under review

de Rutte J*, Dimatteo R*, Zhu S, **Archang MM**, Di Carlo D. Sorting single-cell microcarriers using commercial flow cytometers. SLAS. Submitted May 2021.

Di Carlo D, de Rutte J, Dimatteo R, **Archang MM**, Damoiseaux R, Koo D. Methods of using shaped particles in flow cytometers for assays on B cells and T cells. U.S. Patent Application Serial No. 63/186,719

Published

van Zee M, de Rutte J, Rumyan R, Williamson C, Burnes T, Radakovits R, Eugenio AS, Badih S, Lee DH, **Archang MM**, Di Carlo D. High-throughput selection of microalgae based on biomass accumulation rates in production environments using PicoShell Particles. bioRxiv, 2021.

Griffin DR*****, **Archang MM***, Weaver WM, Weinstein JS, Ruccia A, Feng A, Sideris E, Koh J, Di Carlo D, Segura T, Scumpia PO. Engineered adaptive immune response from a hydrogel scaffold imparts regenerative wound healing. Nature Materials, 2020.

Fang J, Koh J, Fang Q, Qiu H, **Archang MM**, Hasani-Sadrabadi MM, Miwa H, Zhong X, Sievers R, Gao DW, Lee R, Di Carlo D, Li S. Injectable drug-releasing microporous annealed particle scaffolds for treating myocardial infarction. Advanced Functional Materials, 2020.

Rahmani H*****, **Archang MM***, Jamali B*****, Forghani M, Ambrus A, Ramalingam D, Sun Z, Scumpia PO, Coller H, Babakhani A. Towards a machine-learning-assisted dielectric sensing platform for point-of-care wound monitoring. IEEE Sensors Letters, 2020.

Koh J, Griffin DR, **Archang MM**, Feng A, Horn T, Zalazar D, Margolis M, Haddadi H, Segura T, Scumpia PO, Di Carlo D. Enhanced function of a stem cell niche through microporous annealed particle scaffolds. Small, 2019.

Hu J, Schokrpur S, **Archang MM**, Hermann K, Sharrow A, Khanna P, Novak J, Signoretti S, Bhatt RS, Knudsen BS, Xu H, Wu L. A non-integrating lentiviral approach overcomes Cas9-induced immune rejection to establish an immunocompetent metastatic renal cancer model. Molecular Therapy-Methods & Clinical Development, 2018.

Luis Santos J, Ren Y, Vandermark J, **Archang MM**, Williford JM, Liu HW, Lee J, Wang TH, Mao HQ. Continuous production of discrete plasmid DNA-polycation nanoparticles using flash nanocomplexation. Small, 2016.

Williford JM*****, **Archang MM***, Minn I, Ren Y, Wo M, Vandermark J, Fisher PB, Pomper MG, Mao HQ. Critical length of PEG grafts on LPEI/DNA nanoparticles for efficient in vivo delivery. ACS Biomaterials Science and Engineering, 2016.

Archang MM, Mao HQ, Minn I, Pomper M, Ren Y, Santos JL, Williford JM. Compositions of nucleic acid-containing nanoparticles for in vivo delivery. US 20160331845 A1. 2016. US Patent Office.

Williford JM, Wu J, Ren Y, **Archang MM**, Leong KW, Mao HQ. Recent advances in nanoparticle-mediated siRNA delivery. Annual Review of Biomedical Engineering, 2014.

CONFERENCE PROCEEDINGS AND POSTER PRESENTATIONS

Archang MM, Griffin DR, Weaver WM, Weinstein JS, Ruccia A, Feng AC, Sideris E, Koh J, Segura T, Di Carlo D, Scumpia PO. Microfluidically-fabricated MAP hydrogel crosslinked with D-chirality peptides induces skin regeneration by activating adaptive immunity. UCLA Department of Medicine Research Day, 2019.

Archang MM, Griffin DR, Weaver WM, Weinstein JS, Ruccia A, Feng A, Sideris E, Koh J, Di Carlo D, Segura T, Scumpia PO. Activating an adaptive immune response from a hydrogel scaffold imparts regenerative wound healing. MicroTAS, 2019.

Archang MM, Koh J, Di Carlo D. Engineering microporous annealed particle (MAP) hydrogels as novel immunotherapy platform for melanoma. Micro and Nanotechnology in Medicine, 2018.

Archang MM, Williford JM, Ren Y, Mao HQ. Probing the shape-effect on in vivo trafficking and transfection efficiency of polymer/DNA micellar nanoparticles. INBT Symposium, Institute for NanoBioTechnology, Johns Hopkins University, 2014.

Archang MM, Williford JM, Ren Y, Mao HQ. Probing the shape-effect on in vivo trafficking of polymer/DNA micellar nanoparticles. 2014. Provost's Undergraduate Research Award Poster Session. Johns Hopkins University.

Williford JM, Ren Y, Qu W, **Archang MM**, Huang K, Wei Z, Luijten E, and Mao HQ. Experimental and computational approaches to probe the mechanism of shape control in PEG–polycation/DNA micelle assembly. Controlled Release Society, 2014.

FELLOWSHIPS AND AWARDS

Dermatology Scientist Training Program T32 Grant, UCLA	2018 – 2021
Medical Scientist Training Program T32 Grant, UCLA	2015 – Present
Senior Design Presentation Award, Johns Hopkins University	2014
The Senior Design Engineering Award, Johns Hopkins University	2014
Provost's Undergraduate Research Awards, Johns Hopkins University	2013
The John W. & Mary Lou Ross Scholarship, Johns Hopkins University	2013 – 2014
Bloomberg Award, Johns Hopkins University	2013 – 2014
Saddleback Kiwanis Scholarship, Irvine Valley College	2012
Selected Regents Scholar, UCLA	2012

Chapter 1. Biomaterials for immunomodulation

1.1. Introduction

Immune system dysregulation is involved in most pathologies. Our growing understanding of the formation of immunological memory against infections, as well as the role of the immune system in processes such as tissue regeneration, cancer, and autoimmune disorders have led to opening many avenues for development of immunotherapeutic modalities by either activating or suppressing certain aspects of the immune response.

Many such modalities have been developed in recent years. One great example is the development of checkpoint blockers for treatment of cancer which has led to improved survival in aggressive diseases such as melanoma.[1] However, immunotherapeutic approaches are mostly delivered systemically, and are thus limited by the side effects of the interventions, due to widespread hyperactivation or suppression of the immune system, leading to autoimmune disorders, or increased risk of cancer and infections, respectively.[2–4]

Cells of the immune system, unlike most other tissues, are highly mobile, and can rapidly up or downregulate their chemokine receptors, moving from lymphoid tissues to the site of injury or infection and vice versa, with precision. The cytokines and many effector molecules secreted by immune cells also have short half-lives in the extracellular fluid, limiting their function to the vicinity of where the activated immune cells were present. These features generally enable the immune system to present a strong response at the site of injury, while saving the rest of the body from the harmful effects of the immune response. Biomaterial niches for local delivery of the immunomodulatory molecules can improve therapeutic efficacy by increasing the availability of the therapeutic agent at the target site, while decreasing the undesirable systemic effects. Biomaterial scaffolds can also be designed to recruit appropriate

subgroups of immune cells to form a temporary lymphoid organ and modulate the function of the immune system similarly to the physiologic immune response.

1.2. Design criteria for immunomodulatory biomaterial scaffolds

When designing material for immunomodulation certain criteria should be considered, including biocompatibility and biodegradability, porosity, route of delivery, and if delivery of a cargo is intended, release kinetics and cargo capacity (**Figure 1-1a**). The intended application of biomaterial will impact the relative importance of each of these factors.

1.2.1. Biocompatibility

Biomaterials need to be biocompatible to support livelihood and function of cells and avoid a strong immune response that can lead to tissue destruction or a foreign body response that can lead to fibrosis, isolating the biomaterial and rendering it ineffective. While some level of immunogenicity can prove helpful for biomaterial designed for vaccination, for applications in tissue regeneration or induction of immune tolerance, biocompatibility and low immunogenicity become much more critical.

Extracellular matrix (ECM) components inherently possess physical and chemical characteristics as well as cell binding motifs and growth factor binding sites, that enhance their biocompatibility and support of tissue ingrowth and function.[5] As such decellularized ECMs, or their components such as collagen and hyaluronic acid, have been used for fabrication of immunomodulatory scaffolds.[5] Other natural polymers such as alginate and silk, and synthetic polymers such as polyethylene glycol, and poly-lactide-co-glycolide have many similarities to extracellular matrix components, are generally considered biocompatible, and with varying degrees of modifications, such as addition of cell adhesion peptides, or adjustments to their

degradability, have been used to make scaffolds for tissue regeneration and immunomodulation as well.[6–8]

Beside chemical properties that enable cell adhesion, growth factor binding, and prevent major deposition of complement proteins and such processes, the biocompatibility also depends on the physical properties of the material which can be adjusted in the fabrication process.[9] Cells like to the anchor onto ECM molecules, to reorganize their cytoskeleton, and polarize their cytoplasm. A mechanically robust scaffold with high enough microscale stiffness can provide cells with such an environment and support their movement, growth, and division. On the other hand, material with a higher macroscale stiffness compared to the tissue can cause microinjuries when the tissue moves, causing inflammation and tissue destruction. Fabrication processes that can provide different micro- and macro-scale stiffnesses will enhance the material's biocompatibility. Furthermore, cells of the immune system are specifically sensitive to mechanical cues[10] which makes tunability of material stiffness especially important for immunomodulatory applications. Surface topography can also determine the response of immune cells to the material and have been used to alter the immune response to the material by inducing a macrophage phenotypic differentiation.[11]

1.2.2. Biodegradability

Material designed for the purpose of injection or implantation in body for immunomodulation should be biodegradable, to avoid the need for surgical removal of the therapeutic material after the pathology is resolved. Degradation can happen via hydrolysis or other chemical reactions like thiol exchange, enzymatic digestion, dissociation, or other stimuli. The extracellular environment in large mammals like humans is more degrading than small laboratory animals. A biomaterial that has been proven highly degradable in small laboratory

animals, might not last long enough in the larger mammals to achieve its purpose. Furthermore, degradation rate of the material can have a large impact on its other properties, including porosity, and cargo capacity and release kinetics. As such, the ability to tune the degradability, with minimal impact on its other properties, can be critical for successful clinical translation of a biomaterial.

All byproducts of the material degradation should also be biocompatible and readily removable from the body. For example, smaller polymer chains resulting from degradation of PLGA scaffolds can be excreted by the kidneys without causing toxicity to any organ systems.[12] However, formation of glycolic acid and lactic acid groups at the degradation site can lead to a temporary decrease in the pH of the microenvironment of an implanted scaffold.[13] This can be exacerbated if the scaffold is not fully vascularized to wash away the acidity and can interfere with the livelihood and function of infiltrating cells.

1.2.3. Mode of delivery

Injectable biomaterials are preferable for clinical use due to the ease of application. Pre-gel fluids, shear thinning material, and material with shape memory can be delivered via injections and are preferred for ease of clinical application.[14,15] Pre-formed scaffolds are beneficial for ease of fabrication and customization, as multi-step modifications can be applied to them to achieve more complex physical properties and chemical functionalities, without constraints of the physiologic environment and safety concerns. However, preformed scaffolds have to be implanted, which can limit the clinical translation of these biomaterial technologies. Depending on the significance of the pathology and target location, especially for less common applications, implantable material can still be desirable.

1.2.4. Porosity

For systems where immune cell infiltration and interaction with the scaffold is intended, such as material for tissue regeneration or formation of a de novo lymphoid tissue for vaccination, microporosity is necessary. Porous scaffolds have shown higher efficacy in recruiting and activating DCs for immunomodulation compared to non-porous scaffolds with the same chemical composition, containing the same bioactive agents.[16] However, porosity can be less important and even undesirable for certain applications such as injecting a material directly in a tumor simply as a delivery depot.

Different techniques have been developed for fabrication of porous scaffolds for immunomodulation. Adding porogens to the pre-gel solution, can exclude biomaterial from the spaces occupied by the porogen. Removing the porogen after gelation, can then leave a network of interconnected pores within the scaffold, as opposed to a bulk gel (**Figure 1-1b-c**). Salt and ice crystals and rapidly degradable microparticles, have been used as porogens.[16–18] Electrospinning is another technique used to produce macroporous scaffolds.[19,20] While the scaffolds produced with these techniques have the porosity to enable rapid immune cell infiltration, they have to be formed before implantation, and are not injectable. Which limits their clinical use, especially for widespread applications such as vaccination. Furthermore, their nano- and micro-porosity is tightly associated with their mechanical robustness, which reduces their versatility and ability to perform as a delivery depot (**Figure 1-1a**).

Mesoporous silica rods (MSR) are another porous scaffold made of nanometer sized needle like silica structures that when diluted are injectable (**Figure 1-1d**).[21] After injection, their carrier fluid diffuses away, leaving behind a porous scaffold. But these inorganic structures have a few limitations, like questionable degradation and excretion pathways, questionable versatility

as a delivery depot, as well as high immunogenicity which limits them to applications in vaccination (**Figure 1-1a**).[22]

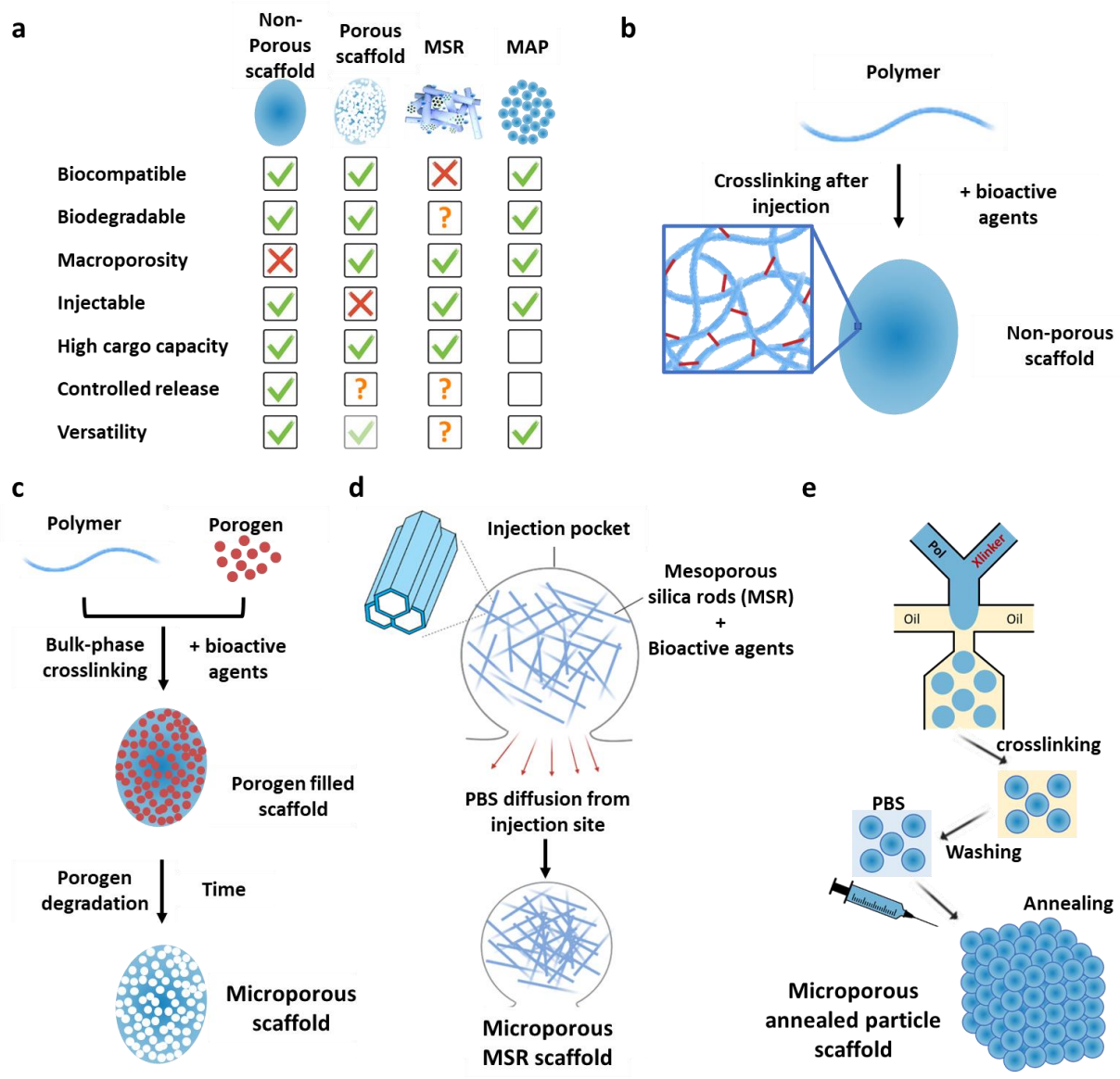

Figure 1-1 Comparison of biomaterial scaffolds used for immunomodulatory applications. a) Features of each biomaterial platform as it pertains to its applicability to immunomodulation. **b-e)** fabrication method and application of non-porous polymeric scaffolds (b), microporous polymeric scaffolds (c), microporous mesoporous silica rods (d), and microporous annealed particle gels (e).

1.2.5. Cargo capacity and release kinetics

The growing number of immunomodulatory agents approved for clinical use, ties the success of a biomaterial scaffold as an immunomodulatory platform to its versatility as a

sustained delivery system. Biomaterial scaffolds should provide a sufficiently high cargo capacity and a mechanism for adjustable sustained delivery of immunomodulatory molecules.[23] This can be challenging, especially for porous scaffolds, due to their high void volume and constraints in their fabrication process. Loading enough cargo in a scaffold can also be challenging if the physical properties of the biomaterial and cargo are different, leading to precipitation at high cargo concentration or even necessitating compartmentalization within the scaffold.

There are several methods for incorporating molecules into biomaterial for prolonged delivery. Immunomodulatory agents can be either physically trapped inside the material if the nanopores in between biomaterial molecules are small enough or immobilized via chemical conjugation or affinity binding. Affinity binding is the simplest method; however, it limits the applicability of the material to cargo with matching physical properties. Click conjugation methods also make it easy to chemically bind cargo to biomaterial with free functional groups, without the need for complicated chemical modification of the polymer.[24] However, a chemical conjugation can change the three-dimensional structure of many immunomodulatory proteins which are critical for serving their function. A large body of literature exists on nano and microparticles for controlled release of agents with different properties.[25] For example, PLGA nanoparticles have been extensively studied for controlled delivery of small hydrophilic and hydrophobic molecules by physically entrapping the cargo within PLA crystals, and positively charged polymeric nanoparticles have been studied for delivery of negatively charged nucleic acids.[26,27] Biomaterials that can incorporate such systems can synergize with the advancements made in those technologies. Finally, for material intended for delivery of therapeutic agents, methods used in preparation can impact clinical translatability. For example, the organic solvents

used in preparation of PLGA nanoparticles can change the three-dimensional structure of proteins, by changing the thermodynamics of protein folding, negatively impacting their functionality.

1.2.6. Versatility

Versatile immunomodulatory scaffolds have a higher chance of translation and success in clinic. By versatility I am referring to the ability to tune each of the criteria mentioned above, independent of the other ones, as well as the ability to incorporate additional technologies into the material without major changes to the structure or fabrication process. To explain this, I will use mesoporous silica rods as an example. Coating MSRs with PEG or LPEI layers has been used for delivery of immunomodulatory agents such as GM-CSF and CpG ODN. However, these coatings have shown to significantly reduce the degradation of the material. So, for MSRs the degradation and the cargo capacity and release kinetics are tightly interconnected, and cannot be tuned individually, which reduces the versatility of the system for translation into humans.

1.3. Biomaterial scaffolds for tissue regeneration

Most of the research in using immunomodulatory biomaterials for tissue engineering has targeted the cells of the innate immune system, mainly macrophages.[9] Identification of the M2 macrophage phenotype, which functions to suppress damaging immune processes, and promote wound healing, tissue repair, and generation of new blood vessels, has led to identification of multiple therapeutic targets to enhance this phenotype to promote tissue regeneration. M2 macrophages are activated by cytokines such as IL-4, IL-13, and IL-10, and produce high levels of IL-10 and TGF-beta.[28] These molecules have been incorporated into biomaterial scaffolds and studied to promote tissue regeneration. For example, injectable silk hydrogels have been shown to support the function of pancreatic islets, and when loaded with IL-4 and dexamethasone

promoted a strong macrophage polarization towards M2 phenotype, which can provide an immunosuppressive environment for implants, and promote regeneration of tissue and blood vessels.[6] Alginate hydrogels, loaded with CSF-1 and IL-4 have also been shows to strongly increase the M2-macrophage markers, improve wound healing in ischemic wound healing model, and enhance cardiac function in myocardial infarction.[29]

More recently, scaffolds derived from bone and cardiac tissue extracellular matrix were applied to muscle defects and elicited functional muscle regeneration in mice through inducing an immune response mediated by mTOR/Rictor dependent T helper 2 pathway that guided an IL-4 dependent M2 macrophage polarization.[30] Importantly, the muscle regeneration was absent in the animals deficient in the cells of adaptive immunity, and was induced without addition of cytokines or other immunomodulatory molecules to the tissue derived scaffolds. While most of the research in tissue regeneration trough immunomodulation has been focused on the cells of the innate immune system, this work opened a new avenue for application of immunomodulatory biomaterials in tissue regeneration by controlling the cells of the adaptive immunity.

1.4. Biomaterial scaffolds for vaccination

Porous scaffolds can be used to deliver antigens along with pathogen associated molecular patterns, or other immunomodulatory molecules to mount a humoral or cellular response against the antigen. Scaffolds can also be directly injected inside a tumor to deliver immunomodulatory cues with or without chemotherapeutic agents and allow the immune system to overcome the immunosuppressive environment of a tumor and mount a response against unknown tumor antigens. Mesoporous silica rod scaffolds have been used to deliver GnRH-decapeptide and successfully led to inducing a humoral response against GnRH, which lasted for 12 months, leading to higher antibody titers than alum vaccine formulations.[31]

Known tumor antigens, or lysates of biopsied tumors can be incorporated into local scaffolds with adjuvants to recruit and activate antigen presenting cells, that will then travel to draining lymphoid tissues to mount a response or to form a lymph node within the scaffold. Prefabricated porous PLGA and alginate scaffolds have been used as cancer vaccines in pre-clinical tumor models with promising results.[16,32] These implantable scaffolds spiked with GM-CSF and CpG oligodeoxynucleotides and a tumor lysate were able to recruit and activate dendritic cells leading to induction of tumor reactive CD8+ cytotoxic T cells in multiple murine tumor models including B16-F10 melanoma. Injectable mesoporous silica rod scaffolds have shown similar success in B16-F10 and TC1 tumor models.

1.5. Microporous annealed particle gels as an immunomodulatory biomaterial

Our lab has developed a fundamentally new biomaterial, recently published in Nature Materials[33], that satisfies these characteristics. The MAP scaffold technology begins as an aqueous slurry of millions of microfluidically fabricated microgel building blocks within a syringe applicator (**Figure 1-1e**). Once applied to tissue these spherical building blocks (~100μm in diameter) are triggered to anneal to the surrounding microgels and the tissue bed to form a mechanically robust lattice-like structure with pores consisting of the interconnected void spaces between packed spherical particles[33]. Prior to annealing, the concentrated solution of microgel building blocks is flowable, which enables delivery via subcutaneous injection. The unique geometric composition of the MAP scaffold enables it to provide different micro and macroscale stiffness. Cells can attach the relatively stiff surfaces of particles and anchor their cytoskeleton, while the low macroscale stiffness of the scaffold prevents tissue damage by adjusting its shape as the surrounding tissue moves. The engineered porosity of the scaffold accelerates infiltration of blood vessels and decreases scar forming fibrosis within the scaffold[33]. Microscale porosity

and low macroscale stiffness also acts to prevent a foreign body response to the scaffold, which further reduces the fibrotic response and encapsulation of the material, which is expected to extend the delivery window for immunomodulatory molecules[33]. The surface of the MAP gel can be functionalized to covalently bind antigens or immunomodulatory molecules. We also can tune the degradation of the MAP gel using peptide crosslinkers that are substrates for matrix metallopeptidases secreted by immune cells, potentially enabling controlled release for any molecule that can be effectively trapped inside the microgel polymer mesh. These features make the MAP gel technology an attractive platform for local modulation of the immune response. In the following three chapters I will discuss the application of this technology as an immunomodulatory platform for skin regenerative healing as well as vaccination.

Chapter 2. Activating an adaptive immune response from a hydrogel scaffold to induce regenerative wound healing

2.1. Introduction

The goal of regenerative medicine is to restore tissue function back to physiological activity. For biomaterial scaffolds, the optimal strategy to achieve this requires balancing material degradation with tissue regrowth. Clinical/patient factors contribute to a wide variation in chemical and physical parameters in situ, which makes striking a degradative-regenerative balance particularly difficult. Our recent development of a flowable, granular biomaterial, known as MAP (Microporous Annealed Particle) gel, provides a new approach to make the balance more feasible[33]. The MAP gel is composed of randomly packed microsphere building blocks with a continuous network of interconnected micrometer-scale void spaces that allows for the infiltration of surrounding tissue without the prerequisite degradation of material[33,34]. This unique design resulted in improved tissue closure and improved vascularization relative to a nanoporous (but chemical formulation equivalent) hydrogel in a cutaneous wound model[33].

Mechanical support to the growing tissue by scaffolds is inherently impacted by the degradation rate of the scaffold[35]. For MAP scaffolds, degradation leads to a slow loss of porosity and reduced tissue ingrowth prior to dissolution. We hypothesized that slowing the degradation rate of MAP scaffolds would maintain the porosity and influence both wound closure rate and regenerated tissue quality.

Changing the chirality of peptide moieties leads to a diminished degradation rate by endogenously present enzymes[36,37]. The use of chirality was made more attractive by the fact that polypeptides of D-enantiomeric amino acids are do not typically elicit a robust immune response and are considered poorly immunogenic[37]. Previously, we have used amino acid chirality to tune

the proteolytic rate of peptide nanocapsules for controlled release of encapsulated growth factors[36]. Therefore, we chose to use an analogous approach to slow the enzymatic degradation of our MAP scaffold by switching the chirality of the peptide crosslinker (e.g., L- to D-chirality at the site of matrix metalloprotease (MMP)-mediated bond cleavage). We hypothesized that this approach would maintain the hydrogel micro-environment (e.g., charge-based interactions and hydrophobicity), while increasing the long-term hydrogel integrity to allow full infiltration of cells, thus providing a greater integration of the entire construct with the host tissue.

In the current study, we investigate how MAP hydrogels cross-linked with either D- or L-amino acid crosslinking peptides affect wound healing and skin regenerative responses using murine wound models. We provide evidence that activation of specific immune responses by the D-amino acid crosslinked MAP hydrogels elicit skin regeneration. While immunity undoubtedly activates the foreign body response and eventual fibrosis of some implanted biomaterials[38,39], the activation of the correct immune responses may enhance the regenerative ability of a biomaterial[30,40].

2.2. Results and discussion

2.2.1. D-chiral crosslinker peptides slow MAP degradation in vitro.

We first used enantiomeric chemistry to change degradation rate without changing the initial material properties (e.g. hydrophobicity, mesh size, and charge) of the hydrogel[36]. All amino acids at the site of enzymatic cleavage for the MMP-degradable peptide were changed to D-amino acids (Ac-GCRDGPQ_DG$I_D$$W_D$GQDRCG-NH2, D-peptide). We matched the stiffness (i.e. storage modulus) by rheology of both the D-peptide MAP (D-MAP) and L-peptide (L-MAP) formulations to that used in our previous MAP-based cutaneous application (~500Pa; **Figure 2-1a**). After formulation optimization, we generated the microsphere particles using a

previously published microfluidic technique[33]. Following application of collagenase I to L-MAP, D-MAP or a 50% mixture of D-MAP and L-MAP (1:1 L/D-MAP), the L-MAP hydrogel degraded within minutes, while the degradation of D-MAP by itself or within a mixture with L-MAP was minimal even after an 1 hour (**Figure 2-2b** and **Figure A-1**).

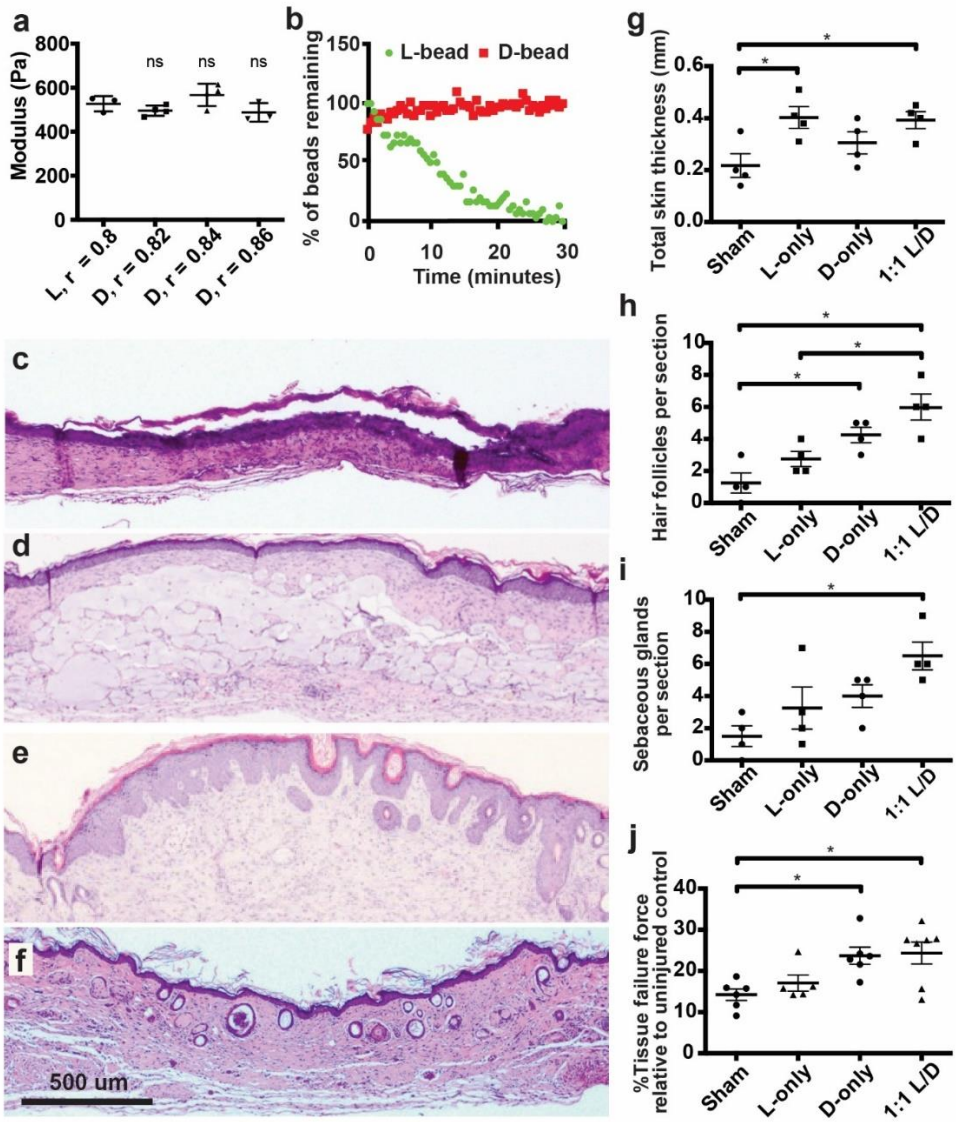

Figure 2-1 Presence of D-chiral crosslinker peptides decreases hydrogel degradation in vitro but enhances hydrogel degradation in SKH1 hairless mice. a) Rheological characterization of MAP hydrogels composed of L or D-peptide crosslinked microgels. The r-ratio (ratio of -SH to -VS) used to form the microgels was changed to arrive at the same storage modulus for both L and D MAP scaffolds. NS represents a no statistical significance between the L MAP scaffold to the D-MAP scaffold indicated using a two-tailed student t-test. **b**) Fabricated L or D hydrogels were tested for *in vitro* enzymolysis behavior through exposure to a solution of collagenase I (5U/mL). **c-f**) Representative low power view of

H&E sections from healed skin 21 days after splinted excisional wounding from a Sham (c), L-MAP (d), D-MAP (e), and 1:1 mixture of L-MAP and D-MAP treated wound in SKH1 mice (f). **g-i**) Histologic quantification of dermal thickness including gels (in mm), hair follicles, sebaceous glands. Each point represents average of 2 sections from 2 separate slides of one wound. Each data point represents one animal, and all analysis is by one-way ANOVA (respective F-values (3,12): 4.448, 10.89, 5.074. **j**) 28 days after incisional, unsplinted wounds were created, healed wounds that were treated without or with different hydrogels were tested against unwounded skin in the same mouse. Tensile strength was evaluated by tensiometry and reported as a percentage of the tensile strength of the scar tissue when compared to the normal skin of the same mouse. Each data point represents average of two measurement from one wound, separate from wounds used in b-i with analysis by one-way ANOVA (F-value (3, 20): 5.400). Data is plotted as a scatter plot showing the mean and standard deviation. *, **, *** represent statistical significance by ANOVA using the Tukey multiple comparisons test.

2.2.2. D-chiral crosslinker peptides enhance MAP degradation in vivo.

We next examined how D-MAP compares to L-MAP *in vivo* in a murine splinted excisional wound model[33,41]. We did not find any difference in wound closure rate, or any increased erythema or gross signs of inflammation in 6wounds treated with D-MAP, L-MAP, or a 1:1 mixture of L/D MAP any time after treatment (shown Day 3 and Day 6 after wounding, **Figure A-2a**). When comparing wound closure to sham treatment (no hydrogel), we found that 1:1 mixture of L/D MAP induced more rapid wound closure (assessed on Day 9 after wounding) than sham (**Figure A-2b**), similar to previous results with L-MAP hydrogel[33].

Since no differences in wound closure results were noted, we next examined whether the degradation of hydrogels containing D amino acid cross-linkers was slowed *in vivo* by examining excised tissue 21 days after the wound was completely healed. Unexpectedly, histological sections of wounds treated with D-MAP or a 1:1 L/D-MAP hydrogel mixture displayed minimal to no hydrogel persistence 21 days after wounding, nearing levels seen in mice not treated with hydrogel (Sham), whereas wounds treated with L-MAP hydrogel displayed large amounts of hydrogel remaining (**Figure 2-1c-f**).

2.2.3. D-MAP hydrogels impart tissue regenerative properties.

Of note, initial examination of histologic sections of D-MAP and 1:1 L/D-MAP displayed a much different overall appearance than that of healed sham- or L-MAP-treated wounds. Previous reports suggest that, unlike large excisional wounds in adult mice (wounds larger than 1x1 cm) that result in significant regenerative healing with wound induced hair neogenesis (WIHN)[42–44], wounds smaller than 1x1cm in mice, like the punch biopsies performed in our studies, typically heal without regeneration of new hair and fat and, instead, form scars[43,45,46]. Despite these reports, when the correct regenerative cues are provided from wound fibroblasts, through transgenic activation of specific Hedgehog signals, small wounds can regenerate[47]. Consistent with these results, histological examination of 4-mm excisional splinted wounds in mice that did not receive hydrogel (sham) displayed the typical appearance of scar tissue with a flattened epidermis, a thinned dermis with horizontally oriented collagen bundles, vertically-oriented blood vessels, and lack of hair follicles and sebaceous glands (**Figure 2-1c, g-i**). Tissue from mice treated with L-MAP hydrogel displayed a similar appearance, but with thicker overall tissue compared to sham wounds, due to the substantial residual L-MAP hydrogels (**Figure 2-1d, g**). Within the dermis surrounding the hydrogel, fibroblasts secreting collagen/extracellular matrix and blood vessels formed between the hydrogel microparticles (**Figure 2-1d**). Only rare hair follicles and associated sebaceous glands were observed in the wound areas (**Figure 2-1d, h-i**). Remarkably, examination of histological sections of the D-MAP- or 1:1 L/D-MAP-treated tissue revealed a *de novo* regenerated appearance. The overlying epidermis often displayed physiological undulation, while numerous immature-appearing hair follicles were seen spanning the length of the healed full thickness injury (**Figure 2-1e-i**). Samples treated with D-MAP or 1:1 L/D-MAP also displayed increased skin thickness despite

less hydrogel remaining in these samples (**Figure 2-1f**). Many samples also displayed epidermal cyst formation. In samples that displayed residual hydrogel, hair follicles were apparent directly overlying the degrading MAP hydrogel particles (**Figure A-2c**). The presence of hair follicles in SKH1 mice was suggestive of embryonic-like tissue regeneration, a phenomenon not often observed in the murine small wound model.

To further quantify tissue regeneration, we next performed tensile strength testing on unsplinted incisional wounds in SKH1 mice using a modified literature protocol[48]. We found that scar tissue from sham wounds revealed tensile strength that was approximately 15% of unwounded skin from the same animal (**Figure 2-1i**). While treatment of wounds with L-MAP hydrogel did not result in a significant increase in tissue tensile strength, treatment with either D or L/D MAP resulted in an ~80% improvement in tensile strength (**Figure 2-1j**).

2.2.4. Hair follicles in D-MAP-treated wounds are neogenic.

We next repeated wound healing experiments in B6 mice to investigate if the regenerative phenomenon observed in D-MAP treated wounds was similar to WIHN. We chose sham as control and D-MAP as a treatment method that showed evidence of regeneration in SKH1 mice. Similar to the sham and L-MAP treated wounds in SKH1 mice, the B6 mice wounds without hydrogel (sham) displayed the typical scar appearance by H&E and Masson Trichrome staining (**Figure 2-2a, c, e**). In contrast, histological sections of the D-MAP treated tissue revealed clear signs of WIHN. As in SKH1 mice, D-MAP treated B6 mice wounds displayed undulations and numerous epidermal cysts under the epidermis, while the dermis was thicker. Importantly, many neogenic hair follicles developed in the wound (**Figure 2-2b, d, f**). The neogenic hair follicles were in early anagen phases with immature appearance, yet many of them already had formed new sebaceous glands (**Figure 2-2b**) and featured prominent $SOX9^{+}$

bulge stem cell region (**Figure 2-2j**). In several instances, neogenic hair follicles were physically connected to epidermal cysts (morphology not expected from pre-existing follicles). This suggests that in D-MAP treated wounds, epidermal cysts can be the initiation sites for *de novo* morphogenesis for at least some of the neogenic hair follicles (**Figure 2-2h**). Masson trichrome staining confirmed the presence of neogenic hair follicles within the collagen matrix of the wound bed (Fig 2b, f). Furthermore, regenerating day 18 D-MAP treated wounds with neogenic hair follicles lacked $PLIN^+$ dermal adipocytes (**Figure 2-2h**), which is consistent with slower regeneration of neogenic adipocytes that occurs four weeks after wounding in the large wound-induced WIHN [49,50]. Thus, addition of D-MAP to normally non-regenerating 4-mm excisional wounds activates hair follicle neogenesis.

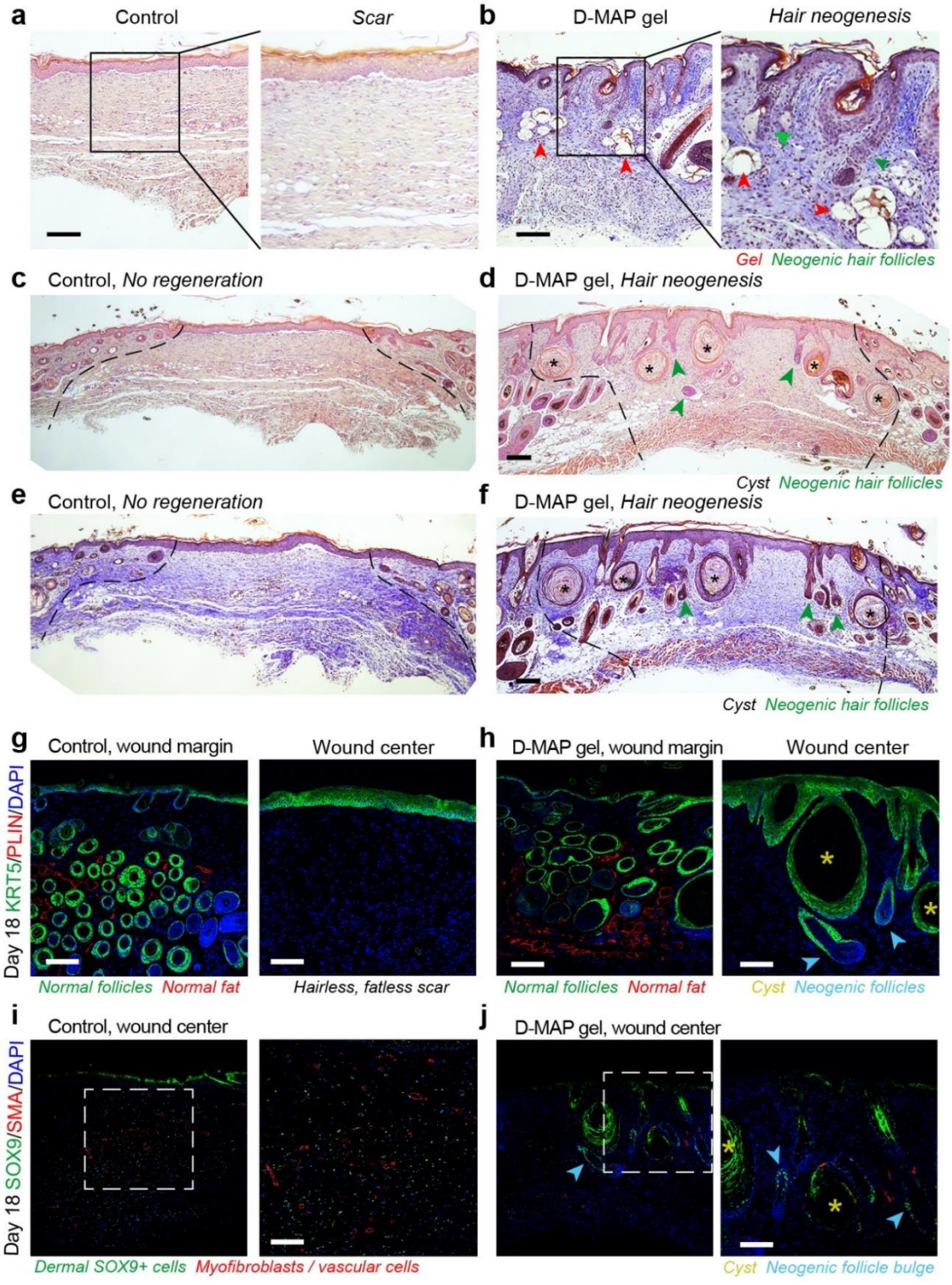

Figure 2-2 D-MAP hydrogel induces neogenesis of hair follicles in full-thickness skin wounds in B6 mice. a-f) H&E (a, c, d) and Trichrome staining (b, e, f) of healed 4-mm full-thickness splinted skin wound on day 18. Control (sham-treated) wounds heal with scarring (a, c, e), while D-MAP gel treated wounds form numerous epidermal cysts (asterisks) and, prominently, regenerate *de novo* hair follicles

(green arrowheads) (b, d, f). In some instances, neogenic hair follicles form in close association with epidermal cysts. As compared to normal, pre-existing anagen hair follicles at the wound edges, neogenic hair follicles display early anagen stage morphology (Wound edges in b-d are outlined and D-MAP hydrogel remnants in b are marked with red arrowheads). **g-h**) Immunostaining for epithelial marker KRT5 (green) and adipocyte marker PLIN (red), reveals normal $KRT5^+$ anagen hair follicles and many mature $PLIN^+$ dermal adipocytes (left panels in g and h). Regeneration of new KRT5+ hair follicles (arrowheads in h) along with KRT5+ epidermal cysts is observed only in D-MAP hydrogel-treated wounds (right panel g vs. h). No neogenic adipocytes are observed in hair-forming D-MAP-treated wounds. **i-j)** Immunostaining for SOX9 (green) and SMA (red), reveals many $SOX9^+$ epithelial cells within the bulge region of neogenic hair follicles in day 18 DMAP-treated wounds (arrowheads in j). In contrast, in control (sham-treated) wounds that undergo scarring, dermal wound portion contains many $Sox9^+$ cells, many of which also co-express contractile marker SMA (i). Expression of SMA is also seen in both control and D-MAP-treated samples in blood vessels. Scales in a-j = 100 μm. The images are representative of slides from 4 animals per group.

2.2.5. D-MAP hydrogel implants enhance myeloid cell recruitment.

To determine whether an enhanced immune response was leading to enhanced D-MAP or 1:1 L:D MAP degradation in the wound microenvironment, we utilized a subcutaneous implantation model which also allows for larger amounts of hydrogel to be implanted, and thus remain present longer, than in the small excisional wound model. To test whether the subcutaneous implants of D-MAP hydrogel resulted in enhanced immune cell recruitment, we utilized immunofluorescent microscopy with Alexa Fluor488 labeled MAP hydrogel. We found that implants containing just L-MAP display a background level of CD11b cells within the hydrogel, as previously observed[33], while D-MAP or L/D-MAP resulted in the robust accumulation of CD11b-expressing myeloid cells within and around the scaffold (**Figure 2-3a-b**). Standard histological analysis of a repeat experiment of different formulations of subcutaneously implanted MAP hydrogel confirmed the activation of type 2 immunity with an atypical, type 2 granulomatous response dominated by the accumulation of individual macrophages within and around D-MAP hydrogel implants, but not L-MAP hydrogel implants (**Figure A-3a** and Supplementary Discussion). Immunofluorescent staining for F4/80 and CD11b confirms the enhanced recruitment of macrophages, without giant cell formation, in D-MAP implants (**Figure A-3b** and **A-3c** and Supplementary Discussion). These results confirm

that D-MAP elicit a more robust immune response, and degradation by the accumulated immune cells likely contributes to the enhanced degradation of D-MAP in our previous wound experiments.

Allergic responses and parasites can elicit a type 2 immune response including atypical type 2 granulomatous responses at least partially through interleukin (IL)-33 production by epithelial cells, recruited myeloid cells and resident macrophages[51–54]. Implanted, non-degradable microparticle-based materials elicit an IL-33-dependent type 2 innate immune response by circulating $CD11b^+$ myeloid cells and macrophages[55]. It is possible that MAP particles could activate this same program, especially given the atypical type 2 foreign body responses observed in D-MAP samples. Indeed, 21 days after implantation, we found similar numbers of IL-33-expressing $F4/80^+CD11b^+$ macrophages in the center/core of both L- and D-MAP implants (**Figure 2-3c** and **2-3d**), consistent with both L- and D-MAP samples activating this type 2 pathway. However, there was a dramatic increase in IL-33 producing $IL\text{-}33^+F4/80^+$ macrophages at the edges of only D-MAP implants (**Figure 2-3c** and **2-3d**). These results confirm that the hydrogel possesses a type 2 innate "adjuvant" effect, that may activate the adaptive immune system and contribute to enhanced immune activation with D-MAP hydrogel. When L-MAP scaffolds are used, the immune response remains mild as the hydrogel degrades slowly over time[56], but the presence of D-peptide accelerates immune mediated degradation.

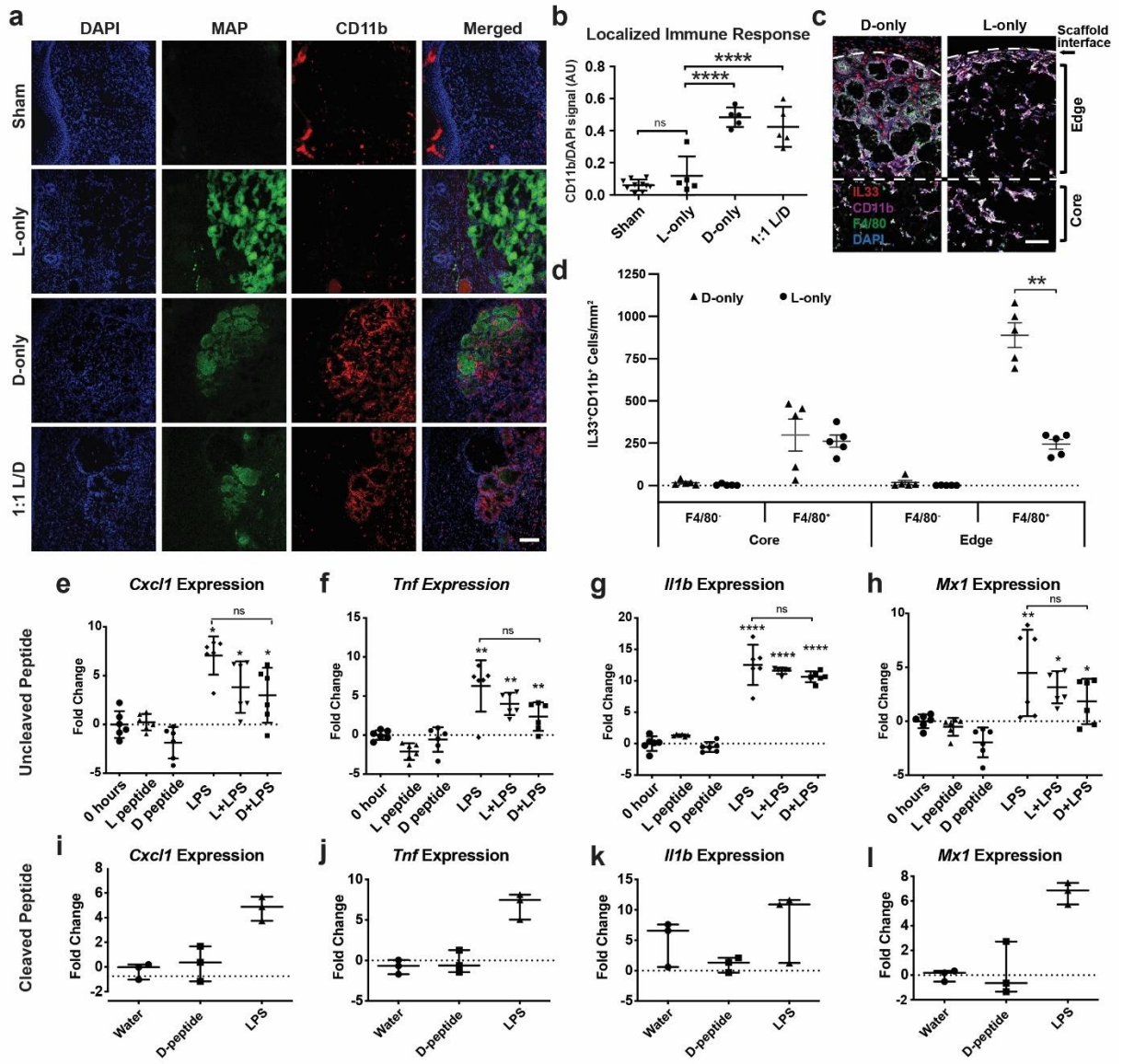

Figure 2-3 Myeloid cell activation and accumulation is associated with increased clearance of hydrogel containing D-chiral peptides, but D-chiral peptides do not directly induce transcriptional activation of myeloid cells *in vitro* through pattern recognition receptors engagement. a) Representative confocal immunofluorescent images staining myeloid cells ($CD11b^+$) within healed wounds of B6 mice in the absence or presence of the indicated hydrogel. Scale = 100μm. **b)** Quantification of $CD11b^+$ cellular infiltrate in healed tissue 21 days after wounding in the presence or absence of hydrogel. Each point represents average of 3 slides for each wound. All analysis is by one-way ANOVA (F-value (3,21): 41.10; **** denotes $p<0.0001$). **c-d)** Representative high-resolution confocal immunofluorescence imaging for CD11b, F4/80, DAPI, and IL-33 from subcutaneous implants of L- or D-MAP hydrogel implants (c) and quantification of IL-33 producing macrophages and other myeloid cells at hydrogel edge and core. n=5 B6 mice, mean +/- SEM (d), multiple t-tests adjusted for multiple comparisons using Holm-Sidak method (** denotes $p=0.00014$). Scale = 100μm. **e-h)** Murine bone marrow derived macrophages (BMDMs) from B6 mice were stimulated with 500 μg/ml of full-length L- or D- crosslinker peptide in the presence or absence of lipopolysaccharide (10ng/ml) for 6 hours. Shown are qPCR results of 4 inflammatory genes from two separate experiment performed with n = 6. All

analysis is by one-way ANOVA (Respective F-values (5, 30): 15.66, 17.62, 107.1, and 8.229). **i-l)** BMDMs were stimulated with LPS (10ng/ml) or cleaved D-crosslinker peptide (500μg/ml) that possessed an N-terminal D-amino acid. Experiment was performed in triplicate. All analysis is by one-way ANOVA (Respective F-values (2,6): 20.28, 30.86, 2.178, and 22.72). All data in Figure 3 is plotted as a scatter plot showing the mean and standard deviation. *, **, *** represent statistical significance by ANOVA using the Tukey multiple comparisons test to determine statistical significance.

2.2.6. Free D-chiral peptides avoid pathogen recognition receptors.

We next tested whether D-peptides could directly activate innate immunity through traditional PRR-induced transcriptional response. We stimulated murine bone marrow derived macrophages (BMDMs) with L-peptide or D-peptide in the presence or absence of bacterial lipopolysaccharide (LPS), the Toll-like receptor 4 agonist that results in rapid macrophage transcriptional responses. We chose to examine genes reliably and potently induced downstream of the major signaling pathways downstream of a variety of cellular insult (AP-1, MAPK, NF-kB, and type I IFN) to simultaneously interrogate multiple PRR pathways[57–59]. To our surprise, neither L- nor D-amino acid containing crosslinking peptides alone at high doses (1mg/ml) induced the expression of pro-inflammatory genes *Tnf* (NF-kB dependent), *Il1b* (NF-kB and MAPK dependent), *Cxcl2* (AP-1 dependent early response), or *Mx1* (type I IFN dependent) in murine BMDMs at 6 hours (t_{max} of gene induction; **Figure 2-3e-l**). Additionally, neither L- nor D-peptides enhanced the ability of LPS to induce the expression of these same genes (**Figure 2-3e-h**).

Previous studies have shown that peptides containing an N-terminal D-methionine can activate the innate immune receptor formyl peptide receptor 2 and formyl peptide like receptor 2[60–62]. Since cleavage of D-amino acid peptide can result in shorter peptides that contain a D-amino acid at the N-terminus, we next wished to examine whether a peptide corresponding to the cleaved D-peptide could activate inflammatory responses in BMDMs. Similar to the results with intact D-peptide, high concentrations of cleaved D-peptide (1mg/ml) did not induce the

transcription of *Tnf, Il1b, Cxcl2,* or *Mx1* at 6 hours (**Figure 2-3i-l**). Since there is a very low likelihood that cleaved D-peptide will be present at such high local concentrations within the implanted hydrogel while it is being degraded *in vivo*, these show that D-chiral peptides are poor activators of a traditional PRR-mediated inflammatory response in macrophages and suggest that D-peptides may be acting as antigens to enhance immunity, leading to enhanced degradation of D-MAP.

2.2.7. D-MAP elicits antigen-specific humoral immunity.

We next evaluated whether the D-MAP activates adaptive immunity. The adaptive immune system recognizes non-self-peptide antigens to induce cell mediated (T cell) and humoral (B cell) immunity. Peptides containing D-amino acids have been reported to activate or suppress T cell dependent and T cell independent adaptive immune responses[37,63]. In the context of the MAP, cross-linking peptides that are non-native may be presented to the immune system until fully degraded. D-peptides could be presented by antigen presenting cells directly to T cells, eliciting a T cell dependent adaptive immune response or alternatively, the presence of D-amino acid containing peptides on the surface of a large molecule of MAP hydrogel could directly crosslink the B cell receptor, leading to T cell independent antibody responses similar to T cell independent antigens. To test this hypothesis, we examined whether mice that were wounded or received subcutaneous implants of L-MAP, D-MAP, or 1:1 L/D-MAP were able to develop T-helper cell dependent (IgG1 or IgG2a) or T cell independent (IgG3) antibodies against L- or D-amino acid containing crosslinkers[64–67].

Indeed, regardless of whether D-containing MAP hydrogel was applied to wounded tissue or given via subcutaneous implants, mice developed a T cell dependent IgG1 and IgG2a response against the D-amino acid containing peptide, but not a T cell independent IgG3

response. These results are more consistent with a T cell-dependent immune response against D-peptides (**Figure 2-4a-b**). IgG1 is typically associated with a Th2 “tissue repair” type response, while IgG2a is typically associated with a Th1 “foreign body” response that typically requires strong adjuvants to develop, depending on the strain of mice[68,69]. The fact that anti-D peptide-specific IgG2a induced when the hydrogel was given to mice in a wound environment but not when the hydrogel was given in the subcutaneous implant model suggests that, by itself, the hydrogel does not possess sufficient adjuvant effects to induce robust Th1 responses. However, the inflammation present in the wound environment may result in a mixed Th2/Th1 response to the D-MAP (**Figure 2-4b** and **2-3e**). Mice that were treated with L-MAP alone did not develop antibody responses to L-peptide.

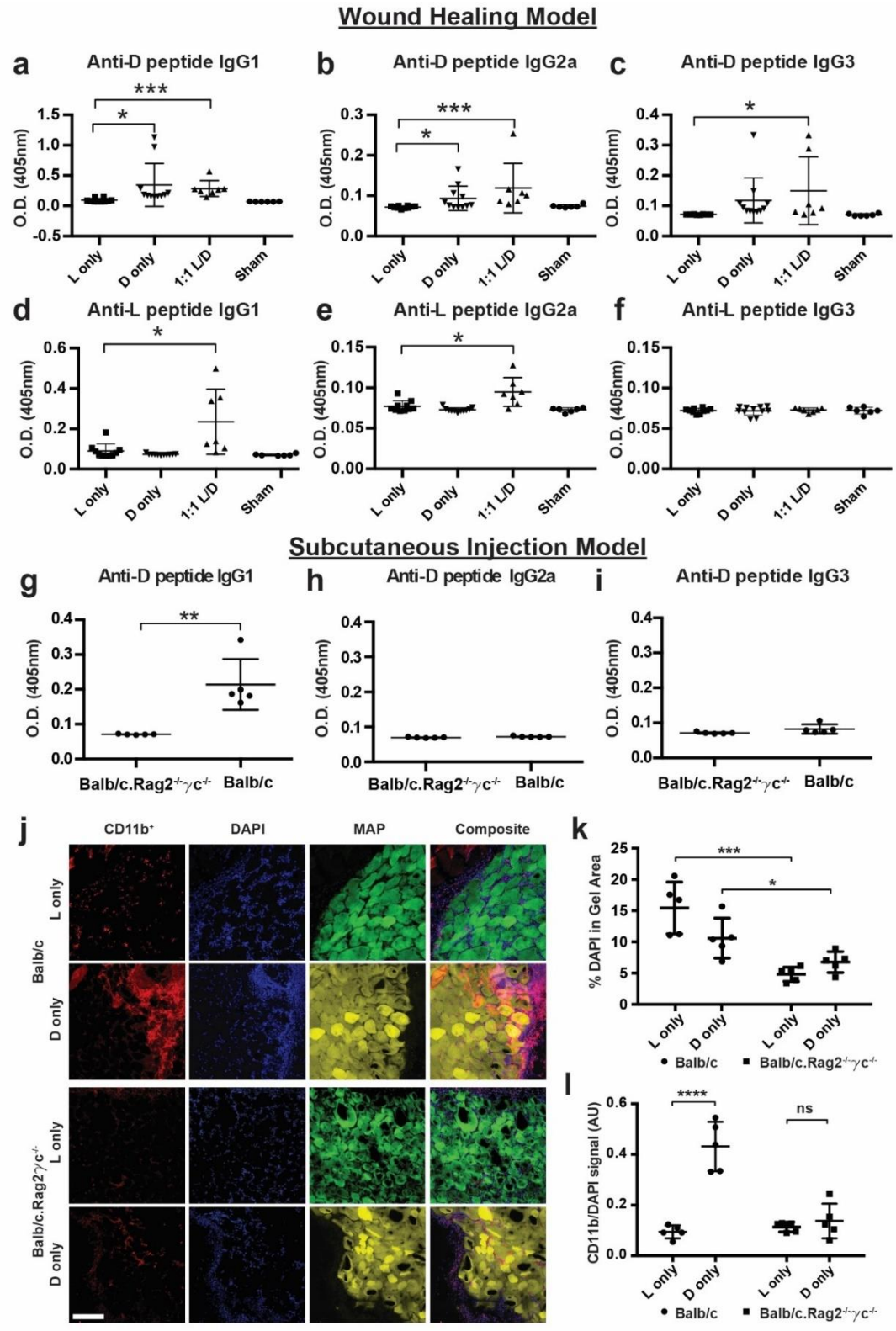

Figure 2-4 D-MAP induces antibody responses *in vivo* and requires an intact adaptive immunity for optimal myeloid cell recruitment. a-c) Measurement of anti-D specific IgG subtype antibodies by ELISA 21 days following wound healing experiments in SKH1 mice treated with indicated hydrogels. **d-**

f) Measurement of anti-L specific IgG subtype antibodies by ELISA 21 days following wound healing experiments in SKH1 mice treated with indicated hydrogels. Each data point represents one animal and all analysis in a-f is by unpaired two-tailed t-test comparing each condition to L only. **g-i)** Measurement of anti-D specific IgG subtype antibodies in Balb/c or Balb/c.Rag2$^{-/-}\gamma c^{-/-}$ mice given a subcutaneous injection of D-MAP 21 days after injection. Each data point represents one animal and all analysis in g-I is by unpaired two-tailed t-test (** denotes p=0.0022). j-l) Representative examples of confocal immunofluorescent imaging for CD11b, DAPI, and hydrogel from subcutaneous implants of L- or D-MAP hydrogel implants in Balb/c or Balb/c.Rag2$^{-/-}\gamma c^{-/-}$ mice. Scale = 200μm. (j) and quantification of total DAPI^{+} cells (k) and CD11b^{+} myeloid cells (l). Data is plotted as a scatter plot showing the mean and standard deviation. Each point represents average of 3 slides for each wound. All analysis is by unpaired two-tailed t-test (* denotes p=0.0455, *** denotes p=0.0006, **** denotes p<0.0001) represent statistical significance by student t-test for the comparison indicated.

2.2.8. D-MAP recruits myeloid cells via adaptive immune response.

Our data suggest that the activation of adaptive immune responses to D-MAP contributes to immune infiltration and degradation of D-MAP. To test this hypothesis further, we examined whether Balb/c.Rag2$^{-/-}\gamma c^{-/-}$ mice, which are devoid of an adaptive immune system, innate lymphoid cells, and IL-2/IL-15 signaling, but possess a fully functional myeloid system, will exhibit reduced immune infiltration[70]. Indeed, total cellularity and the specific recruitment of CD11b^{+} myeloid cells to D-MAP hydrogel in Balb/c.Rag2$^{-/-}\gamma c^{-/-}$ mice were decreased to comparable levels to those seen in L-MAP in WT mice (**Figure 2-4k-l**).

2.2.9. D-MAP-induced skin regeneration relies on adaptive immunity.

To determine whether the adaptive immune response was required for the development of neogenic hair follicles, we next performed excisional splinted wounds in B6 and B6.Rag1$^{-/-}$ mice, and examined them 25 days after wounding with untreated (sham) or treated wounds with 1:1 L/D-MAP gel. Of note, because in preliminary studies, scars induced by 4-mm punch wounds healed with extremely small scars in B6 mice, we used a 6-mm punch in this experiment.

Sham wounds in B6 mice demonstrated an obvious depigmented, irregularly shaped scar, while scars in B6 mice treated with 1:1 L/D-MAP gel were difficult to identify visually as they

displayed hair growth over the wounds and less atrophy/surface changes typically seen in scars (representative example **Figure 2-5a**, all wound images **Figure A-4**). Scars in sham-treated or 1:1 L/D-MAP-treated B6.Rag1$^{-/-}$ mice were smaller than those in sham-treated B6 mice, but were identifiable in B6.Rag1$^{-/-}$ mice regardless of whether wounds were sham treated or hydrogel treated (**Figure 2-5a**). All wound (including 1:1 L/D-MAP-treated B6 wound areas) injuries were confirmed by examining the defect on the fascial side of the tissue after excision of skin. Histological sections of the healed skin of mice displayed significant neogenic hairs and sebaceous glands only in wounds of wildtype mice treated with 1:1 L/D-MAP (**Figure 2-5b-d**, and **Figure A-5**). Sham wounds in B6 and Rag$^{-/-}$ mice, and in the 1:1 L/D-MAP treated B6.Rag1$^{-/-}$ mice displayed prominent scars, without hairs or sebaceous glands, confirming the requirement of adaptive immune system in skin regeneration by D-peptide containing MAP gel (**Figure 2-5b-d**). These studies highlight that hair follicle structures can be regenerated through adaptive immune activation from MAP hydrogel scaffolds.

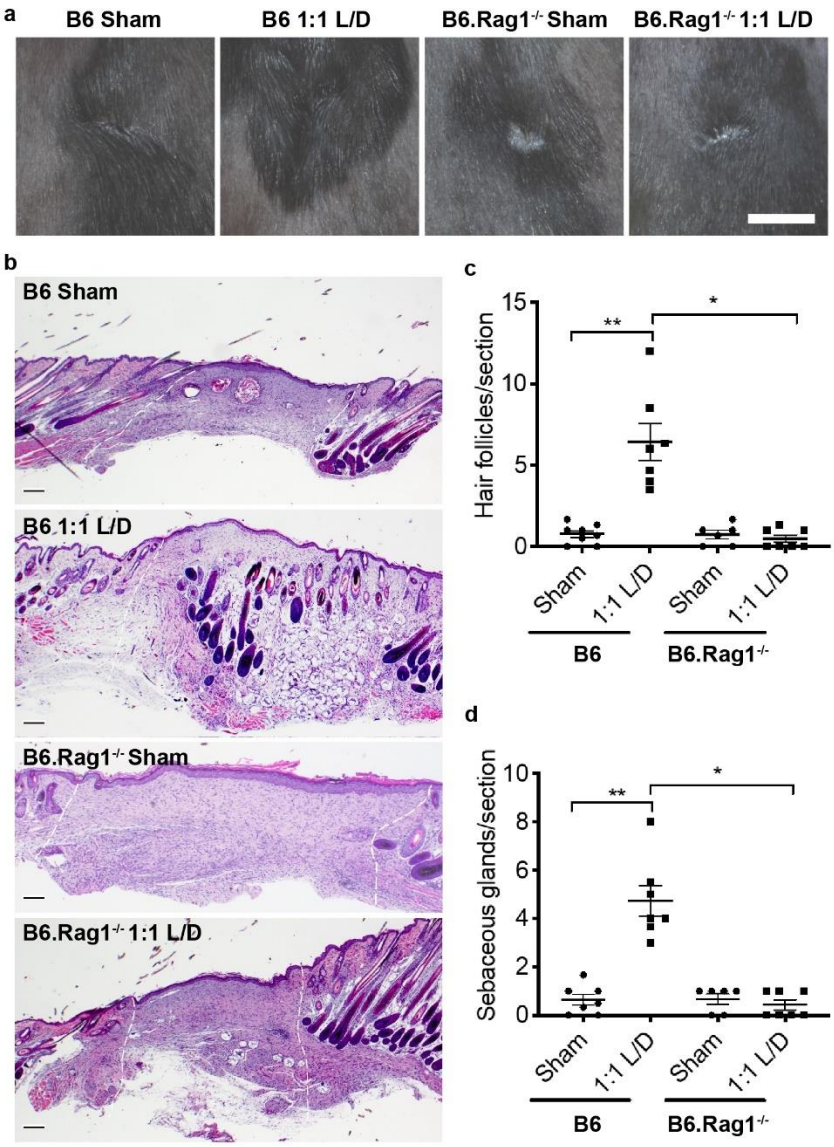

Figure 2-5 D-MAP requires an adaptive immune system to induce hair follicle neogenesis. **a**) Representative examples of gross clinical images of healed splinted excisional wounds in B6 or B6.Rag1$^{-/-}$ mice by DSLR camera 17 days later treated as sham (no hydrogel) or 1:1 L/D-MAP treatment. Scale = 5mm. **b**) Histologic sections of healed tissue from B6 or B6.Rag1$^{-/-}$ mice. Scale = 200μm. White dashed lines denotes wounded area. Quantification of the average numbers of **c**) hair follicles and **d**) sebaceous glands from 3 histological sections per sample from B6 mice and B6.Rag1$^{-/-}$ mice. Data is plotted as a scatter plot showing the mean and SEM. * denotes two-tailed p=0.002 by Mann Whitney test, for inter-strain/identical treatment comparison and ** denotes p=0.0039 by Wilcoxon test for intra-strain/different treatment comparison.

2.3. Conclusion

In most mammals, the natural process of scar formation and tissue fibrosis is highly evolved and is a tissue-scale attempt to restore critical barrier functions for survival. This

process, however, is ultimately a biological ‘triage’ that favors the rapid deposition of a fibrotic matrix to restore the barrier at the expense of a loss of function of complex tissue. In the skin, this fibrotic response results not only in a loss of functioning adnexal structures, but skin tissue that is more fragile and prone to re-injury. A major goal when engineering skin regeneration is to allow for the rapid restoration of barrier function while providing increased tissue tensile strength and higher tissue function. Many biomaterial-based approaches including addition of growth factors and decellularized extracellular matrix constructs display limited success in restoring function in wounds. We previously showed that the MAP scaffold can accelerate wound closure in murine wounds[1]. Our findings reported here further highlight that incorporation of a modest adaptation to MAP that enhanced a type 2 innate and adaptive immune response, induced skin regeneration: hair neogenesis and improved tensile strength (**Figure 2-6**). This response was dependent upon the generation of an adaptive immune response to D-enantiomeric peptides, and occurred without addition of stem cells, growth factors, or adjuvants. Importantly, this regenerative response was decoupled from wound closure that begins immediately, consistent with the time needed to generate an antigen specific immune response.

While adaptive immunity can contribute to fibrosis, foreign body formation, and rejection of biomaterial implants [38–40], adaptive immune activation from growth factor containing extracellular matrices can enhance muscle regeneration [30,40]. Further, other biomaterials were created to directly activate specific components of the immune system to treat cancer as immunotherapy platforms[71,72]. In concert, these studies suggest that the role of the adaptive immune system in tissue repair is significantly more complex than previously realized. Our findings suggest that an engineered type 2 immune response to sterile, degradable microparticle-based materials can trigger regeneration rather than fibrosis and further support a role of adaptive

immune cells to restore tissue function. Finally, we display the potential of the MAP scaffold as a potent immunomodulatory platform. Future identification of immune factors that tip the balance towards regeneration rather than eliciting scarring or a foreign body response may lead to improved biomaterials.

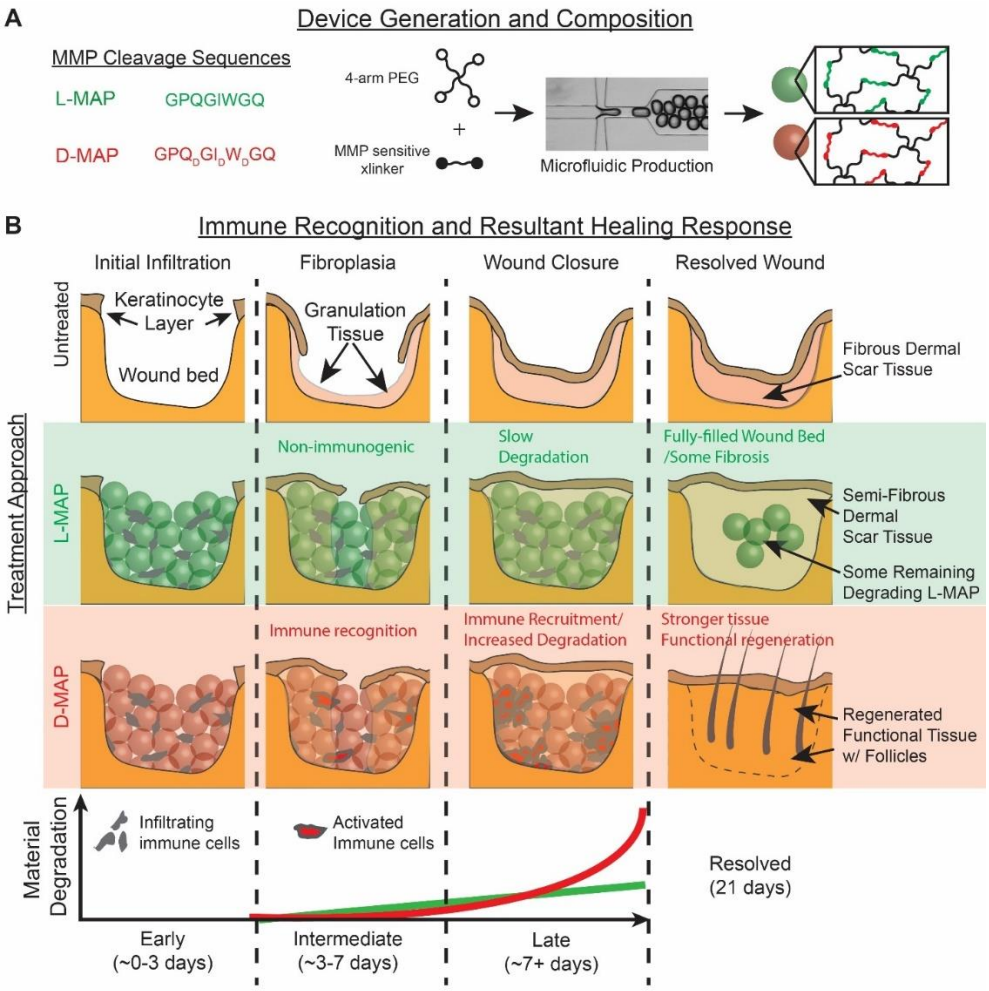

Figure 2-6 Graphical Abstract. a) Representation of amino acid chirality within the cross-linking peptides, microfluidic formation of the hydrogel microbeads incorporating L- or D- chirality peptides. **b)** The use of L- or D-MAP in a wound healing model demonstrates that both L- or D-MAP hydrogel fill the wound defect. While wounds that heal in the absence of hydrogel heal with an atrophic scar with loss of tissue, the epidermis forms over the scaffold in both cases and allows for increased dermal thickness. However, in the case of D-MAP, the hydrogel activates the adaptive immune system over time, resulting in tissue remodeling and skin regeneration as the adaptive immune system degrades the D-MAP scaffold.

2.4. Methods

2.4.1. L-MMP and D-MMP MAP Hydrogel Formation.

Microfluidic water-in-oil droplet generators were fabricated using soft lithography, as previously described[33]. To enable microgel formation, two aqueous solutions were prepared. One solution contained a 10% w/v 4-arm PEG-vinyl sulfone (20 kDa, JenKem USA) in 300 mM triethanolamine (Sigma), pH 8.25, pre-functionalized with 500μM K-peptide (Ac-FKGGERCG-NH2) (GenScript), 500μm Q-peptide (AcNQEQVSPLGGERCG-NH2), and 1 mM RGD (Ac-RGDSPGERCG-NH2) (GenScript). The other solution contained an 8mM di-cysteine modified Matrix Metalloprotease (MMP) (Ac-GCRDGPQGIWGQDRCG-NH2) (GenScript) substrate with either all L-chirality amino acid residues for L-MMP microgels or D-chirality amino acid substitution of amino acids at the site of MMP-mediated recognition and cleavage (Ac-GCRDGPQ_DG$I_D$$W_D$GQDRCG-NH2) for D-MMP microgels. We matched the stiffness of the two hydrogels which required minimal changes to peptide crosslinker solution (L-MAP – 8mM; D-MAP – 8.2mM). The oil phase was a heavy mineral oil (Fisher) containing 0.25% v/v Span-80 (Sigma). The two solutions were mixed in the droplet generator and pinched immediately into monodisperse droplets. Downstream of the pinching region, a second oil inlet with a high concentration of Span-80 (5% v/v) was mixed with the flowing droplet emulsion. Both aqueous solution flow rates used were 0.75μL/min, while both oil solutions were flowed at 4μL/min. The mixture was allowed to react overnight at room temperature and purified by repeated washes with an aqueous buffer of HEPES buffered saline pH 7.4 and pelleting in a tabletop centrifuge at 18000 rcf for 5 mins. Raw materials are purchased endotoxin free and the final hydrogels are tested for endotoxin levels prior to implantation.

2.4.2. Generation of MAP scaffolds from building block microgels

Fully swollen and equilibrated building block microgels were pelleted at 18000 rcf for five minutes, and the excess buffer (HEPES pH 7.4 + 10 mM CaCl2) was removed by aspiration. Subsequently, building blocks were split into aliquots, each containing 50 µl of concentrated building blocks. An equal volume of HEPES pH 7.4 + 10 mM CaCl2 was added to the concentrated building block solutions. Half of these are spiked with Thrombin (Sigma) to a final concentration of 2 U/ml and the other half spiked with FXIII (CSL Behring) to a final concentration of 10 U/ml. These solutions were then well mixed and spun down at 18000 rcf, followed by removal of excess liquid with a cleanroom wipe (American Cleanstat).

Annealing was initiated by mixing equal volumes of the building block solutions containing Thrombin and FXIII using a positive displacement pipet (Gilson). These solutions were well mixed by pipetting up and down, repeatedly, in conjunction with stirring using the pipet tip. The mixed solution was then pipetted into the desired location (mold, well plate, mouse wound, etc.) or loaded into a syringe for subcutaneous injection. The microgel fabrication was performed under sterile conditions. Following particle fabrication, 20µLof dry particles were digested in 200µLdigestion solution (collagenase IV 200 U/ml+ DNase I 125U/ml) and incubated in 37 C for 30 min before testing. Endotoxin concentrations were determined with Pierce LAL Chromogenic Endotoxin Quantitation Kit (Thermo Fisher Scientific) following manufacturer's instructions. Particle Endotoxin levels were consistently below 0.2 Endotoxin U/mL.

2.4.3. Degradation with collagenase

Microgel degradability was confirmed with collagenase I. A 1:1 v/v mixture of microgels formed with MMP-D- or MMP-L-sensitive cross-linker was diluted in collagenase I to a final

concentration of 5 units collagenase/mL. This mixture was added to a 1 mm PDMS well and briefly allowed to settle. Images of the microgels were taken near the bottom of the well every 30 seconds for 2 hours with a confocal microscope. Image analysis was carried out through a custom MATLAB script (script provided by Dr. Sasha Cai Lesher-Perez) and ImageJ. MATLAB was used to determine the number of intact microgel spheres in each image. The previously mentioned script was applied with a minimum droplet radius of 30 pixels, a maximum droplet radius of 50 pixels, and a sensitivity factor of 0.98 for channel-separated images. Then, ImageJ was used to determine the area fraction fluorescing for each channel and each image. The thresholding for each image was set to a minimum of 50 and a maximum of 255 and the fluorescing area fraction was recorded.

2.4.4. Mouse excisional wound healing model (Protocol# 10-011, UCLA IUCAC)

Mouse excisional wound healing experiments were performed as previously described[33,41]. Briefly 10-week old female SKH1 mice (Charles River Laboratories; n=6), or 10-week old female C57Bl/6 (B6) or B6.Rag1$^{-/-}$ mice (Jackson Laboratories; n=4 twice) were anesthetized using continuous application of aerosolized isoflurane (1.5 vol%) throughout the duration of the procedure and disinfected with serial washes of povidone-iodine and 70% ethanol. The nails were trimmed and buprenorphine 0.05mg/ml) was injected intramuscularly. The mice were placed on their side and dorsal skin was pinched along the midline. A sterile 4 mm biopsy punch was then used to create 2 through-and-through wounds, resulting in four clean-cut, symmetrical, full-thickness excisional wounds on either side of the dorsal midline. A small amount of adhesive (VetBond, 3M, Inc.) was then applied to one side of a rubber splint (O.D. ~12mm; I.D. ~8mm) and the splint was placed centered around the wound (adhesive side down). The splint was secured with eight interrupted sutures of 5-0 non-absorbable Prolene. A

second splint wrapped in Tegaderm (3M, Inc.) was attached to the initial splint via a single suture to act as a hinged cover to allow wound imaging while acting as a physical barrier above the wound bed. After addition of thrombin (2 U/ml) and 10mM $CaCl_2$, the experimental material (20 μL of L-only MAP, D-only MAP, 1:1 v/v mixture of L-MAP and D-MAP in HEPES-buffered saline containing Factor XIII (10U/ml) and 10mM CaCl2, or no hydrogel) was then added to one of the wound beds randomly to ensure each hydrogel treatment was applied to the different regions of wounded back skin to limit potential for site-specific effects. Following treatment, a Tegaderm-coated splint was applied, and wound sites were covered using a self-adhering elastic bandage (VetWrap, 3M, Inc.). Animals were housed individually to prevent wound manipulation. At the culmination of the wound healing experiment (Day 21 or Day 25) the mice were sacrificed by isoflurane overdose and cervical dislocation and imaged with a digital camera. The skin was excised and processed via either paraffin embedding for H&E or OCT blocks for immunofluorescence.

2.4.5. Evaluation of wound closure

Wounds were imaged daily to follow closure of the wounds. Each wound site was imaged using high-resolution camera (Nikon Coolpix). Closure fraction was determined as described previously[33]. Briefly, closure was determined by comparing the pixel area of the wound to the pixel area within the 10 mm center hole of the red rubber splint. Closure fractions were normalized to Day 0 for each mouse/scaffold sample. Investigators were blinded to treatment group identity during analysis.

2.4.6. Wound Imaging

On the specified day after wounds were created, close up images of wounds were taken using a Canon Powershot A2600 or a Nikon D3400 DSLR Camera with an 18-55mm Lens, and

were cropped to the wound area but not manipulated further. For wound closure, area was obtained using ImageJ by a subject blinded to the treatment.

2.4.7. Tissue collection

After wounds healed, mice were sacrificed on the indicated day after wounding, and tissue collected with a ~5mm margin around healed wound. The samples were immediately submerged in Tissue-Tek Optimal Cutting Temperature (OCT) fluid and frozen into a solid block with liquid nitrogen. The blocks were then cryo-sectioned by cryostat microtome (Leica) and kept frozen until use. The sections were then fixed with 4% paraformaldehyde in 1X PBS for 30 minutes at room temperature, washed with 1X PBS, and kept at 4°C until stained. For antibody production analysis, blood harvested via cardiac puncture to obtain serum for ELISA.

2.4.8. Macrophage cell culture

Mouse bone marrow derived macrophages were generated as previously described previously[58]. Briefly, following euthanasia, hindlimbs were removed aseptically and bone marrow was flushed. Bone marrow cells were cultured in CMG-conditioned complete DMEM media for 6 days. Cells were then treated with intact L-or D- peptide in ultra-pure H_20 at the indicated concentration in the presence or absence of LPS (10ng/ml). Cleaved D-peptide (with an N-terminal D-amino acid) (W_DGQDRCG-NH2) was also used when indicated. Cells were harvested at 6 hours following treatment and expression of cytokines and chemokines was examined by qPCR using specific primers as described previously[73].

2.4.9. Incisional wound model

10-week old female C57Bl/6 mice (Jackson Laboratories) were anesthetized with isoflurane as above. The dorsal and side skin was dehaired using electric clippers followed by Nair (Church and Dwight, Inc.), then disinfected with serial washes of povidone-iodine and 70%

ethanol. The nails were trimmed to lower the incidence of splint removal, and buprenorphine was injected IM as above. An incisional 2cm x 1cm wound was made with a scalpel. Mice (5 per group) were randomly assigned to receive 50μL of L-MAP, D-MAP, 1:1 v/v mixture of L-MAP and D-MAP or no hydrogel (Aquaphor). The mice were wrapped with Tegaderm followed by VetWrap as above.

2.4.10. Histology and analysis.

Samples were sectioned (6-10μm thick), then stained with hematoxylin and eosin or Masson trichrome by the UCLA Tissue Procurement Core Laboratory using standard procedures. Sections were examined by a board certified dermatopathologist (P.O.S.) and/or an expert in hair follicle neogenesis/regeneration (M.V.P.) who were blinded to the identity of the samples, for the presence of adnexal structures in tissue sections and dermal thickness. For enumeration, two to three tissue sections from the tissue block of each wound were examined and averaged per wound to obtain the count per unit area for each sample. Wounds were splinted to prevent contraction and any sample with more than 50% wound closure by contraction were not included.

2.4.11. Tensiometry.

To evaluate the tensile properties of the healed incisional wounds, tensile testing was performed on an Instron model 3342 fitted with a 50N load cell and data recorded using the Instron Bluehill 3 software package. Tissue was collected from the wound site 28 days following wounding/treatment as a 2 cm x 4 cm “dumbbell” shape (with 1 cm center width in the handle portion). The sample was oriented such that the healed wound spanned the entire middle section of the dog bone (the thinner 1cm region) and the healed wound long axis was orthogonal to the direction of tension applied. The tissue sample was loaded into the Instron and secured with

pneumatic gripers, pressurized to 40 PSI. The tissue was subjected to tensile testing at an elongation rate of 5 mm/min and ran through material failure.

For each tissue sample, stress/strain curves were calculated from force/elongation curves (provided from the Instron Bluehill software) using the known cross-sectional dimensions of the "dog bone" samples (each measured with calipers prior to placement on the Instron), and by measuring the starting distance between pneumatic grips with a caliper. The starting distance was standardized by preloading the sample to 0.5N, followed by measurement and then running of the tensile test to failure. This analysis enabled calculation of Yield Stress, which are reported in **Figure 2-1j**.

2.4.12. Subcutaneous implants of hydrogel

For subcutaneous implants, after anesthesia, 10-week-old female Balb/c and Balb/c.Rag2$^{-/-}\gamma c^{-/-}$ mice were injected with 50µL of L-MAP, D-MAP, or 1:1 v/v mixture of L-MAP and D-MAP (n = 5). 21 days later the skin and subcutaneous tissue containing the hydrogels were removed and processed for histology and immunofluorescence, and blood was collected by cardiac puncture to obtain serum for ELISA. B6 mice were used in another batch of experiments for immunofluorescence analysis and histology of subcutaneous implants.

2.4.13. Tissue section Immunofluorescence, quantification of hydrogel degradation, and immune infiltration.

Slides containing tissue sections (10-25µm thickness) were blocked with 3% normal goat serum (NGS) in 1X PBS + 0.05% Tween-20 (PBS-T). For intracellular antigens 0.2% triton was added to the blocking buffer. Primary antibody dilutions were prepared as follows in 5% NGS in 1X PBS-T: rat anti mouse CD11b clone M1-70 (BD Pharmingen; #553308) – 1:100, F4/80 clone A3-1 (BioRAD; MCA497G) – 1:400, and IL-33 (abcam; ab187060) – 1:200. Sections were

stained with primary antibodies overnight at 4°C, and subsequently washed with 3% NGS in 1X PBS-T. Secondary antibodies (Goat anti-rat Alexa-647, Invitrogen) were all prepared in 5% Normal Goat Serum (NGS) in 1X PBS-T at a dilution of 1:500. Three 5-minute washes with PBST were performed after each antibody incubation. Sections were incubated in secondary antibodies for 1 hour at room temperature, and subsequently washed with 1X PBS-T. For multicolor immunofluorescence staining for primary and secondary of each antigen were performed in sequence. Sections were either mounted with antifade mounting medium with DAPI (Fisher Scientific; H1200) or counterstained with 2 μg/ml DAPI in 1X PBS-T for 30 mins at room temperature and then mounted in Antifade Gold mounting medium.

2.4.14. Computational analysis of multi-color immunofluorescence images

A MATLAB code was used for analysis of the multicolor immunofluorescence images. The code divides the hydrogel into an Edge region (300um from hydrogel-tissue interface) and a Core region (the center of hydrogel to 200um from the inner boundary of the Edge region). For each hydrogel subregion the code reads CD11b and F4/80 signal, binarizes each to form a mask using a similar threshold for all samples. The code then uses the nuclear stain and IL-33^+ stains to identify all nuclei and IL-33^+ cells. The density of each cell type is then quantified by counting the number of nuclei and IL-33^+ cells overlapping or evading the masks divided by the area of the region of interest. Areas with defects caused by tissue sectioning were excluded from analysis. Although not affecting the code performance, the image condition was kept the same across all samples.

2.4.15. ELISA

For assessment of anti-L or anti-D antibodies, sera were collected by cardiac puncture 21 days following hydrogel application of mice (subcutaneous implant or application to wound). for

detection of anti-L and anti-D antibodies plates were coated with either L-MMP peptide or D-MMP peptide respectively (GenScript; sequence above). Serum samples were tested at a 1:500 dilution followed by incubation with alkaline phosphatase-labeled goat anti-mouse IgG1 or IgG2a, or IgG3 antibodies (Southern Biotechnology Associates or BD Pharmingen), and development with p-nitrophenylphosphate substrate (Sigma-Aldrich). Optical density at 405 nm (OD405) was read using a spectramax i3X microplate reader (Softmax Pro 3.1 software; Molecular Devices).

2.4.16. Statistics and Reproducibility

All statistical analysis was performed using Prism 6 (GraphPad, Inc.) software. Specifically, two-tailed t-test or one-way ANOVA were used to determine statistical significance, assuming equal sample variance for each experimental group when comparing individual groups. For ANOVA, post hoc analysis with Tukey multiple comparison. For histological counting, B6 and B6.Rag1$^{-/-}$ sham vs 1:1 L/D-MAP analysis, Wilcoxon signed rank analysis was performed, and B6 vs B6.Rag1$^{-/-}$ and subcutaneous immunofluorescence analysis was performed with t test with Mann-Whitney U test.

The hydrogel degradation test was performed on three separate occasions for each batch of L-MAP, D-MAP, and a 50:50 mixture of L-MAP and D-MAP for a total of nine degradation tests. In each technical replicate at least 10 microgels were imaged and analyzed for fluorescence intensity.

The evaluation of hair neogenesis in B6 mice Control vs D-MAP for **Figure 2-2** was performed on samples from n= 4 for each group. The wound healing studies comparing WT to Rag1-/- mice were repeated three times (n=4 each group). In the first experiment, all Rag1-/- mice were euthanized due to the development of severe and worsening wound infections, and

thus were not included in the final analysis. In addition, wounds/scars that showed more than 50% contraction of the wound area from the underlying fascia from any group were removed from the final data set or if the histological processing failed to identify the wound/scar bed (i.e. sample was cut through). For the histological analysis, Sham vs 1:1 L/D in B6 mice from 3 separate experiments was used (n=9 histological samples available out of an available n=12 wounds performed), while samples in the B6.Rag1-/- mice were obtained from the latter two experiments performed in B6 vs B6.Rag1-/- mice performed at the same time (n=6 histological samples available out of an n=8 wounds. The findings within this manuscript were observed in two different mouse strains (CRL-SKH and C57Bl/6) that have different adnexal structures (vellus hair only and mature/terminal follicles, respectively).

Chapter 3. MAP gels as a sustained delivery depot

3.1. Introduction

An ideal biomaterial for creating tunable immunomodulatory platform will (i) evade the foreign body response, which would otherwise wall off the material and prevent prolonged signaling to the immune system, (ii) encourage rapid immune cell invasion by providing immediate macroporosity and mechanical stability, (iii) be applied in a minimally invasive injection for ease of clinical use, (iv) deliver, in a sustained manner, the immunomodulatory molecules over an immense surface area. While in the previous chapter we showed the utility of MAP as an immunomodulatory scaffold for tissue regeneration, the response shown was mostly a type 2 response, without incorporation of any cytokine or other immunomodulatory agents. To test the potential of MAP as an immunomodulatory scaffold, especially for applications in vaccination, I first needed to characterize its cargo capacity and ability to provide prolonged release for molecules with various molecular weights and characteristics.

The MAP gel is made of stoichiometric conjugation of 4-arm PEG functionalized with vinyl sulfone, with a crosslinker peptide as well as K, Q, and RGD peptides containing thiol groups. Unlike some other platforms like MSRs or PLGA scaffolds, PEG is a very neutral molecule and cannot hold on to cargo well via affinity binding. However, the gels are made of almost 98% water, so methods for trapping cargo inside the hydrogel mesh, in place of the water, can provide an extremely high cargo capacity. The polymer mesh is made up of PEG molecules containing four 4kDa arms joined at a node which crosslink with other PEGs to form a mesh with nanopores roughly 10nm in size. Large molecules close to this size can be physically entrapped in hydrogel mesh if the nanopores are smaller than the size of the molecule (**Figure 3-1**, top). Molecules small enough to freely diffuse through the hydrogel nanopores, can be either

chemically conjugated to the hydrogel mesh, or encapsulated inside denser nanoparticles which will prevent their release before particle degradation (**Figure 3-1**, bottom). Using chemical conjugation can interfere with this stoichiometric balance of vinyl-sulfones and thiols chemistry and necessitate troubleshooting the fabrication process and assessment of gels for every new cargo and dosage.

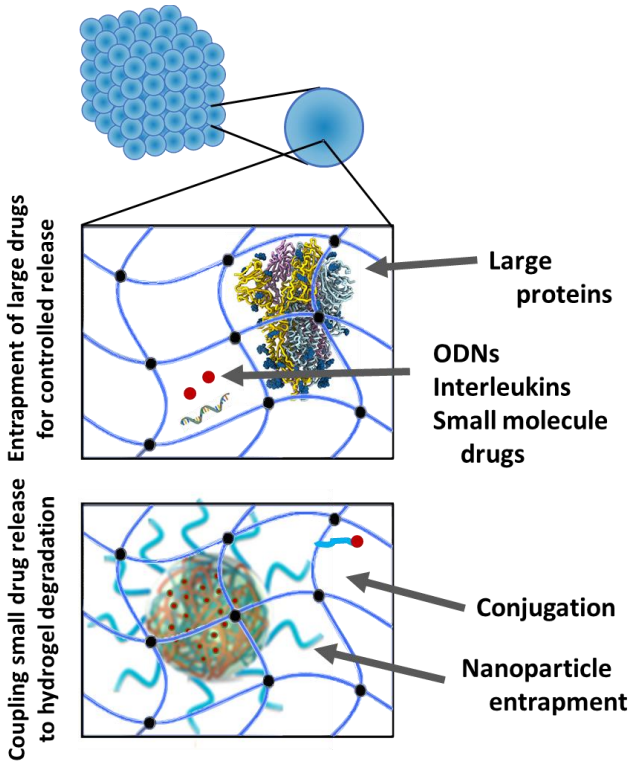

Figure 3-1 Methods for entrapment of cargo inside degradable MAP scaffold for controlled release. Large molecules can be entrapped within the dense hydrogel mesh to couple their release to hydrogel degradation (top). Small molecules can be either chemically conjugated to hydrogel mesh or encapsulated inside denser nanoparticles to prevent their burst release (bottom).

Microfluidic fabrication adds another level of complexity. As opposed to bulk gel fabrication, the pre-gel solutions for microfluidic fabrication have to remain stable for a long period before they are injected into the microfluidic droplet generator device. Reactive groups, such as amines, can compete with thiols in reacting with vinyl sulfone. When making bulk gels this is not a major issue as the thiols react much faster. However, the time it takes for

microfluidic fabrication can allow for slower reactions to happen, making the gels different at the start vs. toward the end of production. Same issue can apply to suspensions of material that are not soluble in the gel precursor solutions at desired concentrations. So, for microfluidic fabrication it is important to ensure molecules that can participate in unwanted reactions are separated and suspensions are kept from precipitation before precursor solutions are injected into the droplet generator device to forming droplets.

In this chapter, I discuss the incorporation of proteins and small molecules, either as free-standing molecules or encapsulated inside other nanoparticle platforms, inside MAP gels for controlled release.

3.2. Results and discussion

3.2.1. The polymeric mesh of MAP scaffold precursor microparticles can entrap medium to large proteins for sustained delivery.

To test the capability of MAP to be used as a sustained delivery platform we first chose to incorporate ovalbumin (OVA) and DADLE as model proteins and peptides into the microgels. OVA is a 43 kDa protein from chicken egg, which is commonly used as an antigen in immunologic studies in mice. This protein has an estimated size of 5nm. We found that using a 5% w/v 4 arm PEG-vinyl sulfone backbone we could trap OVA in the microgel mesh and with minimal initial burst release, prevent its release from hydrogel without degradation (**Figure 3-1a**, dashed line). This would allow for sustained delivery of antigen over weeks coupled to its degradation, which was confirmed by addition of 10% TrypLE to hydrogels, resulting in rapid degradation of MMP peptides and release of OVA from hydrogels (**Figure 3-1a**, solid line**)**. It is noteworthy that I could incorporate OVA in the microfluidic fabrication of MAP at high enough

concentration to reach a final dose of 2µg/µL of MAP slurry, which provides more than enough protein for vaccination in human. Reducing the molecular weight of functionalized PEG precursor in microgel or using polymer with higher number of arms, or increasing the polymer concentration, can reduce the size of the nano-scale pores and increase the density of the hydrogel mesh. This will enable entrapment of slightly smaller proteins and prolonging the diffusion time of smaller molecules out of the hydrogel mesh.

3.2.2. Secondary methods are needed for entrapment and sustained delivery of peptides and small molecule drugs with MAP

We did not anticipate the microgel mesh to be able to trap small molecules inside, however, to test whether van der Waals interactions between small molecules and hydrogel mesh are enough to provide sustained delivery we tested the release of DADLE, a 5-amino acid peptide agonist of the opioid delta receptor molecular weight of 570 Da. We chose to assess the release profile of DADLE with mass spectroscopy, instead of using a fluorescent tagged DADLE, as the small size of DADLE could allow its physical interactions to be significantly altered by the conjugation of a fluorophore. We observed that almost all DADLE was released from the hydrogel mesh within minutes (**Figure 3-1b**). Increasing the polymer mass density from 5 to 10% could only delay the release of DADLE slightly, with all the cargo still released within 12 hours. This shows that MAP gel mesh in itself is not able to provide sustained release for small molecules.

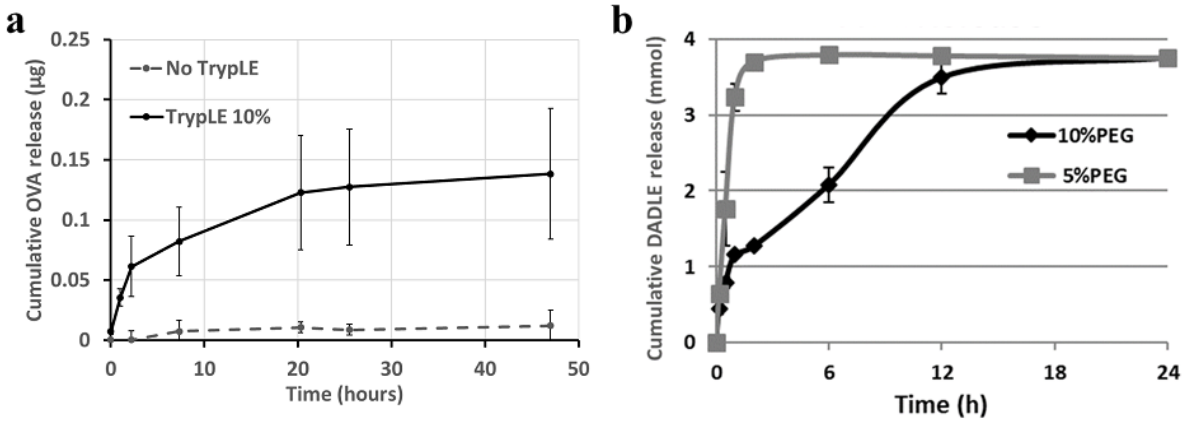

Figure 3-2 Release kinetic of small and large proteins from MAP building blocks. a) release kinetics of ovalbumin from 5% PEG microgels with (solid line) and without (dashed line) degradation by TrypLE. **b)** release kinetics of DADLE from 5% (gray) and 10% (black) PEG microgels without degradation.

3.2.3. PLGA nanoparticles can be incorporated into MAP gel precursor microparticles for long term delivery of small molecules and peptides.

To couple the release of small molecule drugs and peptides to MAP we used the well characterized Poly-lactic-co-glycolic acid (PLGA) nanoparticle delivery platform. We fabricated PLGA nanoparticles with emulsification-solvent evaporation technique, entrapping cargo in the core of nanoparticles, separated from the outside by the hydrophilic PLA layer which remains water impermeable, trapping the cargo inside, until degradation of the polymer. We hypothesized that the large size of the nanoparticles, allows them to entrap the cargo inside the microgel, providing a release profile equivalent to that of established PLGA nanoparticle platform, independent of the extent of microgel degradation.

The degradation profile of the PLGA laden MAP gels was studied in various collagenase concentrations as a surrogate for the combination of degrading power of the microenvironment and time of exposure. Release of Coumarin-6 (green fluorescent) and Alexa Fluor 568 conjugated to hydrogels with MMP sensitive crosslinker were used as a measure of drug release

and hydrogel degradation, respectively. As expected, hydrogel degradation, which is a result of enzymatic cleavage of MMP sensitive peptides, correlated linearly with collagenase concentration, while the coumarin-6 release from PLGA nanoparticles into the incubation medium, which is known to be a hydrolysis dependent process, was independent of the collagenase concentration (**Figure 3-2a**). Furthermore, fluorescent microscopy of the microgels pushed through a narrow channel after degradation showed a direct correlation between the increasing collagenase concentration and the extent of degradation, represented by diminishing Alexa Fluor 568 signal intensity, as well as particle deformability (evidenced by elongation and swelling of the particles) (**Figure 3-2b**). Furthermore, in accordance with our hypothesis, PLGA nanoparticles remained trapped inside microgels despite extensive degradation after exposure to higher collagenase concentrations.

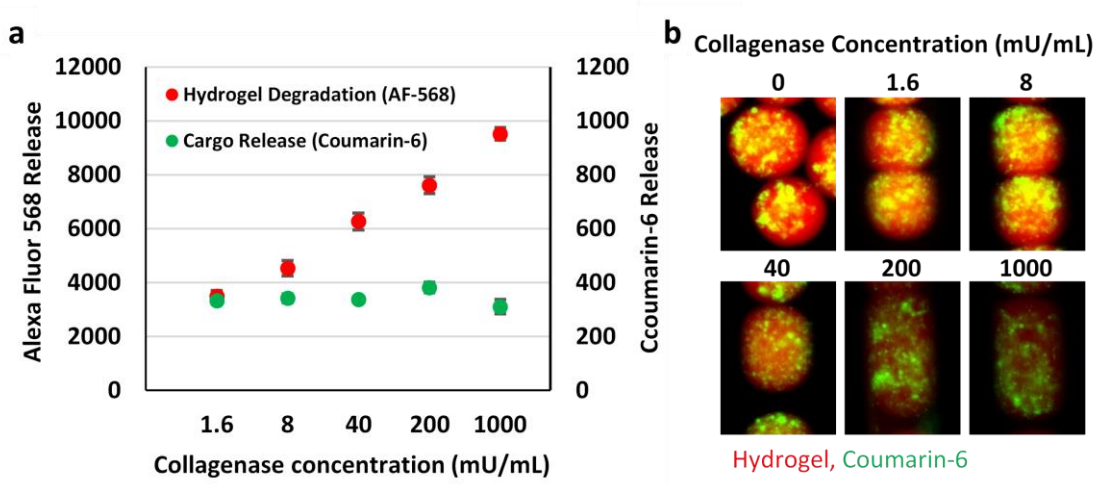

Figure 3-3 Hydrogel degradation and drug release profile of drug-PLGA NP laden MAP gels. a) Alexa Fluor 568 and Coumarin release as surrogates for hydrogel degradation and drug release from hydrogels after a 3-day incubation in collagenase solution at a range of concentrations. Mean ±SD, 3 technical replicates. **b)** representative fluorescent images of particles pushed through a 110*110µm microfluidic channel following a 3-day degradation in a range of collagenase concentrations showing the hydrogel and drug remnant as well as the hydrogel deformability.

3.2.4. LPEI nanoparticles can entrap nucleic acid adjuvants for sustained delivery with MAP gels.

We found that CpG directly mixed in the MAP gel matrix was not trapped and was completely released from hydrogels within a couple of hours because of its smaller molecular weight (20 mer, ~6kDa) (**Figure 3-3d** dashed line). To address this issue, we loaded CpG within polyethylene imine (PEI)-grafted-polyethylene glycol (PEG) nanoparticles with NP ratios (amine in LPEI to phosphate in DNA) of 5 through 30. The CpG and LPEI formed micelles in the range of 100nm. Since the LPEI-CpG interaction is electrostatic in nature, presence of physiologic levels of salt can impact the nanoparticle stability. To enhance the stability, we also tested crosslinking the nanoparticles with DTSSP, which can bind two amines on adjacent LPEI chains. The crosslinker has a dithiol group in the middle which can be reduced after being taken up by cells releasing the cargo. Crosslinking the LPEI mesh with DTSSP did not affect the size at lower NP ratios (80-100nm) but resulted in larger nanoparticles at higher NP ratios increasing the size from 60-80nm to 120nm (**Figure 3-3a**). Except for low NP ratio of 5, the nanoparticles were stable in salt, showing no aggregation at NP ratios of 10 through 30 (**Figure 3-3b**). The nanoparticles, with and without crosslinking, were able to hold onto CpG ODN and prevent CpG from moving through the gel during electrophoresis (**Figure 3-3c**). Finally, release kinetics study of CpG from nanoparticles with NP ratio of 10 incorporated into MAP building blocks during manufacturing showed a small burst release in the first few hours compared to naked CpG incorporated into MAP (**Figure 3-3d**). Degrading hydrogels with TrypLE, however, resulted in a second burst of CpG release from hydrogels, confirming the use of LPEI nanoparticles was effective in coupling CpG release to hydrogel degradation, enabling sustained release needed for immunomodulatory applications.

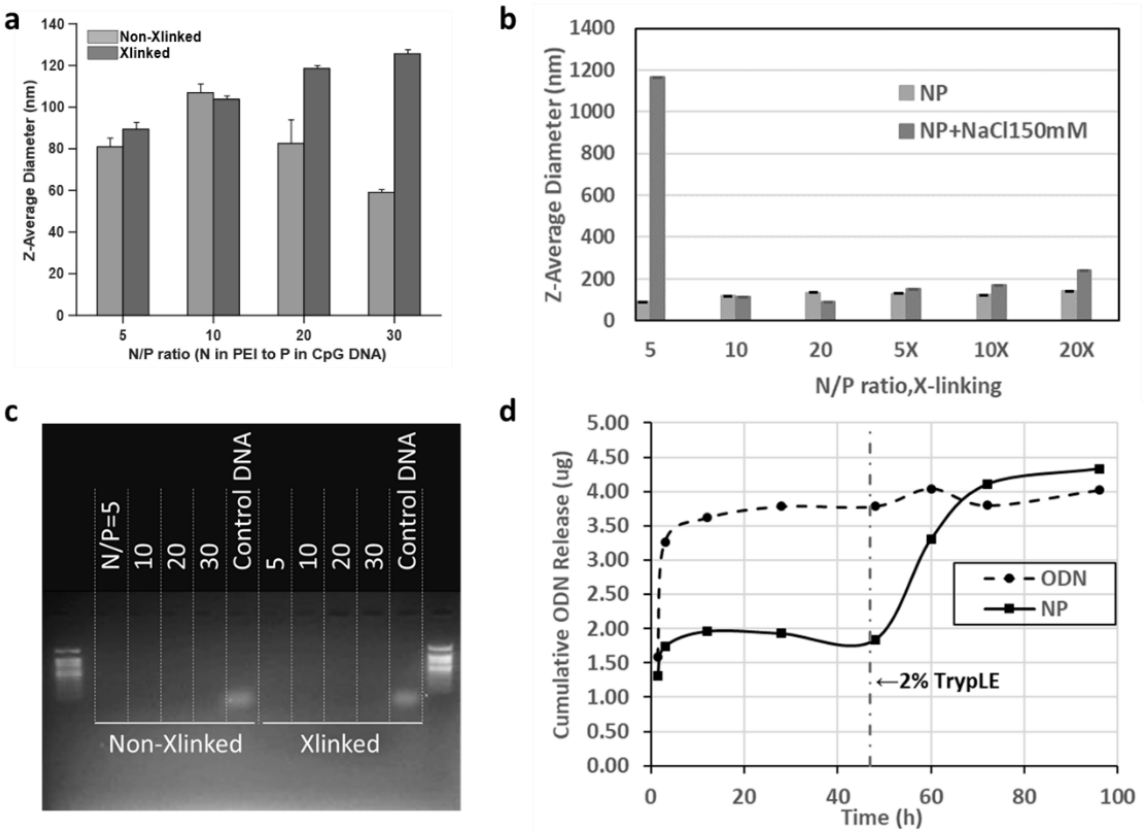

Figure 3-4 LPEI-CpG nanoparticle characterization. a) average diameter of nanoparticles measured with dynamic light scattering at different N/P ratios with and without crosslinking. **b)** Salt stability of nanoparticles with and without crosslinking with different N/P ratios. **c)** Image of gel electrophoresis showing the entrapment efficacy CpG in nanoparticles. **d)** Release kinetics characterization of microgels loaded with CpG (dashed line) and CpG encapsulated in LPEI nanoparticles at N/P=10 (solid line) before and after degradation by TrypLE.

3.3. Conclusion

In this chapter I presented three methods for sustained release of immunotherapeutic cargo using MAP gels: i) direct entrapment in hydrogel mesh for large molecules, ii) incorporation of with PLGA delivery platform for delivery of hydrophilic and hydrophobic small molecules drugs and proteins, and iii) incorporation of LPEI nanoparticles for delivery of nucleic acids. The PEG polymer platform used in MAP is highly versatile. The large water content of the PEG hydrogels provides a lot of room for incorporation of immunotherapeutic cargo.

The degradability of MAP can also be adjusted by replacing variable fractions of MMP crosslinker with non-degradable crosslinkers providing an additional mechanism for prolonging the delivery of cargo. Importantly, this tunability of the degradation rate does not impact the nanopore size, chemical composition of the hydrogel, or its mechanical properties, maintaining the high cargo capacity and porosity. In combination with PLGA nanoparticles, this will also allow MAP to provide cargo specific rerelease kinetics for multiple immunomodulatory agents from the same scaffold.

Taken together, these make MAP a highly versatile and clinically translatable platform for local drug delivery and immune modulation for a variety of applications.

3.4. Methods

3.4.1. PLGA nanoparticle fabrication

An emulsification solvent evaporation technique was applied to prepare NPs.[46] Briefly, a 50/50 wt/wt mix of PLGA (MW=35k, acid-terminated, cat# 26270, Polysciences) and PLGA-b-PEG (PLGA average Mn = 55 kDa, PEG average Mn = 5 kDa, cat# 764752, Sigma) were dissolved in dichloromethane to make 10% w/v solutions. 0.02% (w/v) coumarin-6 (green fluorescence, Sigma) was added and dissolved in the polymer solution. The resulting solution (1 mL) was added to stirred 3 mL 1% (w/v) poly(vinyl alcohol) (PVA, Mw = 25 kDa, 88% hydrolyzed, cat# 15132, Polysciences) solution using a vortex mixer at 2000 rpm for 2 min, and the emulsified polymer solution was immediately sonicated with a 20% amplitude (Sonic Dismembrator 500, Thermo Fisher Scientific) in six 10 s bursts. The test tube was immersed in ice water during sonication. After sonication, the emulsion was added dropwise into 30 mL 1% (w/v) PVA solution and stirred for 3 h at room temperature to remove the residual organic

solvent. NPs were collected and washed three times with distilled water by centrifugation at 10,000 × g for 5 min at 4 °C, and stored at −80 °C until further use.

3.4.2. CpG nanoparticle fabrication

CpG ODN 1826 (Invitrogen) was resuspended in endotoxin-free TE buffer at 4ug/uL. For nanoparticle preparation, CpG ODN was diluted as needed and mixed with a solution of LPEI-*g*-PEG (LPEI average Mn = 20kDa, PEG average Mn = 0.5kDa, custom fabrication, CreativePEGWorks), at 3:1 v:v, to reach a final concentration of 3.2ug/μLCpG at specified final N/P ratio (ratio of amine in LPEI to phosphate in DNA) for characterization. The solutions were mixed by rapid pipetting followed by vortexing for 20 seconds and incubated at room temperature for at least 15 min before further use. To crosslink nanoparticles, a small volume of DTSSP (Thermo Fisher, cat# 21578) was added to the nanoparticle solution at a 50% crosslinking density (sulfo-NHS ester groups in DTSSP to amine groups in LPEI) and incubated for at least an additional 15 min before further use.

3.4.3. Nanoparticle charge, size, and salt stability characterization

Nanoparticle zeta potential was measured using a Zetasizer Nano ZS90 (Malvern Instruments, Southborough, MA). An aliquot of 5 μg of DNA nanoparticle solution was diluted to 800 μL with DI water or 150 mM sodium chloride, added to a DTS1070-folded capillary cell, and measured in the automatic mode.

To test the size and stability in physiological ionic strength solution, a predetermined volume of 5 M NaCl solution was added to a 100 μg DNA dose nanoparticle solution to give a final NaCl concentration of 150 mM. The same volume of DI water was added for control samples. The mixture solution was incubated for 15 min, and then particle size was measured using dynamic light scattering method with a Zetasizer Nano ZS90. To test the stability in serum,

we incubated an aliquot of nanoparticle solution containing 5 μg of DNA with fetal bovine serum (FBS) at a final serum concentration of 5% (v/v) for 15 min before measuring the particle size.

3.4.4. Gel electrophoresis

A 7% TRIS gel was used to check encapsulation of CpG ODN in nanoparticles. The gel was run in TAE buffer with 25μLof each sample containing 5μg of CpG alone or in nanoparticles with different N:P ratios. A 10 min incubation in TAE buffer containing ethidium bromide was used to visualize the CpG ODN using a Bio-Rad Universal Hood II Gel Documentation System. Lack of CpG band moving through the gel was used as an indication of successful encapsulation of CpG within nanoparticles.

3.4.5. Incorporation of cargo into MAP precursor microgels

Microfluidic fabrication of microparticles was carried out as described in chapter 2 using the D-MMP sensitive peptide as crosslinker and KQRGD conjugated PEG-VS. To incorporate proteins or drug-laden PLGA nanoparticles into MAP particles, the PEG-VS precursor solution was spiked with the antigen or protein of choice or PLGA nanoparticles containing coumarin at a high concentration to reach a desired final concentration of 1 ug/μL for OVA, 0.1ug/μL CpG, and 1.5mg/mL PLGA after 2-fold dilution in droplet generator, 2.5 fold dilution by swelling, and 1.5 fold dilution because of sphere packing in the MAP scaffold. In the case of PLGA particles the solution was also spiked with 0.25% w/v hyaluronic acid (HA700kDa, Lifecore Biomedical, LLC) to improve uniform distribution of nanoparticles and prevent precipitation by increasing viscosity of the solution.

The MAP-CpG particles were fabricated similarly to MAP-Ag particles with the following adjustments: A microfluidic droplet generator with three water phase inlets was used to mix 1) the CpG or CpG nanoparticle solution, 2) KQRGD functionalized PEG-VS and

antigen, and 3) the D-MMP crosslinker. Polymer, antigen, and crosslinker concentrations in the precursor solutions were increased to account for the dilution by the added nanoparticle solution volume.

3.4.6. OVA and CpG release kinetics characterization

To characterize the release of OVA and CpG, MAP gels were fabricated using the above methods FITC-conjugated OVA in place of OVA, and FITC-conjugated CpG ODN in place of CpG ODN. After washing microgels back to the water phase, 100µLaliquots of packed spheres were added to 1.5mL microfuge tubes, mixed with a 1mL of Ca/Mg++PBS with or without collagenase II 100mU/mL, and placed on a tube rotator set to 20rpm at 37˚C (n=4 each group). At different timepoints, particles were pelleted with centrifuge, and a 100µLaliquots of the supernatant were used along with standard concentration solutions to determine the concentration of the released cargo, using a plate reader (excitation: 490nm, emission 525nm, 10nm bandwidth).

3.4.7. DADLE release kinetics characterization

To study the DADLE release from hydrogels, a similar method as before was used for acquiring samples at each time point. HPLC followed by mass spectroscopy was used to determine the concentration of DADLE against standard concentration solutions.

3.4.8. PLGA nanoparticle containing microgel degradation and drug release

To study the degradation profile of PLGA laden MAP gels, 100µLof pelleted MAP gels containing coumarin-6-PLGA nanoparticle was incubated with 1 mL of collagenase at concentrations ranging from 1.6mU/mL to 1U/mL in DPBS with calcium and magnesium on a tube rotator set to 20 rpm at 37˚C (n=4 each group). Three days later hydrogels were centrifuged at 6000rpm for 5 min, and 200µLof each supernatant along with standard concentration solutions

were transferred to a 96-well plate for measuring the released coumarin-6 (excitation: 485 nm, emission: 528 nm, 10nm bandwidth) and AF-568 (excitation: 578, emission: 603nm) using a plate reader as surrogates for drug release and hydrogel degradation, respectively. The hydrogels were then washed three times with PBS, and a small sample was pushed through a 110μm*110μm square microfluidic channel and imaged with fluorescent microscopy to measure the remaining drug and AF-568 as well as the deformability of the hydrogels.

Chapter 4. VaxMAP: immunomodulatory injectable biomaterial for tunable vaccines

4.1. Introduction

Successful vaccines have been developed against non-mutating pathogens like measles, however, vaccines against mutating pathogens such as influenza only elicit a single serotype-specific protective memory response[74]. Current vaccine adjuvants such as alum combine with antigen to create a short-lived antigen depot[75]. A recent successful strategy in HIV has utilized an extended delivery time vaccination method, as it more closely mimics a natural acute infection[76]. Thus, the development of a vaccine delivery system that allows for control of adjuvant and antigen release kinetics may induce an improved pathogen-specific recall response.

SARS-CoV-2, the novel coronavirus that emerged in December 2019 in Wuhan, China, through zoonotic spread from bats[77] is yet another example of a mutating virus that has caused a devastating pandemic worldwide[78]. This pandemic resulted in a global effort for application of established vaccination strategies as well as development of novel platforms at an unprecedented pace, and has allowed a large scale comparison of the safety and efficacy of different platforms against the same pathogen. The most rapid programs were nucleic acid-based which proved to be effective. These vaccines can readily be mass produced and have been proven to be safe and effective[79,80]; however, they require two dosages, their long-term safety remains to be studied, and depending on the delivery vehicle require burdensome storage. More importantly, recent data suggests that sera from subjects receiving these vaccines have slightly reduced activity against the South African variant compared to the Wuhan strain in a surrogate neutralization assay[81] which signals that with additional accumulation of mutations, a resistant strain could emerge in near future. Furthermore, the transient side effects of mRNA vaccines have been more

severe than traditional vaccines. A large portion of the recipients have reported systemic side effects forcing them to take time off work. While this level of side effects is acceptable in a rare pandemic such as Covid-19, it will limit the adoption of this vaccine platform by physicians and patients in other cases.

Another major type of vaccines developed for Covid-19 were vectored vaccines. Since the viral vector (adenovirus) is a virus, the antibodies produced have a higher likelihood to induce antibody dependent enhancement (ADE) of inflammation since they are likely to be type 1 and engage pro-inflammatory Fc receptors[82]. The current vector vaccines being attempted by Johnson & Johnson and AstraZeneca were in clinical trials for SARS, MERS, Zika, and Ebola, but there are zero vector vaccine products approved for those infections or any other indication. While the vectored vaccines approved in Covid-19 pandemic have proven to be generally safe except for rare connections with blot clots, they demonstrated much lower efficacy than mRNA vaccines, especially to the mutant versions of the virus.

Live attenuated virus vaccines, such as MMR vaccine, provide a broad antigenic profile and induce a strong and long-lasting immunity, but typically require several boosters, have potential risk for causing disease in certain subpopulations, and their production is limited by the necessitation of biosafety facilities.

The most common vaccine approach, recombinant or inactivated protein vaccines, have the potential to be produced in extremely large quantities but are typically adjuvanted with alum or oil in water emulsions (such as squalene), thus generally result in poor immunity, especially cell-mediate immunity, and require multiple boosters to get the desired protective immunity[75]. Of note, Novavax (NVX-CoV2373), composed of a trimeric spike glycoprotein adjuvanted with a potent Matrix-M1 adjuvant has shown great efficacy against SARS-CoV-2, it requires easy

storage conditions, and causes less side effects compared to mRNA platforms, in terms of both frequency and severity. Despite all the outstanding progress, outbreaks generally continue until herd immunity is obtained or an effective treatment is developed. An adjuvant strategy, capable of synergizing with current antigen technologies to induce the proper function of important T and B cell populations could result in a more effective vaccine that delivers protective immunity, and potentially requires a single dose to accomplish the protective immunity.

High-affinity neutralizing antibodies and memory B cells generated in a germinal center (GC) reaction are hallmarks of the humoral response[83]. The formation of GCs requires the development of a subset of $CD4^+$ T cells known as follicular helper T (Tfh) cells. Tfh cells function to secrete cytokines (IL-21, and IL-4 or IFN-γ) and soluble factors (CD40L) essential for GC B cell proliferation and survival, immunoglobulin affinity selection, and development of memory B and long-lived plasma cells[83–88]. Within the GCs, B cells undergo a Darwinian selection process based on their ability to capture antigen from follicular dendritic cells and present to Tfh cells[89,90]. The GC B cells that acquire more antigen to present to Tfh cells will receive stimulation and be instructed to undergo further affinity maturation or differentiate into a memory B cell or plasma cell[90–92].

Tfh cell delivered cytokines are necessary for B cell generation of the appropriate antibody isotype. Antigen-primed dendritic cells program Tfh cells to provide B cells with either the type 1 inflammatory cytokine IFN-γ or the type 2 inflammatory cytokine IL-4 to instruct class switching to IgG2c or IgG1, respectively[93,94]. Switching to the appropriate antibody isotype is critical for effective pathogen clearance. IgG2c has a Fc region that preferentially interacts with complement components and activates critical antiviral effector functions including the stimulation of antibody-dependent cell-mediated cytotoxicity and opsonization by

macrophages[95,96]. Conversely, the type 2 inflammatory IgG1 is more suited for neutralizing secreted proteins produced by invading extracellular pathogens. Moreover, the Fc portion of IgG1 antibodies mediates a lower-affinity interaction with Fc receptors in comparison with IgG2c, with less effective receptor stimulation and consequent reduction in inflammatory responses[97].

In chapter 2, we showed that by loading antigen into MAP gel (D-amino acids) we can elicit an adaptive immune response without providing further adjuvants[98]. In chapter 3, we showed the ability of MAP to provide sustained delivery of ovalbumin, as well as CpG when incorporated into LPEI nanoparticles. In this chapter we present work on combined local delivery of adjuvants and antigens with this cutting-edge biomaterial, by incorporating both in the fabrication process of MAP scaffold precursor microgels (**Figure 4-1**). VaxMAP is injectable, possesses porosity that enables immediate immune cell infiltration and antigen presentation. Here we evaluate the VaxMAP in inducing germinal centers and directing the humoral immune response towards either type 1 or type 2 response. We further investigate the ability of VaxMAP to direct differential responses to two antigens within one injection.

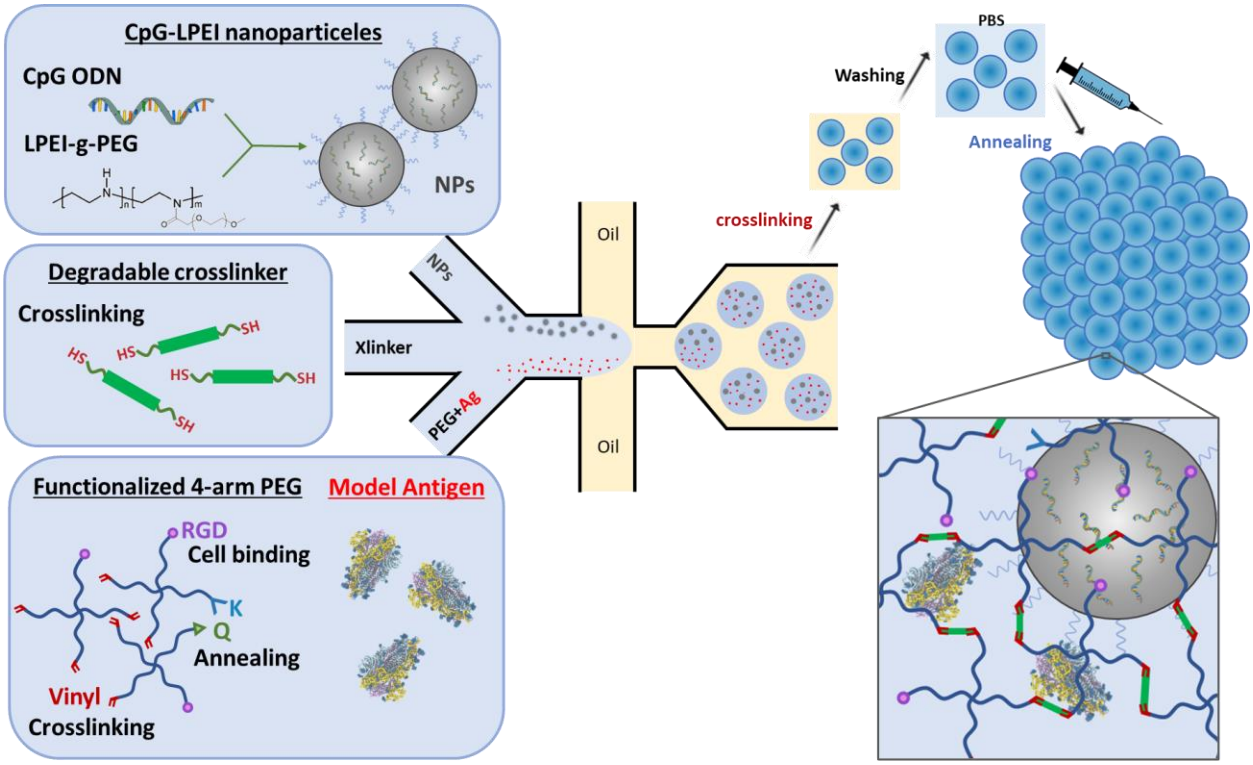

Figure 4-1 VaxMAP components and fabrication process. VaxMAP building blocks are generated by mixing pre-gel solutions inside a microfluidic droplet generator. The droplets are polymerized to form loaded microgel beads by crosslinking functionalized 4-arm-PEG-vinylsulfone molecules via thiol-ene reactions to encapsulate antigen, and optionally CpG loaded nanoparticles (NPs) in the dense gel mesh. Matrix metalloproteinase (MMP) degradable peptide linkers enable the degradation and sustained release of antigen and adjuvants. K and Q peptides allow annealing the microbeads to form a solid scaffold, and RGD peptides allow cell binding.

4.2. Results and discussion

4.2.1. LPEI-CpG nanoparticles retain CpG activity and activate other response pathways

As a first attempt to tune innate immune responses to MAP hydrogel, we determined whether the LPEI-CpG nanoparticles we developed could stimulate transcriptional activation in bone marrow derived macrophage cultures. We chose the Class B/Type G CpG1826 that is similar to the CpG used in approved human vaccines. We stimulated macrophage with LPEI polymer alone, 10ug/ml CpG, 10 ug/ml CpG encapsulated in LPEI nanoparticles (NP), and 10mg/ml CpG in LPEI nanoparticles crosslinked with DTSSP (XL). Not surprisingly, we found that in WT Macrophages, CpG activated expression of TLR9/MyD88 dependent cytokines, but

not type I interferon (IFN-I) genes (**Figure 4-2a**). The encapsulation of CpG in LPEI nanoparticles in some cases increased the production of these cytokines up to two-fold over that of CpG alone. The CpG nanoparticles were also capable of IFN-1 response (Rsad2) which is not a previously known function of CpG DNA (**Figure 4-2a**). Further investigating these results, we found that the LPEI polymer alone was able to activate IFN-I. This was amplified by when polymer and DNA were delivered together in the form of nanoparticles, and even more so with cross linked nanoparticles. LPEI nanoparticles used for delivery of plasmid DNA are believed to provide endosomal escape by buffering protons, leading to accumulation of chloride ions and osmotic lysis of the endosome (the proton sponge effect).[99] This suggested that the CpG ODN in the presence of polymer was allowing the DNA to activate another pathway to induce IFN-I. We further treated wild type and $Sting^{Gt/Gt}$ BMDMs with the same formulations, to see whether cGAS-Sting pathway is involved. Indeed, we found that while cGAS/Sting signaling did not participate in inflammatory gene (TNFa) induction to CpG formulations, Sting ablation reversed the expression of the IFN-I dependent genes (IFIT1) in response to the nanoparticle formulations or polymer alone (**Figure 4-2b**). Of note, cross-linking the CpG (XL) resulted in diminished TNFa induction but enhanced Sting dependent IFN-I induction. While cGAS can bind ssDNA, it does so with much lower affinity than that for dsDNA and as such, unlike the observation reported here, ssDNA has not been capable of stimulating cGAS enzymatic activity in other studies.[100] The efficacy of LPEI nanoparticles in cytoplasmic delivery of CpG at high concentration could be the mechanism behind this observation. These results suggest the ability to tune PRR sensor utilized for recognition of CpG DNA by the LPEI nanoparticles.

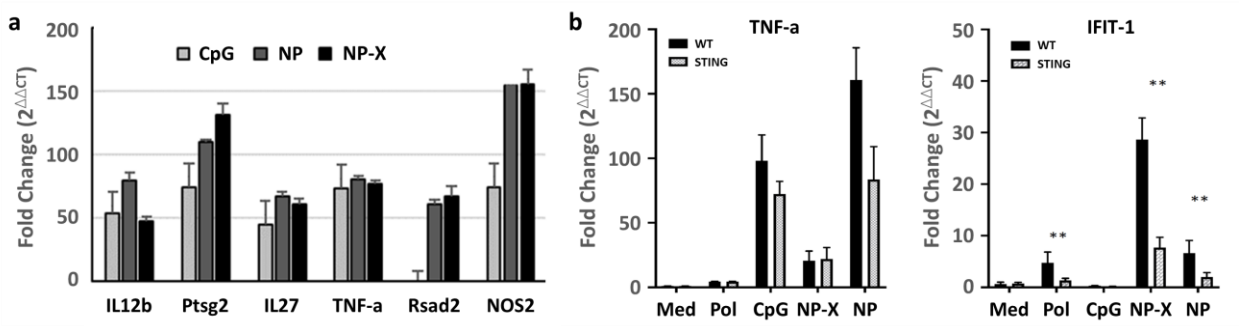

Figure 4-2 Expression of inflammatory genes in mouse bone marrow derived macrophages. a) Relative expression of IL12b, Ptsg2, IL27, TNG-a, Rsad2, and NOS2 in WT BMDMs treated with CpG, CpG-LPEI nanoparticles (NP), or crosslinked CpG-LPEI nanoparticles (NP-X). **b)** relative expression of TNF-a and IFIT-1 in WT and Sting$^{Gt/Gt}$ BMDMs treated with media (Med), LPEI polymer (Pol), CpG, NP-X, and NP. **P<0.01.

4.2.2. MAP induces a GC response similar to Alum and CFA on day 14.

To characterize the ability of antigen loaded VaxMAP to generate an antigen-specific immune response, we compared NP-OVA loaded VaxMAP, to NP-OVA in Complete Freund's Adjuvant (CFA) or alum. C57BL/6 mice were immunized subcutaneously (s.c.) with 100µLof either i) VaxMAP ii) CFA, a well-established immunization model, iii) alum, a traditional vaccine adjuvant or iv) PBS. All groups, with the exception of PBS, contained 50µg of NP-OVA as a model antigen. Mice were sacrificed 14 days after immunization, the peak of Tfh and GC B cell development, respectively. At day 14 post immunization, the percentage of splenic Tfh cells ($CD4^{+}CD44^{+}PSGL\text{-}1^{lo}Ly6c^{lo}CXCR5^{hi}PD\text{-}1^{hi}$) that developed in mice receiving VaxMAP was similar to that of mice immunized with CFA and alum (**Figure 4-3A**). At day 14 post immunization, the percentage of GC B cells ($B220^{+}IgD^{lo}GL\text{-}7^{hi}CD95^{hi}$) in mice receiving VaxMAP was similar to cells from mice immunized with CFA and alum (**Figure 4-3B**).

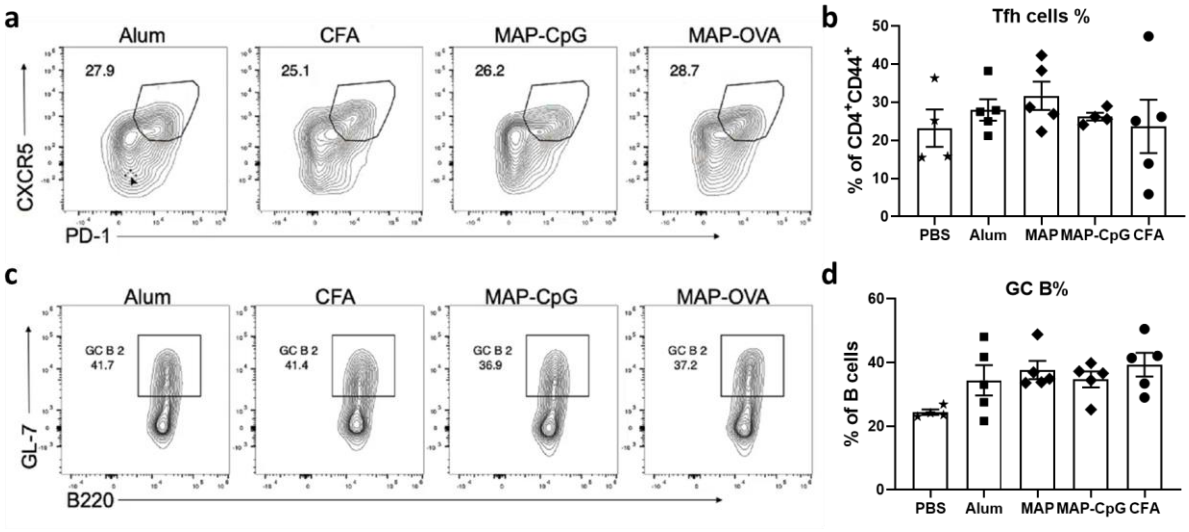

Figure 4-3 Characterization of germinal center response in B6 mice vaccinated with NP-OVA vaccine formulations on day 14. a-b) Representative flow cytometry plots (a) and quantification (b) of germinal center follicular helper T cells as a percent of $CD4^+CD44^+$ cells in spleen. **c-d)** Representative flow cytometry plots (c) and quantification (d) of germinal center B cells as a percent of total B cells in spleen.

4.2.3. MAP can synergize with CpG ODN adjuvants to induce an antibody response superior to alum and comparable to CFA.

To assess the functionality of the GC responses, we analyzed the production of low and high affinity NP-specific antibodies from the sera of mice 14 days after immunization (**Figure 4-4).** VaxMAP immunization induced similar levels of high and low affinity IgG1 anti-NP antibodies compared to sera from CFA and superior to that of alum (**Figure 4-4**, **Figure B-1**). This illustrated that injection of VaxMAP elicited a humoral response better than other adjuvants. Next, to assess the effects of additional adjuvants within the VaxMAP platform, we encapsulated the type 1 adjuvant CpG in nanoparticles along with NP-OVA as in Aim 1. Mice immunized with VaxMAP-CpG had a similar percentage of Tfh cells and GC B cells compared to VaxMAP immunized mice (**Figure 4-3A**). VaxMAP-CpG immunization generated similar levels of the type 1 isotype anti-NP IgG1 to mice immunized with VaxMAP or CFA (**Figure 4-4b**). However, mice immunized with VaxMAP-CpG had significantly increased amounts of high

affinity type 2 isotype anti-NP IgG2c compared to all other immunized mice (**Figure 4-4c, Figure B-2**). Taken together, these data demonstrate that VaxMAP promotes a comparable or better primary humoral response compared to current clinical adjuvants. Furthermore, addition of CpG to our VaxMAP increased class switching to the type 2 IgG2c. Thus, the VaxMAP is a tunable vaccine delivery system that allows for control of adjuvant, antigen, and kinetics, capable of generating a better secondary humoral response.

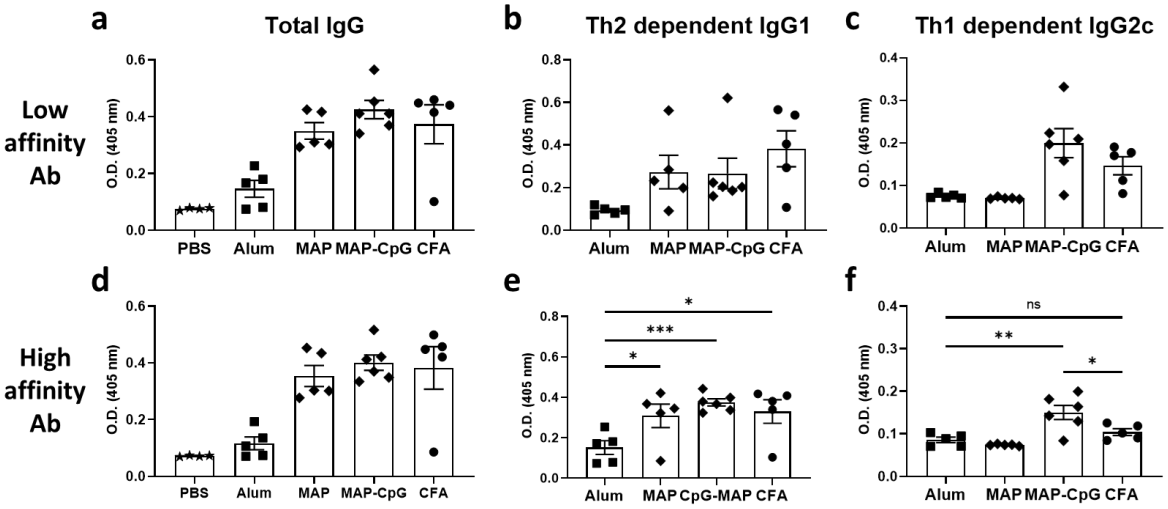

Figure 4-4 Comparison of MAP with different vaccination platforms in inducing NP-specific antibodies on day 14. a-f) Concentration of low (a-c) and high (d-f) affinity anti-NP IgG (a,d), IgG1 (b,e), and IgG2c (c,f) antibodies, in serum of B6 mice on day 14 post vaccination with NP-OVA adjuvanted with MAP, MAP-CpG, using PBS, Alum, and CFA as controls. Affinity was determined by capture with NP(20)-BSA and NP(6)-BSA in ELISA. Each point represents the average of two technical replicated from one mouse.

4.2.4. Spatial resolution of microparticles in MAP scaffolds is possible within a single injection.

While MAP is flowable, it is made of solid particles that, when densely packed, do not move across each other, potentially enabling macroscale spatial separation of different types of hydrogels within a syringe as well as the scaffold after injection. This can be exploited to deliver multiple antigens colocalized with different adjuvants, within one vaccine injection, while

incorporating different adjuvants with each antigen. To test this, we sequentially loaded a syringe with two MAP gels labeled with two fluorescent dyes and quantified the marginal percentage of each gel during injection. While a regular needle with large dead space, did not provide ideal isolation, reaching only 70% isolation (**Figure 4-5a, c**), using a low dead-space needle we could reach 90% separation between the two types of hydrogels in a 100µLMAP scaffold injection (**Figure 4-5b, c**). This means that adding just a 10% spacer MAP gel in between two gels, could readily provide 100% isolation using regular syringes available in research setting. Furthermore, due to the small size of laboratory mice, we could only use 25gauge needles for injection. The possibility for the use of larger bore needles in human, in addition to improving loading method in commercial production, will significantly reduce the mixing of the particles as the pass through the syringe.

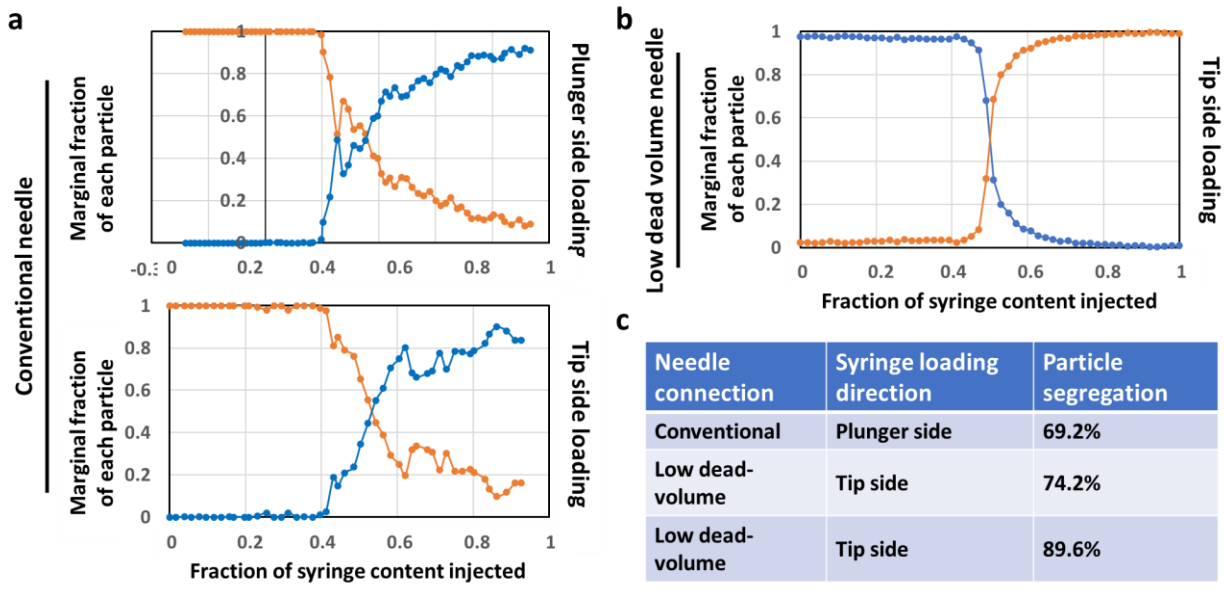

Needle connection	Syringe loading direction	Particle segregation
Conventional	Plunger side	69.2%
Low dead-volume	Tip side	74.2%
Low dead-volume	Tip side	89.6%

Figure 4-5 Assessment of spatial resolution of two MAP gels following syringe loading and injection. a) marginal fraction of each particle in the injected MAP slurry using conventional needles with two directions of syringe loading. **b)** marginal fraction of each particle in the injected MAP slurry using low dead volume needles. **c)** quantification of the particle segregation in the injected scaffolds.

Although we showed that sequential loading of syringes will allow the two particle types to maintain their spatial resolution following injection, for practical purposes in a small-scale research facility, in the two antigen injections presented below we implanted microgels under the skin sequentially using separate syringes. However, we ensured formation of one single bulge under the skin after injection, excluding animals that did not fit this. We also assessed the hydrogel scaffold directly after removing the skin at the endpoint and excluded animals which showed two separate scaffolds.

4.2.5. Spatial resolution of microparticles in MAP scaffold enables induction of a differential immune response to two antigens within a single immunization.

In section 4.2.3 we showed that loading CpG along with NP-OVA changes the dominant antibody isotype from a type 2 IgG1 to a type 1 IgG2c. To investigate the ability of MAP to direct a differential immune response to two antigens within a single vaccination based on spatial resolution of co-encapsulated CpG we fabricated four types of MAP gels: with either OVA or NP-CGG as the antigen, and either unadjuvanted or adjuvanted with CpG nanoparticles (**Figure 4-6a-b**). Using these four MAP gels, we produced two different types of MAP vaccine formulations, each containing MAP gels with one different antigens, one with and one without CpG. In one group, the CpG was colocalized with OVA, and in the other it was colocalized with the NP.CGG, as shown in **Figure 4-6b**. As control, we used a mixture of OVA and NP.CGG adjuvanted with alum, but as alum is completely fluid and cannot provide spatial resolution, we vaccinated one group with CpG adjuvanted alum vaccine, and another without CpG (**Figure 4-6c**).

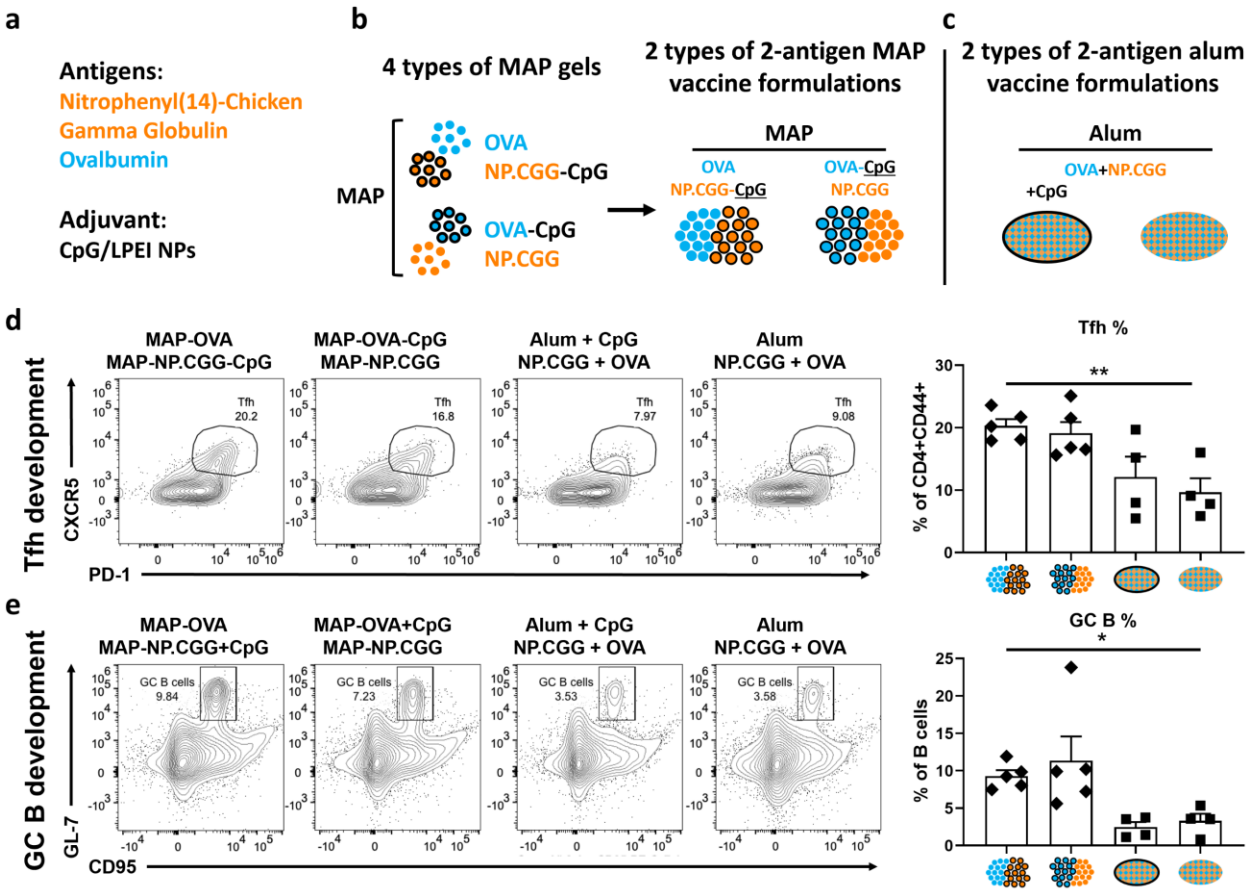

Figure 4-6 Comparison of MAP and alum in inducing germinal center response in B6 mice vaccinated with double antigen formulations on day 28 post immunization. a) antigens and adjuvant included in the vaccine formations. **b)** the MAP precursor fabrication and 2-antigen MAP vaccine formulations. c) 2-antigen alum vaccine formulations. **d)** Representative flow cytometry plots (left) and quantification (right) of germinal center follicular helper T cells as a percent of $CD4^{+}CD44^{+}$ cells in spleen. **e)** Representative flow cytometry plots (left) and quantification (right) of germinal center B cells as a percent of total B cells in spleen.

As opposed to the GC development on day 14 post vaccination, which was similar between MAP and alum vaccines, on day 28 post vaccination, MAP vaccines promoted a more robust Tfh cell and GC B cell development than alum (**Figure 4-6d-e**). The germinal centers in the spleen of mice vaccinated with MAP were also larger and higher in number compared to the mice vaccinated with alum formulations (**Figure B-4**). This shows that MAP can support the GC response for longer, which can lead to higher affinity antibodies and a potentially a stronger memory response. This is likely achieved by the prolonged delivery of the antigen through MAP,

while the antigen in alum is more rapidly depleted leading to a more rapid termination of the GC response.

In the assessment of humoral response, CpG loaded alum induced a similar titer of high affinity, and slightly higher titer of low affinity anti-NP IgG2c antibodies compared to alum and MAP not adjuvanted with CpG (**Figure 4-7c-d**, right panel). CpG loaded MAP containing NP-CGG induced higher anti-NP IgG2c titers compared to CpG loaded alum. This change to type 1 response was limited to NP-CGG, colocalized with CpG, and was not extended to OVA (**Figure 4-7b**), confirming MAP's ability to direct differential immune response to two antigens within one injection. Specifically, the titer of high affinity anti-NP IgG2c antibodies in the mice that were immunized with vaccine formulations containing the CpG-MAP-NP-CGG particles was well above other formulations (**Figure 4-7c-d, right panel**). As for anti-OVA antibodies, while impact of CpG colocalization was not as clear as it was for anti-NP antibodies, MAP gels loaded with OVA, consistently induced a higher titer of both anti-OVA IgG1 antibodies compared to alum formulations (**Figure 4-7b**). It is noteworthy that the MAP formulation with CpG colocalized with NP-CGG lead to a higher number of activated CD8+ T cells compared to alum formulations with or without CpG (**Figure B-3b**), highlighting the capacity of MAP in inducing a cytotoxic response when combined with proper adjuvants.

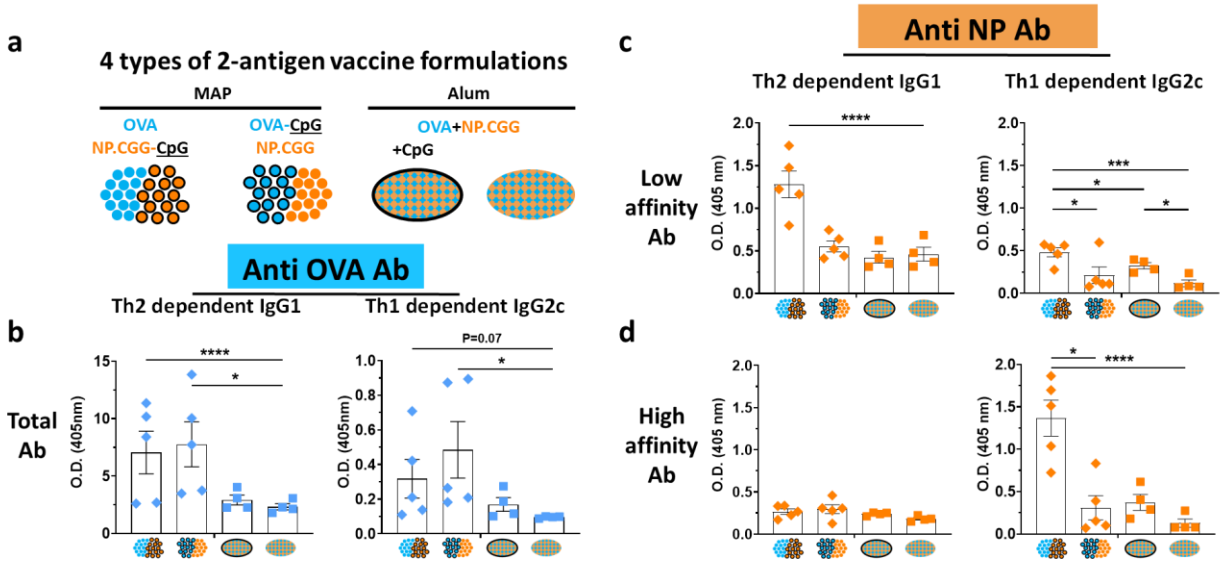

Figure 4-7 Quantification of the differential antibody response from collocalization with CpG adjuvant in 2-Ag formulations in MAP vs. alum on day 28. a) schematic of the 2-Ag vaccine formulations showing the antigens and their colocalization with CpG adjuvant in each formulation. **b)** Concentration of anti-OVA IgG1 (left), and IgG2c (right) antibodies, in serum of B6 mice on day 28 post vaccination. **c-d)** Concentration of low (c) and high (d) affinity anti-NP IgG1 (left), and IgG2c (right) antibodies, in serum of B6 mice on day 28 post vaccination. Affinity was determined by capture with NP(27)-BSA and NP(9)-BSA in ELISA. Each point represents the average of two technical replicated from one mouse.

4.3. Conclusion

MAP gels provide an injectable vaccine platform to leverage innovative and synthetic controlled release technology for sustained delivery, highly porous structure for rapid immune cell infiltration, and large surface area to maximize antigen and adjuvant uptake by infiltrating antigen presenting cells. Thus, delivery of antigen by MAP gel will allow for an extended primary humoral response yielding higher affinity and better neutralizing antibodies, with a decreased need for boosters. MAP can also synergize with other adjuvant technologies to change the type of immune response to antigens. MAP gel's unique geometric structure also enables induction of a differential immune response against multiple antigens within one vaccination, enabling combination of multiple vaccines into one shot. VaxMAP evades the host foreign body

response through IL-33-dependent type 2 immune responses that promote tissue remodeling, where other bulk hydrogel materials cause type 1 immune pathways leading to tissue destruction.[98] VaxMAP's fully synthetic building block materials can be produced at scale and possess a well-established safety profile, enabling rapid translation to a vaccine product. Taken together, these indicate that, unlike other biomaterials demonstrated mostly in academic publications, the VaxMAP platform is highly scalable and translatable to have a real clinical impact in the near term.

4.4. Methods

4.4.1. Macrophage and qPCR study

Bone marrow cell suspension in DMEM with 10%FBS and 1%Pen/Strep supplemented with, L-glutamine and sodium pyruvates was added to each well of 6 well plates (4mL at 0.6 million cells per mL). Media was refreshed on day 4. On day 6, different formulations of 80µg CpG ODN in 20µLwas added to each well and mixed by gentle pipetting. 6 hours post treatment, media was removed and cells in each well were dissolved in 500µLof TRI reagent (MRC). RNA was then isolation using Qiagen RNeasy columns and eluted into 100µLRNAse-free water. 2 µg of RNA was reverse-transcribed using homemade RT mix. cDNA was quantified by real-time PCR using SYBR Green Master Mix (Diagenode) on BioRad Real-time PCR instrument. Gene expression levels were determined by using a standard curve. Each gene was normalized to the housekeeping genes 14433 (GAPDH). PCR amplification was started at 95°C for 3 min followed by 45 cycles of 95°C, 60°C, and 72°C for 15, 30, and 30 seconds, respectively.

4.4.2. VaxMAP fabrication

For all vaccination experiments raw materials were purchased endotoxin free, buffers were sterilized with 200nm filters upon preparation, microparticle fabrication was performed in a

autoclaved enclosed system assembled inside a BSC to maintain sterility, and the final hydrogels were tested for endotoxin levels prior to implantation. Flow-focusing droplet generators were fabricated, as previously described, by soft lithography, and used for microfluidic microgel fabrication. Two aqueous precursor solutions were prepared. One solution contained an 8 mM dicysteine-modified MMP substrate (Ac-GCRDGPQGIWGQDRCG-NH_2) (GenScript) in distilled water. The other solution contained a 10% w/v 20 kDa four-arm polyethylene glycol–vinyl sulfone (PEG-VS, JenKem) in 300 mM triethanolamine (Sigma), pH 8.25, pre-functionalized with a 500 μM K-peptide (Ac-FKGGERCG-NH_2) (GenScript), 500 μM Q-peptide (AcNQEQVSPLGGERCG-NH_2) and 1 mM RGD (Ac-RGDSPGERCG-NH_2) (GenScript). The oil phase was a Novec 7500 Engineered Fluid (3M) that contained 0.2% v/v PicoSurf (Sphere Fluidics). The two solutions were mixed in the droplet generator at equal flow rates of 5 μl min^{-1} and pinched immediately into monodisperse droplets with an oil flow of 75 to 85 μl min^{-1} to produce 73 +/- 3μm particles. The mixture was allowed to react for 4 hours at 37˚C. Oil phase was removed by three washes with a 20mM Tris-buffered saline at pH 7.4 and hexane, and pelleting in a tabletop centrifuge at 2500*g* for 3 min. Before use, the purified hydrogels were imaged to confirm swelling from 73 to 100um size, equivalent to 2.5 swelling in volume, to ensure consistency between fabrications.

For antigen incorporation, NP-OVA was dissolved in TEOA at a high concentration and was added to the PEG-VS solution pre-gel solution to reach a 7.5mg/mL concentration. This provided a 1mg/mL concentration in the MAP gel slurry after a 2-fold dilution in microfluidic fabrication, 2.5 fold dilution in swelling, and 1.5 fold dilution due to sphere packing.

For CpG nanoparticle incorporation along with the antigen, microgels were fabricated similarly to MAP-Ag particles with the following adjustments: A microfluidic droplet generator

with three water phase inlets was used to mix 1) KQRGD functionalized 10% PEG-VS spiked with NP-OVA, 2) 16mM D-MMP peptide, and 3) CpG-LPEI nanoparticle solution with NP ratio of 10 at 1.5mg CpG per mL. The three solutions were mixed in the droplet generator at 5, 2.5, and 2.5 $\mu l\ min^{-1}$, respectively, to provide similar final PEG, antigen, and MMP concentrations, as well as 100ug/mL of CpG in the resulting MAP slurry after swelling.

4.4.3. Preparation of vaccination syringes

For a typical vaccination experiment 500µL of microgel slurry was spiked with 100µL of HEPES buffer containing 3U of FXIII and 2.4U of Thrombin, mixed thoroughly with pipetting and incubated on ice for 30 min. Particles were then centrifuged and 100µL of supernatant was removed to produce a dense microgel pellet containing an assumed final concentration of 5 and 2U/mL of FXIII and thrombin, respectively. Particles were loaded into a 100µL Hamilton GasTight Syringe connected with a 25-gauge low dead volume needle, through the plunger side.

4.4.4. Single antigen mouse immunization experiments

All experiments involving animals, animal cells, or tissues were performed in accordance with the Chancellor's Animal Research Committee ethical guidelines at the University of California Los Angeles under protocol no ARC-2015-125. Ten-week-old C56BL/6J mice (Jackson Laboratory) were shaved on their back the day prior to immunization. On the day, the skin was cleaned with alcohol swabs and 100µL of MAP vaccine was injected subcutaneously. Antigen emulsified with complete Freund's adjuvant, or mixed with Alum (Thermo, Imject), or PBS were used as positive and negative controls.

4.4.5. Assessment of spatial resolution of MAP in one injection

To assess whether two different MAP gels batches can remain separate while being loaded into a single syringe and injected, two batches of original D-MAP gels were fabricated

using the process described above, but by adding 1ug/mL of either Alexa Fluor 568-maleimide or Alexa Fluor 488-maleimide to the crosslinker solution. 1mL BD luer lock syringes with a 5/8" 25G conventional needle (BD, Cat# 305122) or 100µLHamilton GasTight syringe model 1710 RN (Hamilton, Cat# 81030) with a custom 25G 5/8" removable needle was used. Before loading gels, plunger and needle were removed from the syringe body. Using a positive displacement pipette, 50µLof each gel was sequentially loaded into the syringe body. To account for the dead volume of the BD syringe, additional volume of the gel which was placed further away from needle tip was loaded. The plunger and needle were then reassembled. A Harvard Apparatus PHD2000 syringe pump was used to inject the gels blotting a string of hydrogels on a glass slide as they exited the syringe. A cover slip was placed on top to flatten the gels into a monolayer. The slides were then imaged with a fluorescent microscope at a minimum of 50 points along the path. A custom MATLAB script was used to identify gel particles and record the fraction of each gel type, at every point. The following formula was used to calculate the spatial separation:

$$Percent\ separation = 100 * \frac{\sum_{i=1}^{n} \left| \mathrm{F_{i,Gel\#1}} - \mathrm{F_{i,Gel\#2}} \right|}{n}$$

n is the number of points imaged, F is fraction of each gel type at each point.

4.4.6. Two-Ag mouse immunization experiments

For two-antigen immunization we used a similar method as the microgel preparation for single antigen experiments, to fabricate four types of microgels containing OVA or NP-CGG as the antigen, each with and without LPEI-CpG nanoparticles. The antigens concentrations were kept the same but twice the dose of CpG-LPEI nanoparticles was loaded into the microgels containing CpG. For immunizations, Ten-week-old C57BL/6 mice were injected with one of the following formulations: 1) 50µLMAP-OVA + 50µLMAP-NP-CGG-CpG, 2) 50µLMAP-OVA-CpG + 50µLMAP-NP-CGG, 3) Alum containing 50µg of each OVA and NP-CGG, and 4) Alum

containing 50µg of each OVA and NP-CGG and 10µg CpG, to provide the same total antigen and total CpG dosage over all vaccine formulations as the single dose study. To simplify the vaccination procedure and prevent the need for preparation of syringe for each animal, for groups 1 and 2, one type of microgel was first injected subcutaneously, forming a bulge. The second microgel type was then injected in the same spot, ensuring the formation of one single bulge under the skin. To prevent false results due to spatial isolation of two gel types under the skin, if two separate bulges were observed at the time of vaccination, or if two separate MAP scaffolds were identifiable under the skin at the endpoint, the mouse was excluded from the study. Mice were euthanized on day 28 after immunization to quantify Tfh and GC B cells by flow cytometry from spleen. The high- and low- affinity IgG1 (Th2 dependent) and IgG2c (Th1 dependent) antibody titers against NP and OVA in each formulation were also be assessed by ELISA on serum on days 0, 14, and 28.

4.4.7. Collection of blood and splenocytes

To obtain blood, facial vein puncture and cardiac puncture were used to obtain blood for midpoint and endpoint studies, respectively. The blood was then allowed to clot at room temperature for 4 hours, and centrifuged at 10,000rpm for 10 min to separate serum for ELISA. Spleens were harvested and dissociated through a 70-µm-pore-size sterile filter. Splenocyte suspensions were then pelleted with a centrifuge at 300g, treated with erythrocyte lysis by resuspending in ammonium chloride lysis solution for 1 min on ice, then washed twice with PBS, and counted.

4.4.8. Antibody ELISA for NP and Ag

For assessment of antigen specific antibodies, plates were coated with either the antigen, or BSA-NP at 6 or 20 conjugation ratio (GenScript; sequence above). Serum samples were tested

at 1:1000 to 1:25000 dilutions followed by incubation with alkaline phosphatase-labeled goat anti-mouse IgG, IgG1 or IgG2a, or IgG3 antibodies (Southern Biotechnology Associates or BD Pharmingen), and development with p-nitrophenylphosphate substrate (Sigma-Aldrich). Optical density at wavelength of 405 nm was read using a VersaMax microplate reader (Softmax Pro 3.1 software; Molecular Devices).

4.4.9. Spleen GC histology

Spleens were snap frozen in 4% OCT medium, sectioned at 8um thickness, mounted on positively charged glass slides, fixed with ice-cold acetone, rehydrated, and blocked with 5% rat serum, 5% rabbit serum, 3% BSA with 0.1% Tween, and stained with anti IgD (eBiosciences) and anti PNA (Vector Labs) antibodies, followed by secondary staining with streptavidin-AF 555 (Invitrogen), and imaged with a 510 META laser-scanning confocal microscope (Carl Zeiss) at 25× magnification. Germinal center sizes were measured using ImageJ software in a blinded manner.

4.4.10. Splenocyte flowcytometry

Splenocytes were fixed with PFA for 1 min, washed, and stained with flow antibody panels for follicular helper T cells (CD4, CD44, PSGL-1, Ly6c, or CD4, CD44, CXCR5, PD-1) and germinal center B cells (B220, IgD, GL-7, CD95) in PBS containing 1% BSA and 0.1% NaN_3 for 15 minutes in room temperature. All flowcytometry data were obtained using an LSRII Cytometer (BD Biosciences).

Chapter 5. Shaped microparticles for high throughput single-cell functional analysis of antibody secreting cells.

5.1. Introduction

Functional analysis of antibody producing cells (APC) with single cell resolution, while maintaining cell viability for downstream functional analysis and sequencing, is fundamental for both antibody discovery and the study of the biology of humoral response.[101] Antigen specific memory B cells and plasma cells are extremely rare, with frequencies as low as 1 in 1,000 to 1 in 50,000 B cells in lymphoid tissues.[102] As such, techniques for high throughput functional analysis of individual primary APCs are necessary for monoclonal antibody discovery and study of the biology of these cells.

Traditionally, screening of antigen specific B cells for antibody discovery was achieved by the hybridoma technology. The hybridoma technology entails immortalization of primary antibody secreting cells via fusion with myeloma cell lines, followed by their clonal expansion, all prior to assessment of their antigen-specificity. The fusion process has a low yield (0.02%), and together with the need for cell expansion, increases reagent consumption, cost of labor, and the assay's timeline.[103] Furthermore, this method does have the capability for functional or phenotypic analysis of the primary APCs.

The alternative approach for monoclonal antibody discovery is to identify individual antigen-specific APCs which allows for acquisition of antibody gene sequences upstream of the cell line development.[104–109] These approached eliminate the need for cell culture, reduce reagent consumption, and shorten the assay time. However, because of the rarity of antigen-specific APCs, these approaches not only need to be highly sensitive and specific, but also provide a high-throughput. Fluorescence activated cell sorting (FACS) has been widely adopted for sorting

live single cells based on their surface markers but cannot assess cell secretions. Approaches to capture cell secretions on their own surface have been combined with FACS to allow assessment of cell secretions but offer low specificity due to crosstalk between cells.

A few approaches using microscale tools are developed in the past few years, for placing cells into separate compartments and successfully increased assay specificity. However, these have limitations. Microdroplets don't allow iterative reagent exchange so all the reagents needed for a secretion assay must be encapsulated along with cells, necessitating development of special one-step assay formats, such as fluorescent resonance energy transfer.[110,111] Microchamber techniques require manual recovery of identified cells, which increases the labor cost and lowers the throughput.[112] Furthermore, use of these micro-tools require expertise in microfabrication and microfluidics, limiting their widespread adaption. Automated commercial systems that resolve these limitations have been developed but require prohibitively expensive equipment limiting their use to large pharmaceutical companies.[101,113]

Our lab has developed a technology for high throughput single cell secretion analysis using shaped particles.[114] Each microparticle, called nanovial, has the functionality of a well in the well plate format but with a sub-nanoliter volume. The cavity of these cup shaped biotinylated particles (nanovials) can be used for capture and protection of single cells, while their surface enables performing sandwich assays for capture and detection of cell secretions. Fluids are easily exchanged by centrifugation and pipetting, and each compartment can be sealed and unsealed using biocompatible oils to prevent crosstalk between samples. These nanovials are compatible with commercial flow cytometers, enabling performance of the traditional well plate format assays in vials almost the size of a single cell, thereby increasing the throughput of these

assays by 3-4 orders of magnitude with single cell resolution without the need for any new instrumentation.

In this chapter I will present the developed workflow for adopting nanovial technology for the study of antibody secreting cells and discuss the factors impacting the assay. To adopt the nanovial technology I designed the assay for antigen-specific APCs, with changes in the particle fabrication, cell adhesion method, and an assay format for antigen-specific antibody detection shown in **Figure 5-1**. APCs will be seeded on particles and captured using Cell adhesion peptide sequences, electrostatic binding, or CD specific cell capture antibodies. Then uniform water in oil droplets will be formed by emulsifying the cell containing particles to create compartments with individual cells. After cell secretions are captured with antibody capture molecules, the particles are recovered back into water phase, and stained for labeling of antigen specific antibodies. The particles are then analyzed by a commercially available FACS system, and particles containing single cells with antigen specific antibody signal will be sorted individually in 96 or 384 well plate for downstream analysis.

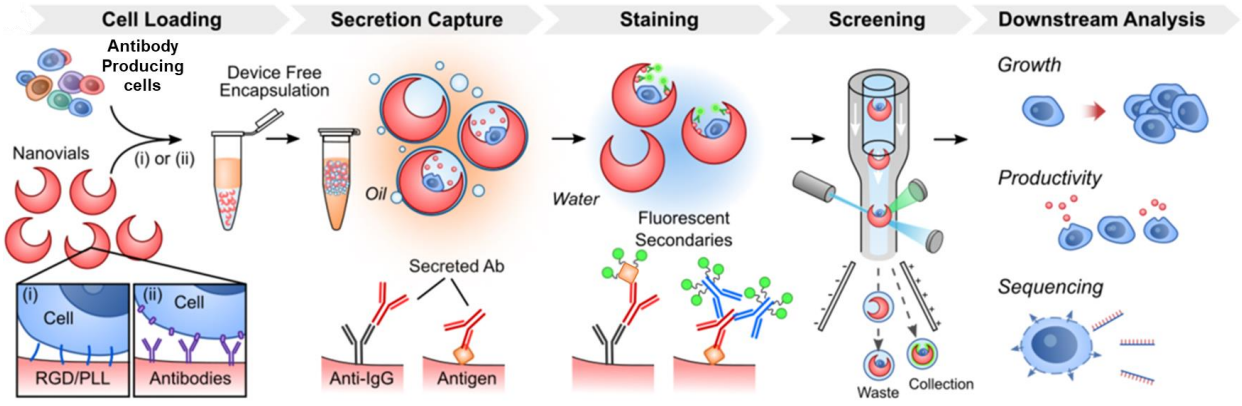

Figure 5-1 Detailed overview of workflow and assay design for selection of antigen specific IgG secreting B-cells for downstream analysis. Streptavidin coated nanovials are incubated with cell and secretion capture sites, and then seeded into a well plate and settle with cavities exposed upright. B cells are then seeded into the exposed cavities and incubated to allow binding. Nanovials and attached cells are transferred to a microcentrifuge tube by pipetting, emulsified to create individual compartments to

prevent crosstalk, and incubated to accumulate antibodies on the surface of the nanovials. The nanovials, cells, and captured secreted antibodies are then transferred back into water phase and captured antibodies are labeled with one of two assay designs for antigen specific antibody detection. Using FACS, nanovials are screened in high-throughput and nanovials with a cell secreting antibody against the antigen of interest are index sorted into separate wells of a well-plate for downstream analysis.

5.2. Results and discussion

5.2.1. Nanovials can bind B cells and plasma cells

B cells and plasma cells are non-adherent cells that, unless activated, do not express many cell adhesion ligands on their surface and as such they do not adhere to the RGD moieties incorporated into the structure of the nanovials for attachment of adherent cells. We tested additional methods for B cell attachment, including coating nanovials with poly L-lysine and fibronectin as well as anti-surface marker antibodies to improve cell adhesion via electrostatic interaction between cell membrane and PLL, or clusters of differentiation and cell capture antibodies. We then loaded particles with B cells isolated from mouse spleen, targeting a 15% loading, and removed unattached cells after incubation using a cell strainer to test binding efficacy. PLL improved cell adhesion only marginally, with most cells successfully loaded into nanoparticles, falling off after washing (**Figure 5-2** left panel), however anti CD19, anti CD45, or a mixture of both, resulted in a robust capture of B cells, almost completely retaining loaded B cells following washing steps (**Figure 5-2**).

5.2.2. One million cell laden nanovials can be sorted in one hour with >90% success rate

To test the cell capture and sorting workflow with B cells, we seeded 35μm diameter coated particles with B cells and sorted them at rate of >250 events/sec. The smaller nanovial sizes were suited to isolate mouse B cells which adhered to anti CD45 antibodies on the particle surface and enabled sorting using a common FACS system, Sony SH800. We were able to sort

500,000 events in half an hour, going from a sample with <5% cell loaded particles, reaching a purity of above 90% cell loaded particles (**Figure 5-2c-d**).

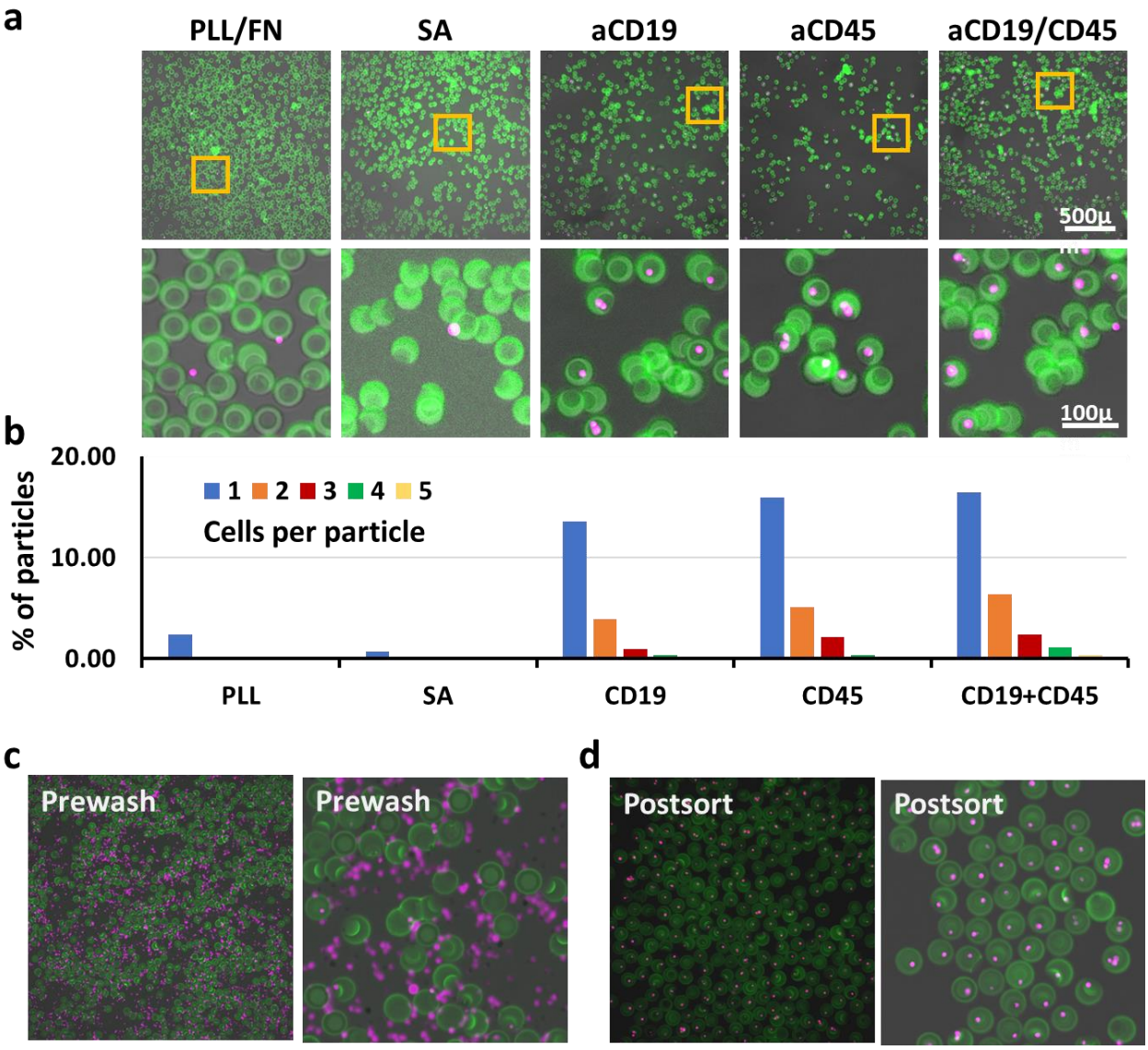

Figure 5-2 Efficacy of different binding methods for loading B-cells into nanovials. a) low (top) and high(bottom) power fluorescent microscopy images of B-cells loaded into nanovials, and **b)** the quantification of the distribution of cell containing particles based on the number of cells per particle following removal of unattached cells. **c-d)** low- and high-resolution image of B cell laden particles at the cell loading stage (c) and after sorting (d).

5.2.3. Considerations in method for capturing B cells with anti-surface marker antibody.

While coating nanovials with biotinylated anti CD45 was effective in capturing B cells, to capture both cells and their secretions, the cell capture and secretion capture antibodies have to be applied to the particles at the same time (**Figure 5-3,** top). So, a point of consideration in the cell binding method is that the competition for available SA sites reduces the density of each cell and secretion capture antibodies on the surface by a factor of two. This can potentially reduce the efficacy of the assay by: 1) reducing the cell binding strength, 2) reducing the maximum capacity for secretion binding, 3) producing false signal if detection of secreted antibodies with an antibody is desired (from cross reactivity of detection antibody with cell capture antibody), and most importantly, 4) accumulation of signal from surrounding cells on particles during the cell binding incubation step. To eliminate these, we performed the cell binding with a different scheme, by first coating cells with biotinylated anti CD45, and adding them to particles coated with streptavidin, and then washing unbound cells and their secretions away, and finally incubating cell laden nanovials with secretion capture antibodies for a short period, before emulsification (**Figure 5-3**, bottom). We observed that this binding scheme had the same cell binding and recovery efficacy when sorting particles loaded with cells (data not shown). This method can especially be beneficial in avoiding false signal accumulation from unbound cells during the cell binding step when working with highly secreting cells such as plasma cells. Furthermore, it allows cell binding based on multiple surface markers using cell capture antibody cocktails without compromising the strength of the binding or sensitivity of the secretion assay.

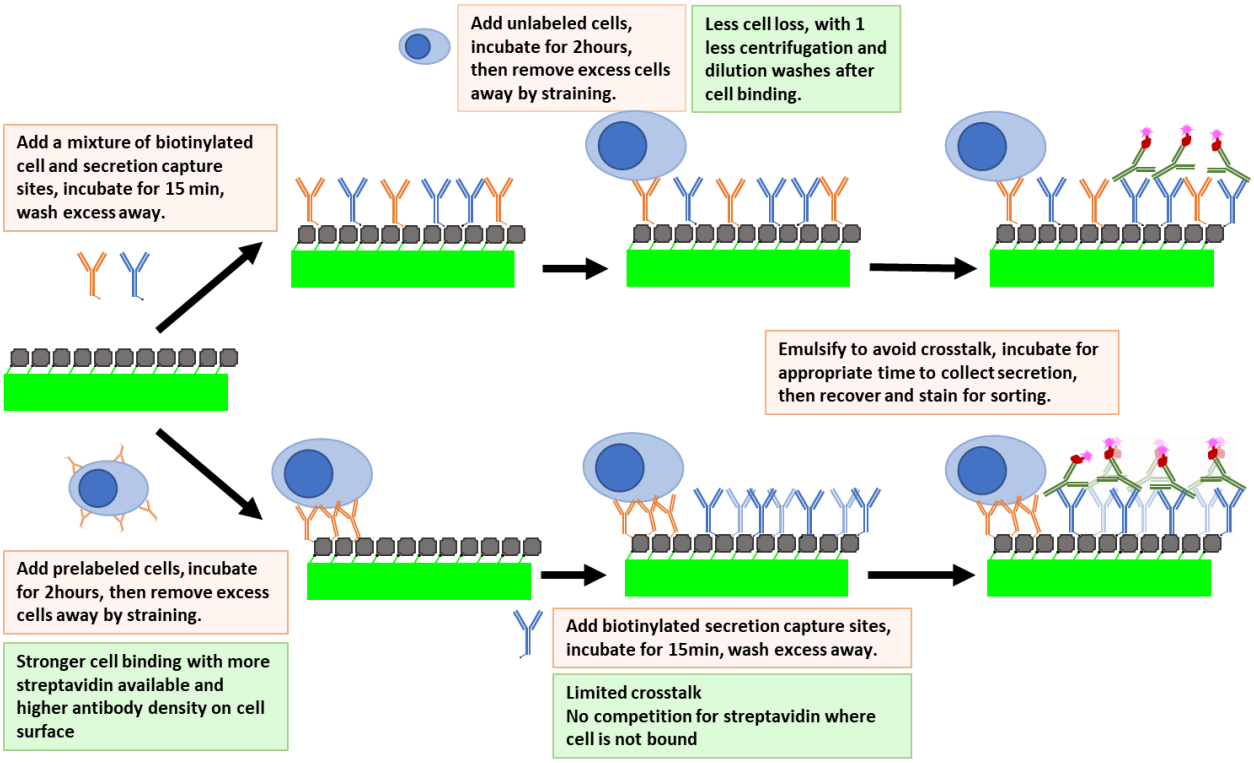

Figure 5-3 Schematic of different B cell binding techniques for the dropicle assay along with advantage and disadvantages of each. Top shows one step particle coating with both cell and secretion capture antibodies followed by loading of B cells. Bottom shows the loading of particles with cells pre-coated with cell capture antibodies, followed by coating with secretion capture antibodies.

5.2.4. A small fraction of the biotin is available at the nanovial surface.

To quantify the absolute biotin availability for analyte capture on nanovials, we first blocked them with increasing streptavidin amounts to block biotin, followed by streptavidin conjugated HRP to bind to any remaining uncovered biotin. Nanovials functionalized with 0.1mg/mL biotin-PEG1k-thiol in the precursor solution, showed a drop in HRP signal when first incubated with about 22 femtomoles (2.5ng) or more of SA per 2µLof initial particle pellet corresponding with 500,000 biotins available for binding on surface of each particle (**Figure 5-4**). Raising the biotin-PEG1k-thiol concentration in precursor solution to 1mg/mL, the nanovials started to show a drop in HRP signal when first incubated with 414 femtomoles (23ng) or more of SA, corresponding to 4.3 million biotins per particle (**Figure 5-4**). Comparing with the

expected concentration of biotin in a nanovial volume, we found that the biotin in about 1.8nm thickness of the nanovials is accessible for binding to streptavidin and larger molecules. The proportional increase in the availability of biotin on nanovials from 2.5 to 23ng with 10 times more biotin-PEG addition to the precursor solution shows the versatility of the system's capacity for applications to analysis of cells with different secretion capacities. To put this number in context, a single plasma cell at optimal condition can produce up to 1000 antibodies per second, saturating the capture sites on a nanovial with the higher biotin concentration in about 1.5 hours.

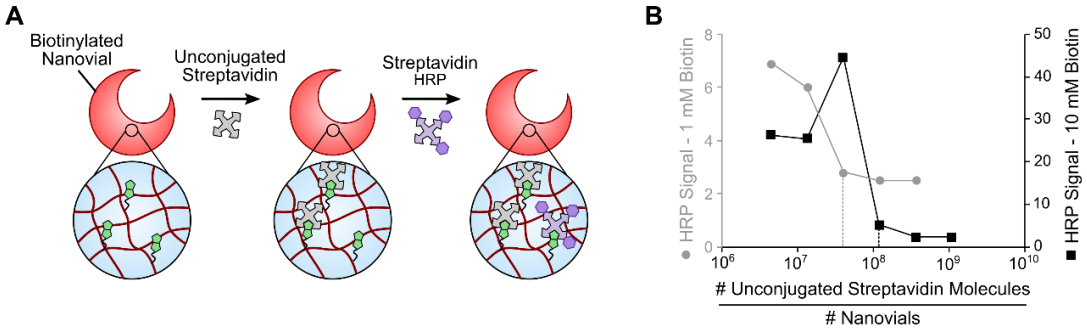

Figure 5-4 Quantification of available biotin groups using HRP colorimetric assay. a) Particles are first coated with unconjugated streptavidin over a range of concentrations. Samples are washed and then incubated with HRP conjugated streptavidin (SA-HRP) at a fixed concentration. After conjugation samples were washed and reacted with a colorimetric HRP substrate (2,2'-Azino-bis(3-ethylbenzothiazoline-6-sulfonic-acid, Sigma-Aldrich). The concentration of reaction product generated from conjugated SA-HRP was measured using a plate reader. **b)** Measured HRP signal vs unconjugated streptavidin concentration for nanovials with 1 and 10 mM biotin groups in the precursor solution. Available biotin groups are saturated with streptavidin at around 4×10^7 and 1.2×10^8 molecules per nanovial for the 1 and 10 mM conditions respectively.

5.2.5. Nanovials can detect antigen specific antibodies at similar levels as ELISA

Using smaller 35µm diameter particles, we applied the dropicle platform for the isolation of B lymphocytes based on secreted IgG. First to assess the dynamic range of nanovials and their limit of detection for antigen specific antibodies we used sera from ovalbumin vaccinated mice. Nanovials coated with antigen were incubated with mice sera diluted from 100 to 2,000,000-fold and stained with fluorescent anti-Mouse IgG H+L antibodies (**Figure 5-5a**). Using fluorescence microscopy, we could detect signal on nanovials from sera diluted up to 20,000-fold (**Figure 5-**

5h and **Figure C-1a**). The sera from non-vaccinated mice had no reactivity with particles at titers as low as 1:10. Assessing the same nanovials with flowcytometry, the limit of detection was increased by roughly 10-fold, detecting antigen specific antibodies from sera of vaccinated mice at 200,000-fold dilution (**Figure 5-5b**, **Figure C-1b**). To put this in context, a single plasma cell encapsulated in a nanovial can produce 0.2 to 20pg of antibodies in a 2-hour incubation time of the assay. The 1:200 and 1:200,000 serum dilutions correspond to 0.03pg to 10pg antibody per particle. This shows that not only nanovials are capable of detecting antigen specific antibody secreting cells but can also differentiate them based on the amount of antibody production. Considering the possibility of non-specific labeling of B cell receptors that might be left on plasma blasts or cross reactivity with cell capture antibodies when staining with anti-Mouse IgG H+L antibodies (**Figure C-3**) we also tested the assay in a reverse setup, by capturing serum antibodies with anti-Mouse IgG coated nanovials, and labeling the antigen specific ones with fluorescent tagged ovalbumin. Using this setup, nanovials could detect antigen specific antibodies in sera from vaccinated mice at dilutions up to 2,000 folds in fluorescence microscopy (**Figure C-2**). The decreased limit of detection here is expected as the non-specific capture method results in most capture sites being occupied by serum antibodies that are not ovalbumin specific.

5.2.6. Nanovials can detect rare antigen specific antibody producing cells

Having established cell binding, as well as sandwich assay format, we performed the full workflow to assess antigen specific antibody secretion by plasma cells isolated from the bone marrow of OVA vaccinated mice. 55µm diameter particles coated with anti CD45 and anti-mouse IgG, for plasma cell binding and antibody capture, respectively, were used. After cell binding, dropicles were formed and incubated at 37C to capture antibody secretions. After

2hours of incubation, particles were transferred back to water and stained with Cy5-conjugated ovalbumin. The antibody signal on the surface of particles containing OVA specific plasma cells, was readily visualized using fluorescence microscopy (**Figure 5-5b**). Some cells appeared brightly stained in the images which were not antibody producing cells, either from reaction their B cell receptors with OVA, or from internalization of OVA via endocytosis (**Figure 5-5b**, bottom row). In these instances, the fluorescent signal made differentiation of particles with cells from empty particles easier on Sony SH800 flow sorter, by moving them higher along the AF-555 height and area components (**Figure 5-5c**, gold box in panel 3). We found that the width of the flow plots can be used to easily differentiate staining on particles from staining on cells. The particles with antibody staining were contained along the upper portion of AF647 width axis and made up 0.4-1% of population (**Figure 5-5b-c**, black box in panel 4). However, a few brightly stained cells were also present in this area. We have since determined the presence of small amount of Pluronic F-127 in our staining medium is the cause for cell membrane permeabilization leading to the non-specific entry of the fluorescent antigen to the cells. Removing the Pluronic from the staining buffer, while mildly increases the sample loss, will eliminated the background staining.

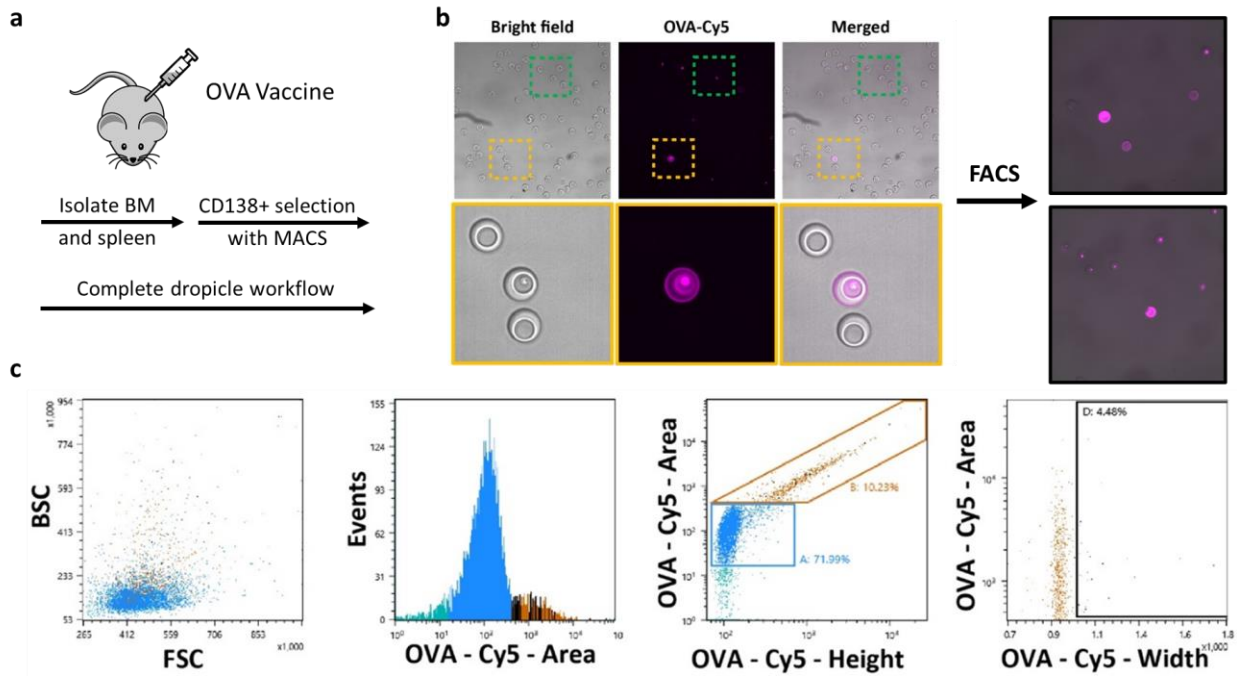

Figure 5-5 Assessment of full dropicle assay workflow for detection and sorting of antigen specific antibody secreting cells. a) Experimental design for the full workflow assay. **b)** Fluorescent and brightfield micrographs of plasma cells after a complete workflow for detection of antigen specific antibody secretion signal via staining with fluorescent antigen. **c)** Flowcytometry plots of the plasma cell containing nanovials after staining.

5.3. Conclusion

In this chapter I showed the workflow for nanovials as a platform for identification and sorting of live antigen-specific APCs. This platform can be used for therapeutic monoclonal antibody discovery by sequencing the antibody messenger RNA of APCs, or downstream iterative phenotypic and functional analysis at single cell resolution. The nanovials provide multiple advantages over other microtools for identification of APCs.

Using the nanovials, isolation of cells into uniform compartments can be done in parallel, as opposed to sequential loading into droplets in microfluidic technologies, which increases the throughput of the assay. The cavity size can be adjusted to limit the number of cells that can be loaded in one particle.

The surface of the nanovials, similar to a streptavidin coated well plate surface, allows both cell binding and performing simple, robust, and highly specific fluorescence linked immunosorbent assays. However, as we have shown the small size of dropicles templated by the nanovials, increases the limit of detection to levels comparable to amplified enzyme linked immunosorbent assays. This allows detection of secretions of a single cell, eliminating the time and resource extensive cell expansion needed in assay formats like hybridoma technology. Furthermore, the surface enables multiplexing for concurrent assessment of antibody affinity for different antigen epitopes or other cell secretions.

Nanovials can be analyzed and sorted with widely accessible FACS instruments enabling screening at rates above 300 events per second. Using this format labs can screen more than 2,000,000 APCs in a single day, demonstrating single-cell analysis for an antibody discovery workflow which can identify rare antibody secreting cells from an order of magnitude more cells than previous approaches all within one day.

Importantly the entire nanovial assay including cell seeding, emulsification, and secretion capture can be done without any expertise in microfluidics or other micro-technologies, only using common place lab equipment and pipetting techniques, and very limited resources. The low cost, high throughput, and ease of performing the nanovial workflow make the antibody discovery process accessible to all biology labs.

The nanovial technology can also be used to study pathways leading to B cell to plasma cell transition by antibody secretion analysis at single cell resolution. The ability to sort live APCs further enables downstream sequencing or phenotypic and secretion analysis to dissect the heterogeneity of these cell populations.

5.4. Methods

5.4.1. Fabrication of biotin coated nanovials

Nanovials were fabricated using a PDMS microfluidic flow focusing droplet generator with two water phase inlets. A PEG solution comprised of 28.9% w/w 4-arm PEG10kDa-norbornene (Sigma), 3% w/w LAP (lithium phenyl-2,4,6-trimethylbenzoylphosphinate,sigma), and 0.1 or 1 mg/ml Biotin-PEG-thiol (5000 MW, Nanocs) in phosphate buffered saline (PBS, pH7.2) was co-injected with a dextran phase comprised of 11% w/w 40 kDa dextran (Sigma), 1.3% w/w DTT (dithiothreitol, Sigma) in PBS at a rates of 0.5 - 5μL/min, depending on nanovials size, using syringe pumps (Harvard Apparatus PHD 2000). An oil phase comprised of Novec 7500 (3M) and 0.25% w/w PicoSurf (Sphere Fluidics) was injected at a rate of 10 - 42μL/min to partition the aqueous phases into monodisperse water and oil droplets. PEG and Dextran polymers phase separated on chip after approximately 5 seconds. The PEG phase was crosslinked with focused UV light through a DAPI filter set and microscope objective (Nikon, Eclipse Ti-S) near the outlet region of the microfluidic device. Crosslinked particles were collected, and oil and dextran were removed using a series of washing steps. Briefly, excess oil was removed by pipetting and a layer of PBS was added on top of the remaining emulsions. A solution of 20% v/v perfluoro octanol (PFO, Sigma) in Novec 7500 was then added to destabilize the emulsions and transfer particles to the PBS phase. Excess oil was removed, and samples were washed twice with Novec 7500 to remove remaining surfactant. Novec 7500 was removed by pipetting and residual oil was removed by washing two to three times with hexane (Sigma). Samples were then washed three times with PBS to remove dextran from the system. For cell experiments particles were sterilized by incubating in 70% Ethanol overnight. Particles were

then washed five times with a storage solution comprised of PBS + 0.1% Pluronic F-127 (Sigma) +1% penicillin/streptomycin (Invitrogen) and stored in a conical tube at 4°C until further use.

5.4.2. Assessment of the accessible biotin on particles

To quantify the number of biotin available per nanovial an HRP ELISA was utilized. Evaluated nanovials were fabricated with 1 or 10 mg Biotin-PEG-thiol per mL of PEG precursor solution. For each condition, 2µL of particles (~58000 particles) were first labeled with various amounts of unconjugated streptavidin ranging from 1 to 31000 ng SA per µL particle solution in 60µL buffer to cap available biotins. After 45 min of incubation, 80 ng SA-3HRP was added to each vial and allowed to incubate an additional 30 min to allow binding to any free biotin. Particles were then washed 5 times with 1 mL PBS containing 0.05% Pluronic and 0.5% Bovine Serum Albumin (BSA), and aliquots of the supernatant of each wash were collected to confirm the level of remaining HRP is not biasing the experiment in any way. Following the last wash particles from each condition were resuspended in 50µL washing buffer and moved to a 96 well plate and mixed with 100µL of HRP substrate. To create a standard curve, 50µL of washing buffer containing known amounts of SA-3HRP from 0.05 to 30 ng were mixed with 100µL of substrate. Reactions were allowed to occur for 25 min on a shaker before proper development was observed. Reaction was stopped with 100µL of 3N NaOH, and the absorbance was measured at 405 nm using a Gen5 plate reader. The high unconjugated SA concentrations was considered to saturate particles, practically not allowing any additional SA-3HRP being adsorbed to the particles, leading to no HRP signal in ELISA. The concentration of unconjugated SA below which the HRP signal started to appear was considered the lowest to saturate the particles and was used to estimate the capacity of particles for binding streptavidin.

To calculate the number of biotin molecules accessible per particle, the thickness of particles where biotin is accessible, and % of biotin in particles accessible the following methods were used, assuming a spherical particle with 35um diameter. This assumption slightly underestimates the surface area of particles, resulting in overestimation of the thickness of particle where biotin is available.

$$AccessibleBiotin_{per\ particle} = \frac{total\ biotin\ measured\ by\ calorimetric\ assay}{particle\ count\ in\ 2uL}$$

$$AccessibleThickness_{per\ particle} = \frac{AccessibleBiotin_{per\ particle}}{4\pi r^2} * \frac{swelling\ ratio}{[biotin]_{precursor}}$$

$$\%BiotinAvailability = 100 * \frac{AccessibleBiotin_{per\ particle}}{\frac{swelling\ ratio}{[biotin]_{precursor}} * \frac{4\pi}{3}(r_{particle}^3 - r_{cavity}^3)}$$

Where $r_{particle}$ and r_{cavity} are the the particle radius and radius of inner cavity, swelling ratio is the ratio of particle volume after swelling to before swelling (1.7x).

5.4.3. Mouse Immunization and B lymphocyte isolation and culture.

All experiments involving animals, animal cells, or tissues were performed in accordance with the Chancellor's Animal Research Committee ethical guidelines at the University of California Los Angeles under protocol no ARC-2015-125. Ten-week-old C56BL/6J mice (Jackson Laboratory) were immunized for a total of 7 times in 28 days with recombinant ovalbumin (Biosearch Technologies) as a model antigen. Immunizations were made by mixing ovalbumin at 1ug/µLin PBS with equal volume of Inject alum adjuvant (ThermoFisher Scientific). 250µg and 25µg doses of ovalbumin were used initial immunization, and subsequent 7 boosters, respectively. 4 days after final immunization, mice were euthanized with isoflurane overdose followed by cervical dislocation and sterilized by spraying with 70% ethanol. for tissue and blood collection. For bone marrow isolation, the mice were submerged in 70% ethanol. The

skin was removed from the lower limbs by making an incision along from the palms to the abdomen, and tibia and femur of both legs were cut from hip and palms. Muscle tissue was then removed, and the four bones were placed in ice cold PBS while processing other mice. The bone ends were cut and the bone marrow was removed by flushing 10 mL of cold PBS through one end using a syringe connected to a 25-gauge needle. The tissue clumps were dissociated by drawing and flushing the solution through the needle 3 times. The isolated cells from up to 4 mice were pooled together, strained through a 70µm cell strainer, and centrifuged at 300g for 10 min at 4C. A 10^8cells/mL suspension of cells was prepared in EasySep buffer (StemCell Technologies, #20144), and plasma cells were isolated using a EasySep mouse CD138 positive selection kit (StemCell Technologies, #18957) according to the manufacturer's protocol. The isolated cell suspensions were then placed on ice until use. For B cell isolation, spleen was removed, cut into small pieces with scissors, and pushed through a 70µm cell strainer in a 10cm petri dish containing 10mL cold PBS, using the plunger of a 10mL syringe. The same syringe was then used to dissociate tissue clumps by drawing and flushing the solution through a 25-gauge needle 3 times. Cells were pelleted by centrifugation at 300g for 10min and resuspended at 10^8 cells/mL in EasySep buffer and B lineage cells were isolated using an EasySep mouse B cell negative isolation kit (StemCell Technologies, #19854). For serum, blood was collected directly from left ventricle via cardiac puncture immediately after euthanasia. Blood was allowed to clot at room temperature for 4 hours, before centrifuging at 10,000 g for 10 min to separate serum.

5.4.4. B cell and Plasma cell cultures

There was an effort made to use plasma and B cells fresh after isolation. Excess cells were frozen in FBS containing 10% DMSO at 1million cells per mL. After thawing, cells were allowed to recover for one hour in media before further use. RPMI, containing 10% FBS, 1% of

each of penicillin/streptomycin, L-Glutamine, HEPES buffer , minimum essential medium nonessential amino acids, sodium pyruvate (ThermoFisher Scientific 15070063, A2916801, 15630130, 11140050, 11360070), and 50µm beta mercaptoethanol. For any incubation time over 1 hour, the plasma cell media was supplemented with IL-6 and APRIL (GenScript Z03189 and Z02969) at 50 and 100ng/mL respectively. Isolated B cells from spleen of vaccinated mice were cultured at 500k cells per mL in vitro for 3 days in media supplemented with LPS and CpG ODN 1826 at 5 and 1µg/µL, respectively.

5.4.5. Cell binding assay

PLL+Fibronectin particles were prepared as mentioned in ExpiCHO cell binding section above. To test capture with anti-surface marker antibodies, particles were first incubated for 10 min with 1µg streptavidin per 1µLparticle solution. Particles were then washed three times and incubated with a solution containing 2ng aCD45, aCD19, or 1:1 mix of aCD45+aCD19 per µL particle solution at 60µg total antibody concentration. Particles were then washed 3X. 8µLof particles were added to each well of a 24 well plate in 2mL washing buffer, followed by addition of 100,000 cells, pre-stained with cell-tracker. The cells were allowed to settle into particle cavities and adhere for 2 hours in cell incubator. The particles were then strained with a 20um cell strainer to remove unattached cells and imaged with fluorescent microscopy or sorted with Sony SH800 FACS system. The fluorescent microscopy images were analyzed using a custom MATLAB algorithm, by first identifying particle centers and radii, along with cell centers in the brightfield and cell tracker fluorescence channel, respectively, followed by counting the number of cells overlapping each particle.

5.4.6. Serum measurements, LOD and Dynamic Range experiments

For assessment of the dynamic range of the on-particle FLISA for antibody capture and detection, 2µLaliquots of particles were used for each condition. To reduce sample loss, as mentioned above, all conical tubes and pipette tips were precoated with washing buffer prior to handling particle containing solutions. Biotinylated particles were labeled with streptavidin (Thermo Fisher, 434302) by adding 150 ng per µL of concentrated particle solution and incubating for 10 min. Samples were then washed three times with washing buffer and resuspended. Particles were then labeled biotinylated goat anti-mouse IgG H&L antibodies with or without biotinylated anti-CD45 and (SouthernBiotech 1034-08, Invitrogen 13045182) by adding 60 ng and 40 ng of the respective antibodies per µL of concentrated particle solution and incubating for 30 min. After incubation, particles were washed and resuspended in washing buffer. Serum, media, or purified antibodies at various concentrations were added to the particles and incubated for 2 hours to allow antibody capture onto the particle matrix via anti-mouse IgG H&L sites. After the incubation period, particles were washed, and captured secretions were stained with Alexa Fluor 647 conjugated ovalbumin (Invitrogen O34784) at a final concentration of 50 ng per µL of initial concentrated particle solution. After 30 min of staining, samples were washed five times with washing buffer. Finally, particles were analyzed by Sony SH800 FACS system or imaged with a fluorescent microscope in both brightfield and fluorescence channels in a well plate. The fluorescent microscopy images were analyzed using a custom MATLAB algorithm, by first identifying particles' centers and radii in the brightfield channel, followed by integrating the secretion label fluorescence intensity in the area of each particle. A similar assay format was also tested for ovalbumin specific antibody capture using a reverse FLISA setup: biotinylated ovalbumin (Nanocs OVA1BN1) as capture site on particles, and Alexa Fluor Plus

555 conjugated goat anti-mouse IgG H&L antibodies (Invitrogen, A32727) for detection, with similar moles of capture and detection molecules as the first ELISA configuration.

5.4.7. Plasma cell secretion assay.

To minimize manipulation of primary plasma cells in antibody secretion assay, particle labeling was performed prior to seeding the cells. To reduce sample loss, as mentioned above, all conical tubes and pipette tips were precoated with washing buffer prior to handling particle containing solutions. Biotinylated particles were labeled with streptavidin (Thermo Fisher, 434302) by adding 150 ng per µL of concentrated particle solution and incubating for 10 min. Samples were then washed three times with washing buffer and resuspended. Particles were then labeled with biotinylated anti-CD45 and biotinylated goat anti-mouse IgG H&L chain antibodies (Invitrogen 13045182 and SouthernBiotech 1034-08) by adding 40 ng and 60ng of the respective antibodies per µL of concentrated particle solution and incubating for 30 min. After incubation, particles were washed and resuspended in EasySep buffer containing IL6 and APRIL, respectively. 9µL of 55µm nanovials and 85000 plasma cells were seeded into a 24-well plate as described above and then incubated at 37°C for 1 hours to allow cells to adhere to the particles. Particles were then recovered by tilting the well plate and transferring by pipetting. To remove unattached cells from the background, samples were strained using a 37 or 20µm reversible cell strainer for 55 and 35µm particles, respectively (STEMCELL Technologies or Partec North America CELLTRICS) and then particles were recovered by flipping the cell strainer and washing with washing buffer. After recovering, samples were concentrated by centrifuging particles and associated cells at 300 g for 3 min, aspirating, and then resuspending in 1 mL EasySep buffer containing IL6 and APRIL. After re-suspending, samples were compartmentalized by pipetting with oil and surfactant as described above to create dropicles.

Samples were then incubated for 2 hours to allow cells to secrete and to facilitate capture of secreted antibodies onto the associated particle matrix via goat anti-mouse IgG H&L sites. After the incubation period, particles and associated cells were transferred back into media by breaking the emulsions. Samples were then washed, and captured secretions were stained with Alexa Fluor 647 conjugated ovalbumin (Invitrogen O34784) at a final concentration of 50 ng per µL of initial concentrated particle solution. After 30 min of staining, samples were washed three times with a large volume of EasySep buffer and optionally stained with propidium iodide. An aliquot of the sample was then either sorted using a Sony SH800 FACS system or imaged with a fluorescent microscope in both brightfield and fluorescence channels in a well plate for quality control, or analysis in MATLAB.

5.4.8. Assessment of cell binding using cell capture antibody on cells

Coating cells with capture antibody, rather than addition of capture antibody to particles, was tested as an alternative method for cell binding. To do so, biotinylated anti-CD45 antibodies and cell tracker were added to the cell suspension prior to seeding them on particles. After three washes in PBS, cell-capture antibody coated cells were seeded on streptavidin coated particles, prepared as above, and allowed to settle and adhere for 2 hours. The unattached cells were then removed by straining, and particles were incubated with biotinylated goat anti-mouse IgG H&L chain antibodies for 15 min prior to washing excess antibodies away with three additional washes. The particles were then sorted, and binding efficacy was compared with the method described in section 5.4.5 using particles coated with a 1:1 mix of biotinylated anti-CD45 and biotinylated goat anti-mouse IgG H&L chain antibodies, by counting the percentage of particles that were positive for cell tracker signal.

REFERENCES

1. Trojaniello, C., Luke, J. J. & Ascierto, P. A. Therapeutic Advancements Across Clinical Stages in Melanoma, With a Focus on Targeted Immunotherapy. *Front Oncol* **11**, 670726 (2021).
2. Moslehi, J. J., Salem, J.-E., Sosman, J. A., Lebrun-Vignes, B. & Johnson, D. B. Increased reporting of fatal immune checkpoint inhibitor-associated myocarditis. *The Lancet* **391**, 933 (2018).
3. Francis, D. M. & Thomas, S. N. Progress and opportunities for enhancing the delivery and efficacy of checkpoint inhibitors for cancer immunotherapy. *Advanced Drug Delivery Reviews* **114**, 33–42 (2017).
4. Rosenblum, M. D., Gratz, I. K., Paw, J. S. & Abbas, A. K. Treating Human Autoimmunity: Current Practice and Future Prospects. *Science Translational Medicine* **4**, 125sr1-125sr1 (2012).
5. Rowley, A. T., Nagalla, R. R., Wang, S.-W. & Liu, W. F. Extracellular matrix-based strategies for immunomodulatory biomaterials engineering. *Adv Healthc Mater* **8**, e1801578 (2019).
6. Kumar, M., Gupta, P., Bhattacharjee, S., Nandi, S. K. & Mandal, B. B. Immunomodulatory injectable silk hydrogels maintaining functional islets and promoting anti-inflammatory M2 macrophage polarization. *Biomaterials* **187**, 1–17 (2018).
7. Ali, O. A., Huebsch, N., Cao, L., Dranoff, G. & Mooney, D. J. Infection-mimicking materials to program dendritic cells in situ. *Nature Mater* **8**, 151–158 (2009).
8. Irvine, D. J., Stachowiak, A. N. & Hori, Y. Lymphoid tissue engineering: Invoking lymphoid tissue neogenesis in immunotherapy and models of immunity. *Seminars in Immunology* **20**, 137–146 (2008).

9. Andorko, J. I. & Jewell, C. M. Designing biomaterials with immunomodulatory properties for tissue engineering and regenerative medicine. *Bioeng Transl Med* **2**, 139–155 (2017).
10. Engineering an Artificial T-Cell Stimulating Matrix for Immunotherapy - PubMed. https://pubmed.ncbi.nlm.nih.gov/30968468/.
11. Vassey, M. J. *et al.* Immune Modulation by Design: Using Topography to Control Human Monocyte Attachment and Macrophage Differentiation. *Advanced Science* **7**, 1903392 (2020).
12. Gentile, P., Chiono, V., Carmagnola, I. & Hatton, P. V. An Overview of Poly(lactic-co-glycolic) Acid (PLGA)-Based Biomaterials for Bone Tissue Engineering. *Int J Mol Sci* **15**, 3640–3659 (2014).
13. Liu, H., Slamovich, E. B. & Webster, T. J. Less harmful acidic degradation of poly(lactic-co-glycolic acid) bone tissue engineering scaffolds through titania nanoparticle addition. *Int J Nanomedicine* **1**, 541–545 (2006).
14. Fenton, O. S. *et al.* Injectable Polymer–Nanoparticle Hydrogels for Local Immune Cell Recruitment. *Biomacromolecules* **20**, 4430–4436 (2019).
15. Bencherif, S. A. *et al.* Injectable preformed scaffolds with shape-memory properties. *PNAS* **109**, 19590–19595 (2012).
16. Bencherif, S. A. *et al.* Injectable cryogel-based whole-cell cancer vaccines. *Nat Commun* **6**, 7556 (2015).
17. Harris, L. D., Kim, B. S. & Mooney, D. J. Open pore biodegradable matrices formed with gas foaming. *J Biomed Mater Res* **42**, 396–402 (1998).

18. Verbeke, C. S. & Mooney, D. J. Injectable, Pore-Forming Hydrogels for In Vivo Enrichment of Immature Dendritic Cells. *Advanced Healthcare Materials* **4**, 2677–2687 (2015).
19. Goonoo, N. Modulating Immunological Responses of Electrospun Fibers for Tissue Engineering. *Adv Biosyst* **1**, e1700093 (2017).
20. Moore, K. M. *et al.* Injectable, Ribbon-Like Microconfetti Biopolymer Platform for Vaccine Applications. *ACS Appl. Mater. Interfaces* **12**, 38950–38961 (2020).
21. Nguyen, T. L., Choi, Y. & Kim, J. Mesoporous Silica as a Versatile Platform for Cancer Immunotherapy. *Adv Mater* **31**, e1803953 (2019).
22. Cauda, V., Schlossbauer, A. & Bein, T. Bio-degradation study of colloidal mesoporous silica nanoparticles: Effect of surface functionalization with organo-silanes and poly(ethylene glycol). *Microporous and Mesoporous Materials* **132**, 60–71 (2010).
23. Hotaling, N. A., Tang, L., Irvine, D. J. & Babensee, J. E. BIOMATERIAL STRATEGIES FOR IMMUNOMODULATION. *Annu Rev Biomed Eng* **17**, 317–349 (2015).
24. Jones, L. H. Recent advances in the molecular design of synthetic vaccines. *Nature Chem* **7**, 952–960 (2015).
25. Pagels, R. F. & Prud'homme, R. K. Polymeric nanoparticles and microparticles for the delivery of peptides, biologics, and soluble therapeutics. *J Control Release* **219**, 519–535 (2015).
26. Ding, D. & Zhu, Q. Recent advances of PLGA micro/nanoparticles for the delivery of biomacromolecular therapeutics. *Mater Sci Eng C Mater Biol Appl* **92**, 1041–1060 (2018).
27. Wang, X., Niu, D., Hu, C. & Li, P. Polyethyleneimine-Based Nanocarriers for Gene Delivery. *Curr Pharm Des* **21**, 6140–6156 (2015).

28. Abdelaziz, M. H. *et al.* Alternatively activated macrophages; a double-edged sword in allergic asthma. *Journal of Translational Medicine* **18**, 58 (2020).
29. Bloise, N. *et al.* Engineering Immunomodulatory Biomaterials for Regenerating the Infarcted Myocardium. *Front Bioeng Biotechnol* **8**, 292 (2020).
30. Sadtler, K. *et al.* Developing a pro-regenerative biomaterial scaffold microenvironment requires T helper 2 cells. *Science* **352**, 366–370 (2016).
31. Dellacherie, M. O. *et al.* Single-Shot Mesoporous Silica Rods Scaffold for Induction of Humoral Responses Against Small Antigens. *Advanced Functional Materials* **30**, 2002448 (2020).
32. Ali, O. A., Tayalia, P., Shvartsman, D., Lewin, S. & Mooney, D. J. Inflammatory Cytokines Presented from Polymer Matrices Differentially Generate and Activate DCs In Situ. *Advanced Functional Materials* **23**, 4621–4628 (2013).
33. Griffin, D. R., Weaver, W. M., Scumpia, P., Di Carlo, D. & Segura, T. Accelerated wound healing by injectable microporous gel scaffolds assembled from annealed building blocks. *Nat Mater* **14**, 737–744 (2015).
34. Nih, L. R., Sideris, E., Carmichael, S. T. & Segura, T. Injection of Microporous Annealing Particle (MAP) Hydrogels in the Stroke Cavity Reduces Gliosis and Inflammation and Promotes NPC Migration to the Lesion. *Adv. Mater. Weinheim* **29**, (2017).
35. Xu, Q. *et al.* Injectable hyperbranched poly(β-amino ester) hydrogels with on-demand degradation profiles to match wound healing processes. *Chem. Sci.* **9**, 2179–2187 (2018).
36. Zhu, S., Nih, L., Carmichael, S. T., Lu, Y. & Segura, T. Enzyme-Responsive Delivery of Multiple Proteins with Spatiotemporal Control. *Adv. Mater. Weinheim* **27**, 3620–3625 (2015).

37. Sela, M. & Zisman, E. Different roles of D-amino acids in immune phenomena. *FASEB J.* **11**, 449–456 (1997).

38. Doloff, J. C. *et al.* Colony stimulating factor-1 receptor is a central component of the foreign body response to biomaterial implants in rodents and non-human primates. *Nat Mater* **16**, 671–680 (2017).

39. Mishra, P. K. *et al.* Sterile particle-induced inflammation is mediated by macrophages releasing IL-33 through a Bruton's tyrosine kinase-dependent pathway. *Nature Materials* **18**, 289–297 (2019).

40. Chung, L., Maestas, D. R., Housseau, F. & Elisseeff, J. H. Key players in the immune response to biomaterial scaffolds for regenerative medicine. *Adv. Drug Deliv. Rev.* **114**, 184–192 (2017).

41. Galiano, R. D., Michaels, J., Dobryansky, M., Levine, J. P. & Gurtner, G. C. Quantitative and reproducible murine model of excisional wound healing. *Wound Repair Regen* **12**, 485–492 (2004).

42. Ito, M. *et al.* Wnt-dependent de novo hair follicle regeneration in adult mouse skin after wounding. *Nature* **447**, 316–320 (2007).

43. Seifert, A. W. *et al.* Skin shedding and tissue regeneration in African spiny mice (Acomys). *Nature* **489**, 561–565 (2012).

44. Nelson, A. M. *et al.* dsRNA Released by Tissue Damage Activates TLR3 to Drive Skin Regeneration. *Cell Stem Cell* **17**, 139–151 (2015).

45. Guerrero-Juarez, C. F. *et al.* Wound Regeneration Deficit in Rats Correlates with Low Morphogenetic Potential and Distinct Transcriptome Profile of Epidermis. *J. Invest. Dermatol.* **138**, 1409–1419 (2018).
46. Marshall, C. D. *et al.* Sanativo Wound Healing Product Does Not Accelerate Reepithelialization in a Mouse Cutaneous Wound Healing Model. *Plast. Reconstr. Surg.* **139**, 343–352 (2017).
47. Lim, C. H. *et al.* Hedgehog stimulates hair follicle neogenesis by creating inductive dermis during murine skin wound healing. *Nat Commun* **9**, 4903 (2018).
48. Carlson, M. A. & Chakkalakal, D. Tensile properties of the murine ventral vertical midline incision. *PLoS ONE* **6**, e24212 (2011).
49. Plikus, M. V. *et al.* Regeneration of fat cells from myofibroblasts during wound healing. *Science* **355**, 748–752 (2017).
50. Guerrero-Juarez, C. F. *et al.* Single-cell analysis reveals fibroblast heterogeneity and myeloid-derived adipocyte progenitors in murine skin wounds. *Nat Commun* **10**, 650 (2019).
51. Warren, K. S. A functional classification of granulomatous inflammation. *Ann. N. Y. Acad. Sci.* **278**, 7–18 (1976).
52. Chensue, S. W. *et al.* Cytokine responses during mycobacterial and schistosomal antigen-induced pulmonary granuloma formation. Production of Th1 and Th2 cytokines and relative contribution of tumor necrosis factor. *Am. J. Pathol.* **145**, 1105–1113 (1994).

53. Wills-Karp, M. *et al.* Trefoil factor 2 rapidly induces interleukin 33 to promote type 2 immunity during allergic asthma and hookworm infection. *J. Exp. Med.* **209**, 607–622 (2012).

54. Hardman, C. S., Panova, V. & McKenzie, A. N. J. IL-33 citrine reporter mice reveal the temporal and spatial expression of IL-33 during allergic lung inflammation. *Eur J Immunol* **43**, 488–498 (2013).

55. de Kouchkovsky, D. A., Ghosh, S. & Rothlin, C. V. Induction of sterile type 2 inflammation. *Nat Mater* **18**, 193–194 (2019).

56. Koh, J. *et al.* Enhanced In Vivo Delivery of Stem Cells using Microporous Annealed Particle Scaffolds. *Small* **15**, e1903147 (2019).

57. Purbey, P. K. *et al.* Defined Sensing Mechanisms and Signaling Pathways Contribute to the Global Inflammatory Gene Expression Output Elicited by Ionizing Radiation. *Immunity* **47**, 421-434.e3 (2017).

58. Scumpia, P. O. *et al.* Opposing roles of Toll-like receptor and cytosolic DNA-STING signaling pathways for Staphylococcus aureus cutaneous host defense. *PLoS Pathog* **13**, (2017).

59. Tong, A.-J. *et al.* A Stringent Systems Approach Uncovers Gene-Specific Mechanisms Regulating Inflammation. *Cell* **165**, 165–179 (2016).

60. Kim, S. D. *et al.* The agonists of formyl peptide receptors prevent development of severe sepsis after microbial infection. *J. Immunol.* **185**, 4302–4310 (2010).

61. Kang, H. K. *et al.* The synthetic peptide Trp-Lys-Tyr-Met-Val-D-Met inhibits human monocyte-derived dendritic cell maturation via formyl peptide receptor and formyl peptide receptor-like 2. *J. Immunol.* **175**, 685–692 (2005).

62. Schepetkin, I. A. *et al.* 3-(1H-indol-3-yl)-2-[3-(4-nitrophenyl)ureido]propanamide enantiomers with human formyl-peptide receptor agonist activity: molecular modeling of chiral recognition by FPR2. *Biochem. Pharmacol.* **85**, 404–416 (2013).
63. Zisman, E., Dayan, M., Sela, M. & Mozes, E. Ia-antigen-T-cell interactions for a thymus-independent antigen composed of D amino acids. *Proc Natl Acad Sci U S A* **90**, 994–998 (1993).
64. Cernysiov, V., Gerasimcik, N., Mauricas, M. & Girkontaite, I. Regulation of T-cell-independent and T-cell-dependent antibody production by circadian rhythm and melatonin. *Int. Immunol.* **22**, 25–34 (2010).
65. Honda, S. *et al.* Enhanced humoral immune responses against T-independent antigens in Fc alpha/muR-deficient mice. *Proc. Natl. Acad. Sci. U.S.A.* **106**, 11230–11235 (2009).
66. Mongini, P. K., Stein, K. E. & Paul, W. E. T cell regulation of IgG subclass antibody production in response to T-independent antigens. *J. Exp. Med.* **153**, 1–12 (1981).
67. Weinstein, J. S. *et al.* Maintenance of anti-Sm/RNP autoantibody production by plasma cells residing in ectopic lymphoid tissue and bone marrow memory B cells. *J. Immunol.* **190**, 3916–3927 (2013).
68. Germann, T. *et al.* Interleukin-12 profoundly up-regulates the synthesis of antigen-specific complement-fixing IgG2a, IgG2b and IgG3 antibody subclasses in vivo. *European Journal of Immunology* **25**, 823–829 (1995).
69. Boehler, R. M., Graham, J. G. & Shea, L. D. Tissue engineering tools for modulation of the immune response. *BioTechniques* **51**, 239–240, 242, 244 passim (2011).

70. Song, J. *et al.* A mouse model for the human pathogen Salmonella typhi. *Cell Host Microbe* **8**, 369–376 (2010).

71. Park, C. G. *et al.* Extended release of perioperative immunotherapy prevents tumor recurrence and eliminates metastases. *Sci Transl Med* **10**, (2018).

72. Kim, J. *et al.* Injectable, spontaneously assembling, inorganic scaffolds modulate immune cells in vivo and increase vaccine efficacy. *Nature Biotechnology* **33**, 64–72 (2015).

73. Ramirez-Carrozzi, V. R. *et al.* A unifying model for the selective regulation of inducible transcription by CpG islands and nucleosome remodeling. *Cell* **138**, 114–128 (2009).

74. Green, S. & Rothman, A. Immunopathological mechanisms in dengue and dengue hemorrhagic fever. *Curr. Opin. Infect. Dis.* **19**, 429–436 (2006).

75. HogenEsch, H. Mechanisms of stimulation of the immune response by aluminum adjuvants. *Vaccine* **20 Suppl 3**, S34-39 (2002).

76. Cirelli, K. M. *et al.* Slow Delivery Immunization Enhances HIV Neutralizing Antibody and Germinal Center Responses via Modulation of Immunodominance. *Cell* **180**, 206 (2020).

77. Rothan, H. A. & Byrareddy, S. N. The epidemiology and pathogenesis of coronavirus disease (COVID-19) outbreak. *J Autoimmun* **109**, 102433 (2020).

78. Zhou, P. *et al.* A pneumonia outbreak associated with a new coronavirus of probable bat origin. *Nature* **579**, 270–273 (2020).

79. Baden, L. R. *et al.* Efficacy and Safety of the mRNA-1273 SARS-CoV-2 Vaccine. *New England Journal of Medicine* **384**, 403–416 (2021).

80. Polack, F. P. *et al.* Safety and Efficacy of the BNT162b2 mRNA Covid-19 Vaccine. *New England Journal of Medicine* **383**, 2603–2615 (2020).

81. Tada, T. *et al.* Neutralization of viruses with European, South African, and United States SARS-CoV-2 variant spike proteins by convalescent sera and BNT162b2 mRNA vaccine-elicited antibodies. *bioRxiv* (2021) doi:10.1101/2021.02.05.430003.

82. Iwasaki, A. & Yang, Y. The potential danger of suboptimal antibody responses in COVID-19. *Nature Reviews Immunology* 1–3 (2020) doi:10.1038/s41577-020-0321-6.

83. Weinstein, J. S. *et al.* TFH cells progressively differentiate to regulate the germinal center response. *Nat. Immunol.* **17**, 1197–1205 (2016).

84. Xu, J. *et al.* Mice deficient for the CD40 ligand. *Immunity* **1**, 423–431 (1994).

85. Liu, D. *et al.* T-B-cell entanglement and ICOSL-driven feed-forward regulation of germinal centre reaction. *Nature* **517**, 214–218 (2015).

86. Zotos, D. *et al.* IL-21 regulates germinal center B cell differentiation and proliferation through a B cell-intrinsic mechanism. *J Exp Med* **207**, 365–378 (2010).

87. Lee, S. K. *et al.* Interferon-γ excess leads to pathogenic accumulation of follicular helper T cells and germinal centers. *Immunity* **37**, 880–892 (2012).

88. Roco, J. A. *et al.* Class-Switch Recombination Occurs Infrequently in Germinal Centers. *Immunity* **51**, 337-350.e7 (2019).

89. Mesin, L., Ersching, J. & Victora, G. D. Germinal Center B Cell Dynamics. *Immunity* **45**, 471–482 (2016).

90. Shulman, Z. *et al.* Dynamic signaling by T follicular helper cells during germinal center B cell selection. *Science* **345**, 1058–1062 (2014).

91. Gitlin, A. D., Shulman, Z. & Nussenzweig, M. C. Clonal selection in the germinal centre by regulated proliferation and hypermutation. *Nature* **509**, 637–640 (2014).

92. De Silva, N. S. & Klein, U. Dynamics of B cells in germinal centres. *Nat Rev Immunol* **15**, 137–148 (2015).

93. Thieu, V. T. *et al.* Signal transducer and activator of transcription 4 is required for the transcription factor T-bet to promote T helper 1 cell-fate determination. *Immunity* **29**, 679–690 (2008).

94. Weinstein, J. S. *et al.* STAT4 and T-bet control follicular helper T cell development in viral infections. *J. Exp. Med.* **215**, 337–355 (2018).

95. Takai, T., Li, M., Sylvestre, D., Clynes, R. & Ravetch, J. V. FcR gamma chain deletion results in pleiotrophic effector cell defects. *Cell* **76**, 519–529 (1994).

96. Kipps, T. J., Parham, P., Punt, J. & Herzenberg, L. A. Importance of immunoglobulin isotype in human antibody-dependent, cell-mediated cytotoxicity directed by murine monoclonal antibodies. *J. Exp. Med.* **161**, 1–17 (1985).

97. Hewitson, J. P. *et al.* Concerted activity of IgG1 antibodies and IL-4/IL-25-dependent effector cells trap helminth larvae in the tissues following vaccination with defined secreted antigens, providing sterile immunity to challenge infection. *PLoS Pathog.* **11**, e1004676 (2015).

98. Griffin, D. R. *et al.* Activating an adaptive immune response from a hydrogel scaffold imparts regenerative wound healing. *Nature Materials* 1–10 (2020) doi:10.1038/s41563-020-00844-w.

99. Sonawane, N. D., Szoka, F. C. & Verkman, A. S. Chloride accumulation and swelling in endosomes enhances DNA transfer by polyamine-DNA polyplexes. *J Biol Chem* **278**, 44826–44831 (2003).

100. Kranzusch, P. J., Lee, A. S.-Y., Berger, J. M. & Doudna, J. A. Structure of human cGAS reveals a conserved family of second-messenger enzymes in innate immunity. *Cell Rep* **3**, 1362–1368 (2013).

101. Winters, A. *et al.* Rapid single B cell antibody discovery using nanopens and structured light. *MAbs* **11**, 1025–1035 (2019).

102. Amanna, I. J. & Slifka, M. K. Quantitation of Rare Memory B Cell Populations by Two Independent and Complementary Approaches. *J Immunol Methods* **317**, 175–185 (2006).

103. Schmitt, J. J., Zimmermann, U. & Neil, G. A. Efficient generation of stable antibody forming hybridoma cells by electrofusion. *Hybridoma* **8**, 107–115 (1989).

104. Tiller, T. *et al.* Efficient generation of monoclonal antibodies from single human B cells by single cell RT-PCR and expression vector cloning. *Journal of Immunological Methods* **329**, 112–124 (2008).

105. Tiller, T., Busse, C. E. & Wardemann, H. Cloning and expression of murine Ig genes from single B cells. *Journal of Immunological Methods* **350**, 183–193 (2009).

106. Dekosky, B. J. *et al.* High-throughput sequencing of the paired human immunoglobulin heavy and light chain repertoire. *Nature Biotechnology* **31**, 166–169 (2013).

107. DeKosky, B. J. *et al.* In-depth determination and analysis of the human paired heavy- and light-chain antibody repertoire. *Nature Medicine* **21**, 86–91 (2015).

108. Mcdaniel, J. R., DeKosky, B. J., Tanno, H., Ellington, A. D. & Georgiou, G. Ultra-high-throughput sequencing of the immune receptor repertoire from millions of lymphocytes. *Nature Protocols* **11**, 429–442 (2016).

109. Parola, C., Neumeier, D. & Reddy, S. T. Integrating high-throughput screening and sequencing for monoclonal antibody discovery and engineering. *Immunology* vol. 153 31–41 (2018).

110. Eyer, K. *et al.* Single-cell deep phenotyping of IgG-secreting cells for high-resolution immune monitoring. *Nat Biotechnol* **35**, 977–982 (2017).

111. Bounab, Y. *et al.* Dynamic single-cell phenotyping of immune cells using the microfluidic platform DropMap. *Nat Protoc* **15**, 2920–2955 (2020).

112. Jin, A. *et al.* A rapid and efficient single-cell manipulation method for screening antigen-specific antibody–secreting cells from human peripheral blood. *Nat Med* **15**, 1088–1092 (2009).

113. Josephides, D. *et al.* Cyto-Mine: An Integrated, Picodroplet System for High-Throughput Single-Cell Analysis, Sorting, Dispensing, and Monoclonality Assurance. *SLAS TECHNOLOGY: Translating Life Sciences Innovation* **25**, 177–189 (2020).

114. Massively parallel encapsulation of single cells with structured microparticles and secretion-based flow sorting | bioRxiv. https://www.biorxiv.org/content/10.1101/2020.03.09.984245v1.

115. Ellis, L. Z., Cohen, J. L. & High, W. Granulomatous reaction to silicone injection. *J Clin Aesthet Dermatol* **5**, 44–47 (2012).

Appendix A

Supporting information for chapter 1.

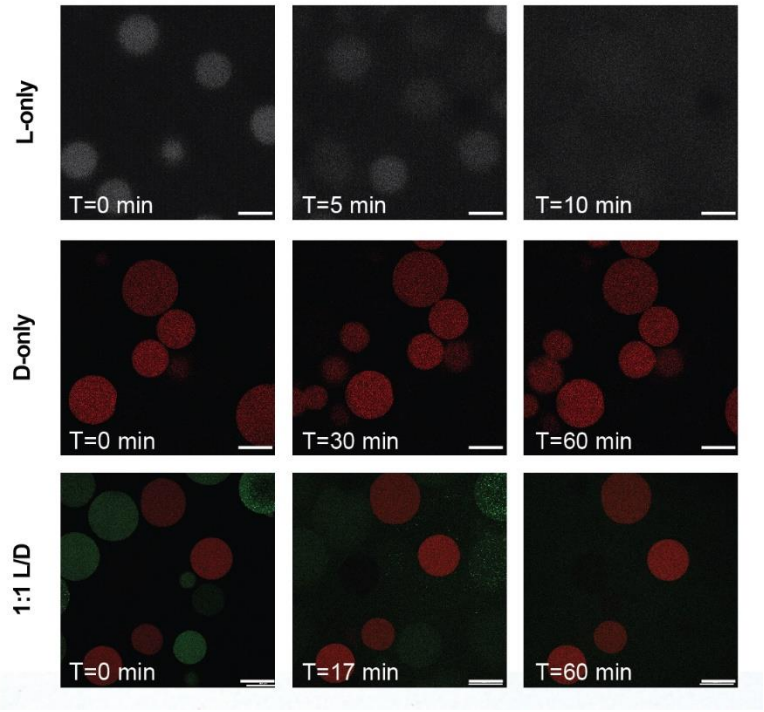

Figure A-1 In vitro characterization of L- and D- chiral microparticles and MAP hydrogel. Collagenase I degradation study of L, D and a 1:1 mixture of L and D microgels. As expected, L-peptide crosslinked microgels are degradable by collagenase I and are completely degraded by 60 minutes. I contrast D-peptide crosslinked microgels have no visible degradation within the 60-minute incubation in collagenase I. In a 1:1 mixture of L and D-peptide crosslinked microgels only L-peptide crosslinked microgels degrade. Images show representative examples of microscope images from in vitro hydrogel degradation of L, D, and 1:1 L/D-MAP. Scale = 200μm.

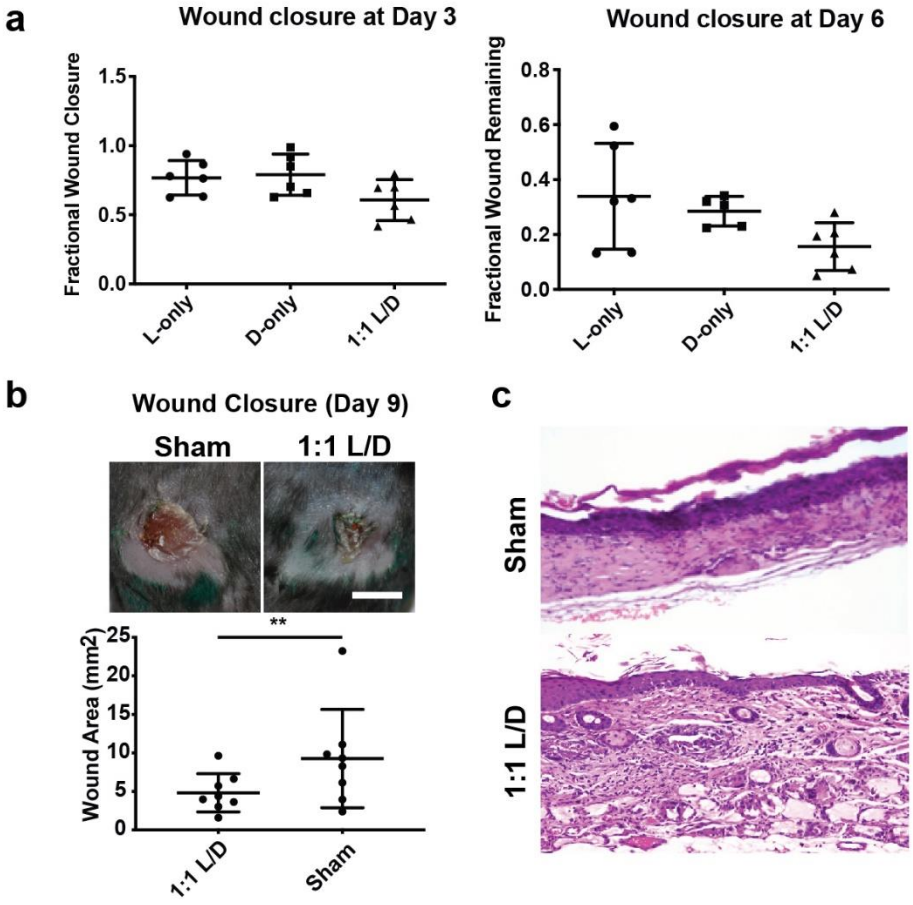

Figure A-2. Early wound closure results with different hydrogel treatments. a) No difference in wound closure between different L, D, and L/D MAP hydrogel treatment. n = 6 B6 mice, mean +/- SD. **b)** Comparison of L and D hydrogel to sham in B6 mice at day 9 reveals improved wound closure when compared to Sham. n = 8 B6 mice, mean +/- SD. Scale = 5mm. ** denotes two-tailed p=0.0078 by Wilcoxon matched pair signed rank test. **c)** 100x view of histology from SKH1 (hairless) mice 21 days after wounding demonstrating typical scar formation in sham mice (top) or vellus hair follicles and sebaceous glands directly over several degrading MAP gel particles in a mouse that was treated with D-MAP hydrogel.

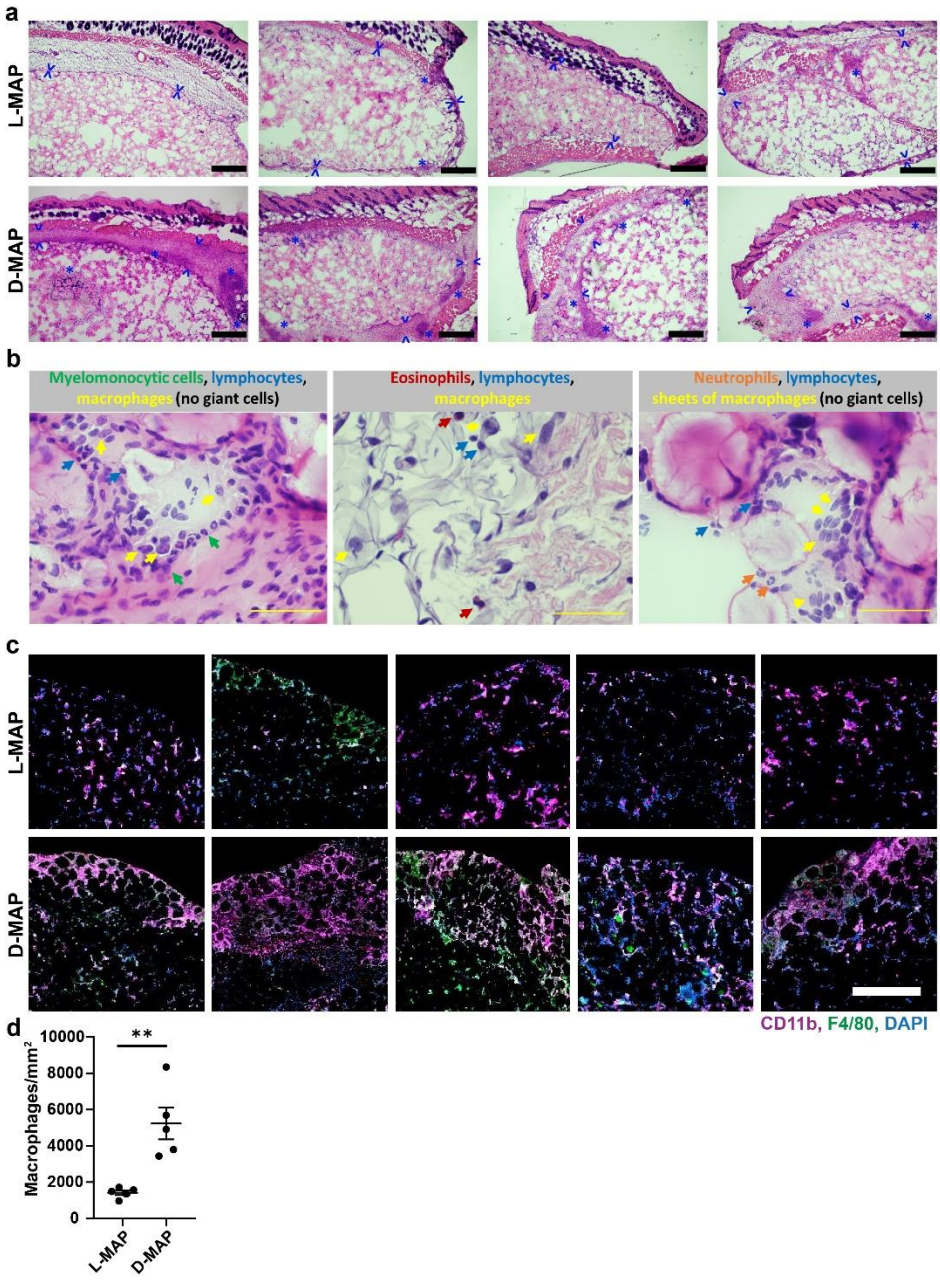

Figure A-3. Characterization of subcutaneous MAP implants. a) H&E staining of subcutaneous implants of L-MAP and D-MAP hydrogels. Arrowheads denote the expansion of the fibrous capsule with lymphohistiocytic cells and with admixed neutrophils and eosinophils. Asterisks denote foci of more robust inflammation. Note the minimal fibrous capsule and inflammatory response in L-MAP hydrogels compared to more robust response in D-MAP. Scale = 500μm **b)** Representative high-resolution H&E staining micrographs of subcutaneous D-MAP implants showing the macrophages, lymphocytes, and scattered eosinophils and neutrophils. Scale = 50 μm **c)** Immunofluorescence images from all subcutaneous implants of L-MAP and D-MAP hydrogels for F4/80 (green), CD11b (purple), IL-33 (red), and DAPI (blue). White to light pink denotes co-staining for F4/80 and CD11b antigens. Scale = 500 μm. (a) and (b,c) represent separate experiments. **d)** Quantification of $F4/80^{+}CD11b^{+}$ macrophages in the edge of L-MAP and D-MAP implants. ** denotes p=0.0025 on two-tailed unpaired T test. n = 5 B6 mice (whole hydrogels analysis), mean +/- SEM.

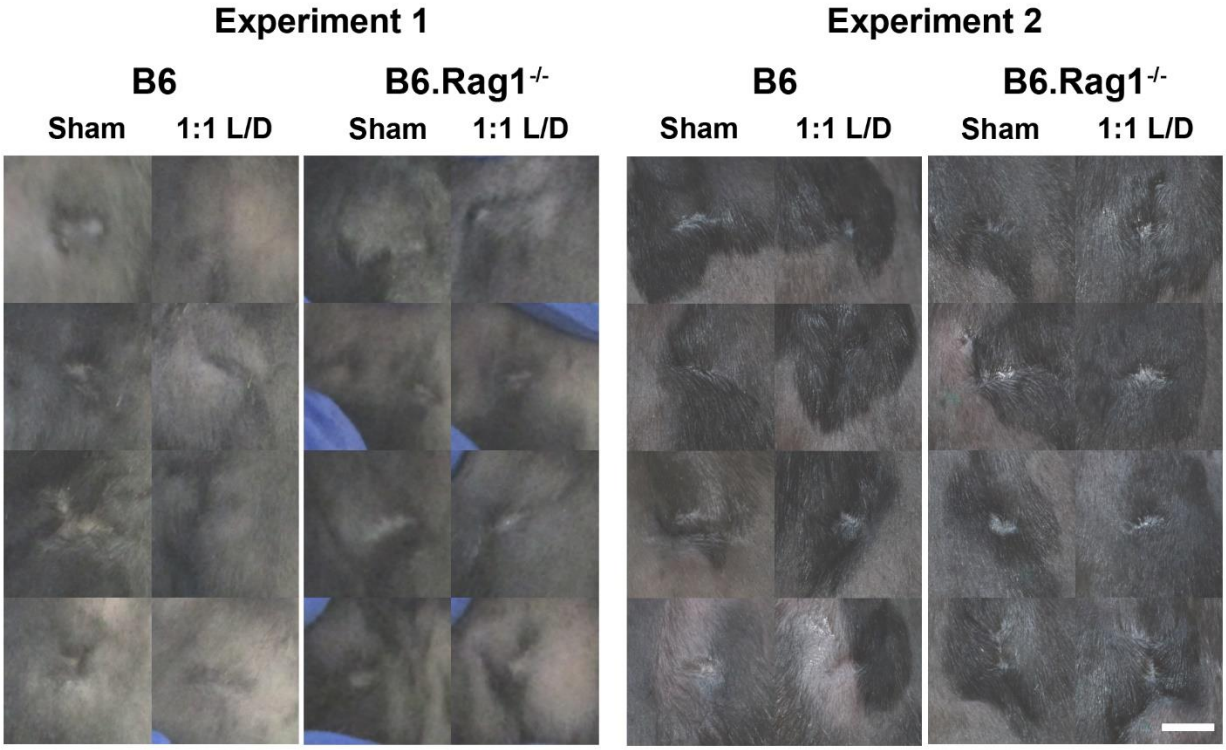

Figure A-4. L/D MAP hydrogel diminishes the clinical appearance of scar in WT mice but not B6.Rag1$^{-/-}$ mice. Splinted wounds (6mm) were performed on B6 or B6.Rag1$^{-/-}$ mice, and one side was treated with L/D MAP hydrogel and the other with no hydrogel. On Day 16, clinical photographs of wounds were taken. Shown are all healed wounds, paired by mouse, in two separate experiments. Scale = 2mm.

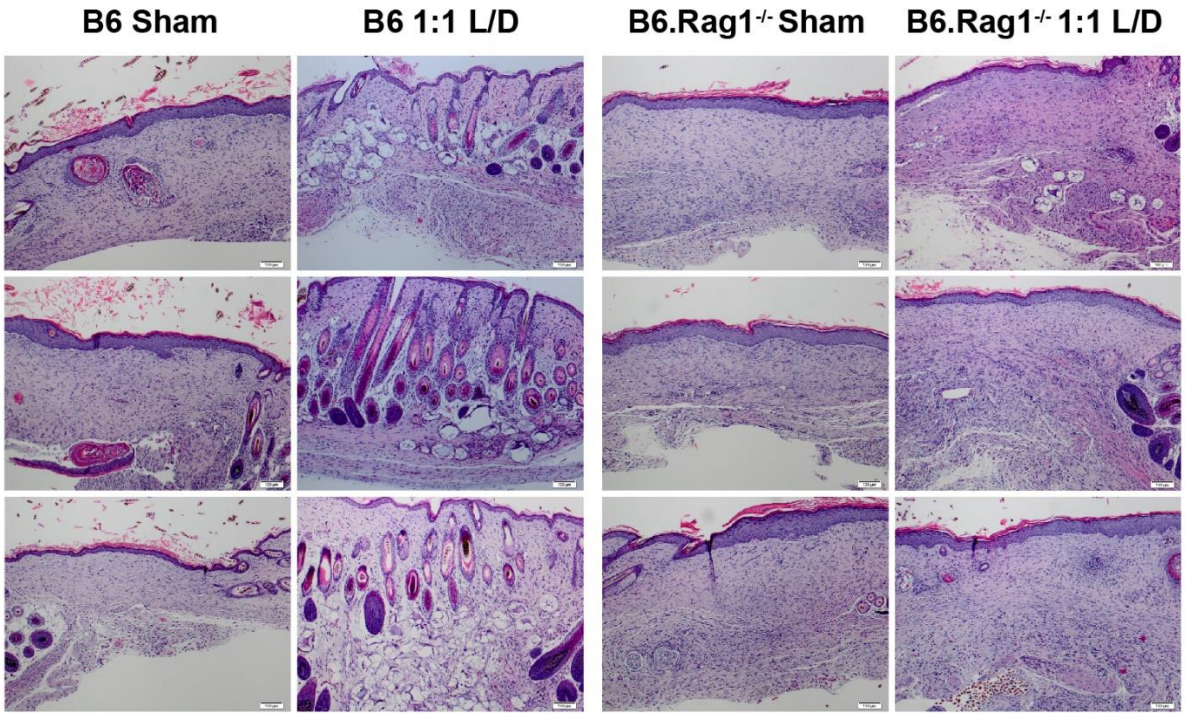

Figure A-5. Additional histology from healed 1:1 L/D-MAP or Sham treated wounds, B6 mice, and B6.Rag1$^{-/-}$ mice. Scale = 100μm. Note in the 1:1 L/D-MAP treated B6 samples, multiple hair follicles and some sebaceous glands, including some in disarrayed orientation compared to the surrounding tissue, are present directly overlying degrading microgels. Similar hair follicles are not present in any other group of samples. n = 3 per group shown.

Supplementary Discussion

To further characterize how D-MAP enhances innate immune recruitment, we evaluated histology of subcutaneous implants. After 21 days, L- or D-MAP implants were removed from the mice. As we previously demonstrated[56], most L-MAP implants did not display traditional fibrous capsule formation and only a few areas displayed some focal and thin fibrous capsules containing small foci of immune cells (**Figure A-3a**). No foreign body reaction with giant cells were noted within or surrounding the hydrogel, but some lymphohistiocytic immune infiltrates were seen dispersed randomly within and in areas towards the edge of the implant (**Figure A-3a**). This is likely a property of the porous nature of the MAP hydrogel allowing cells to migrate through the hydrogel rather than typical materials that allow a build-up of immune cells at the edges of the hydrogel. In contrast, D-MAP implants displayed thick fibrous capsules filled with mainly lymphohistiocytic cells and rare scattered neutrophils and eosinophils (**Figure A-3a-c**). Epithelioid histiocytes degrading hydrogel particles with scattered surrounding lymphocytes, and rare eosinophils and neutrophils were detected at the edges of the scaffold. Many more of these immune aggregates were found within D-MAP scaffolds than L-MAP scaffolds (denoted by *s in **Figure A-3a**). These findings are not consistent with a typical type 1 foreign body granuloma (no foreign body giant cells with sheaths of surrounding lymphocytes) associated with a strong Th1/M1 immune response seen in tuberculosis or with inflammatory materials. Instead, the material was eliciting a type II foreign body reaction typically associated inert foreign materials such as silicone[51,52,115]. Immunofluorescent staining for F4/80 and CD11b confirmed the increased presence of $F4/80^{+}CD11b^{+}$ macrophages within the D-MAP scaffolds at 21 days with concentrations at the edges of the hydrogel (**Figure A-3b** and **Figure A-3c**). These data suggest that D-MAP either possesses increased adjuvant properties by itself, or the MAP hydrogel itself

that is being amplified by the presence of D-chiral peptides or the MAP hydrogel possesses adjuvant properties, and the presence of D-chiral peptides induce an adaptive immune response that can dramatically amplify the immune response to the MAP hydrogel.

Appendix B

Supplementary info for chapter 3.

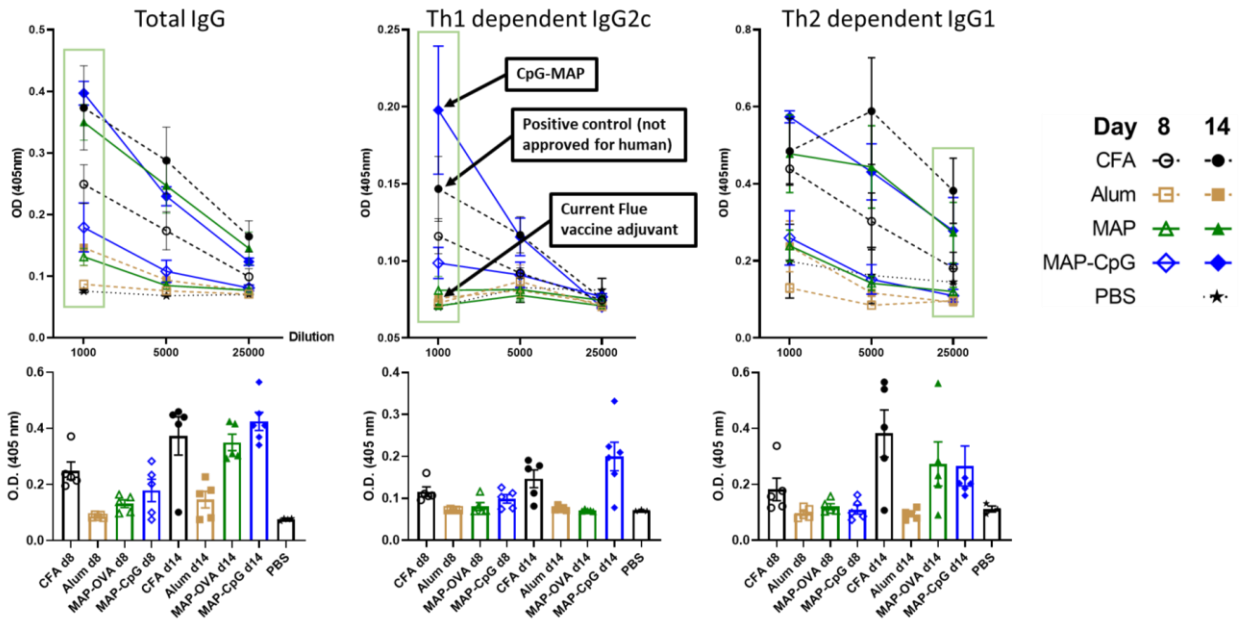

Figure 0-1. Comparison of MAP with different vaccination platforms in inducing NP-specific antibodies on day 8 and 14. Relative concentration of anti-NP IgG, IgG1, and IgG2c antibodies, in serum of B6 mice on day 8 and day 14 post vaccination with NP-OVA adjuvanted with MAP, MAP-CpG, using PBS, Alum, and CFA as controls. Total antibody concentration was determined by capture with NP(20)-BSA in ELISA. Each point represents the average of two technical replicated from one mouse.

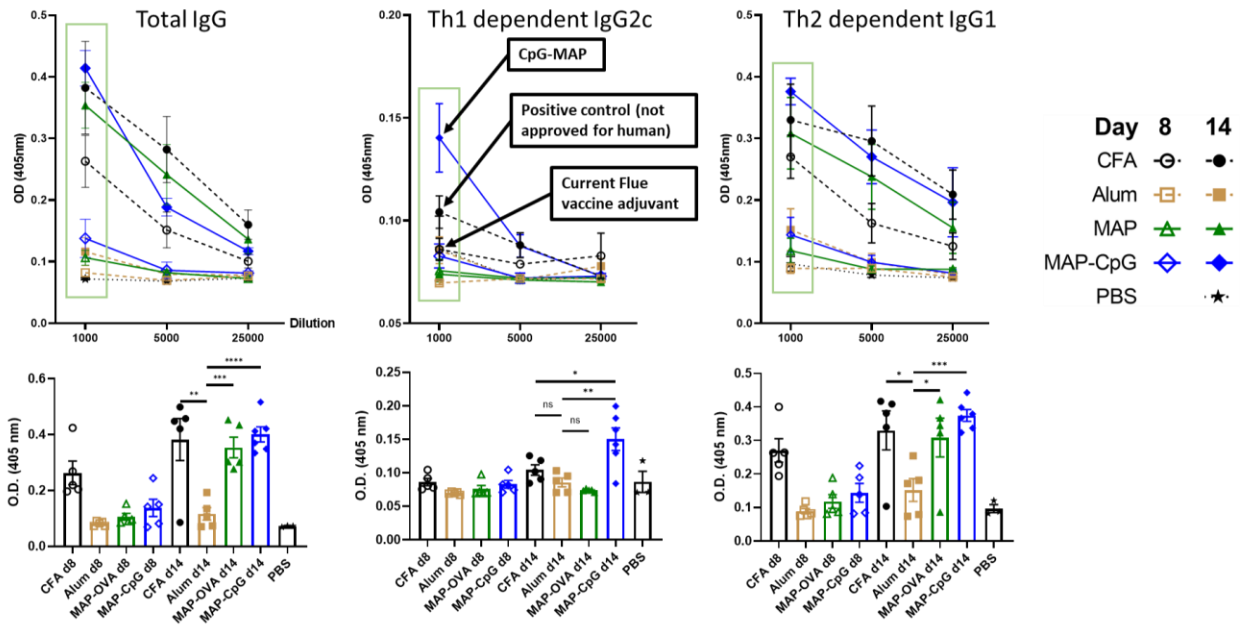

Figure 0-2. Comparison of MAP with different vaccination platforms in inducing high affinity NP-specific antibodies on day 8 and 14. Relative concentration of high affinity anti-NP IgG, IgG1, and IgG2c antibodies, in serum of B6 mice on day 8 and day 14 post vaccination with NP-OVA adjuvanted with MAP, MAP-CpG, using PBS, Alum, and CFA as controls. High affinity antibody concentration was determined by capture with NP(6)-BSA in ELISA. Each point represents the average of two technical replicated from one mouse.

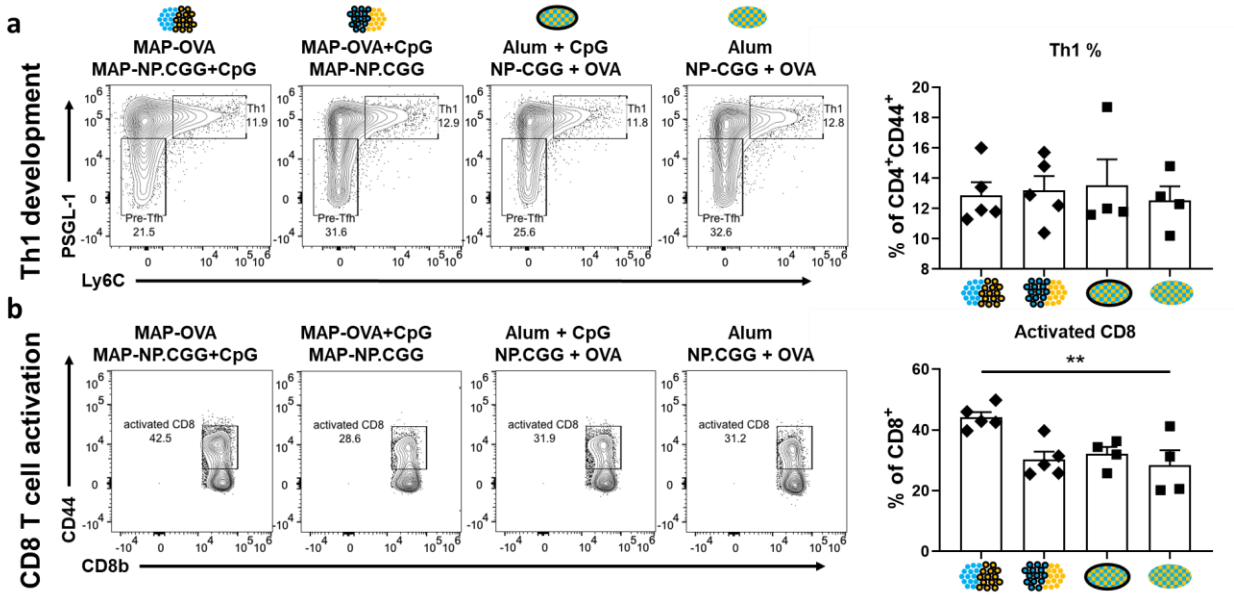

Figure 0-3. Characterization of Th1 dependent cellular response in B6 mice vaccinated with NP-CGG and OVA double antigen vaccine formulations on day 28. a-b) Representative flow cytometry plots (a) and quantification (b) of Th1 cells as a percent of $CD4^{+}CD44^{+}$ cells in spleen. c-d) Representative flow cytometry plots (c) and quantification (d) of activated CD8+ cells as a percent of total CD8+ cells in spleen.

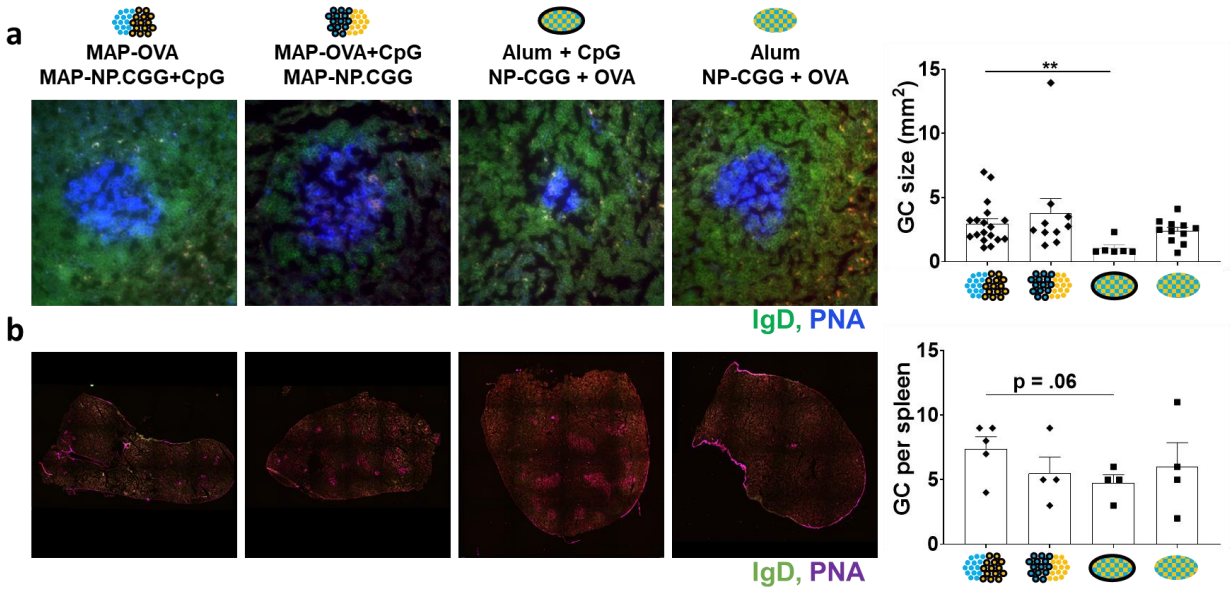

Figure 0-4. Histologic quantification of the germinal center reaction in the spleen of mice vaccinated with different double-antigen vaccine formulations. a) Representative high magnification image of the germinal centers, highly stained with peanut agglutinin (PNA), as well as the quantification of the germinal center sizes for each vaccine formulation. **b)** Representative low magnification images of the spleen sections showing the germinal centers with quantification of the number of germinal centers per spleen section in each vaccine formulation.

Appendix C

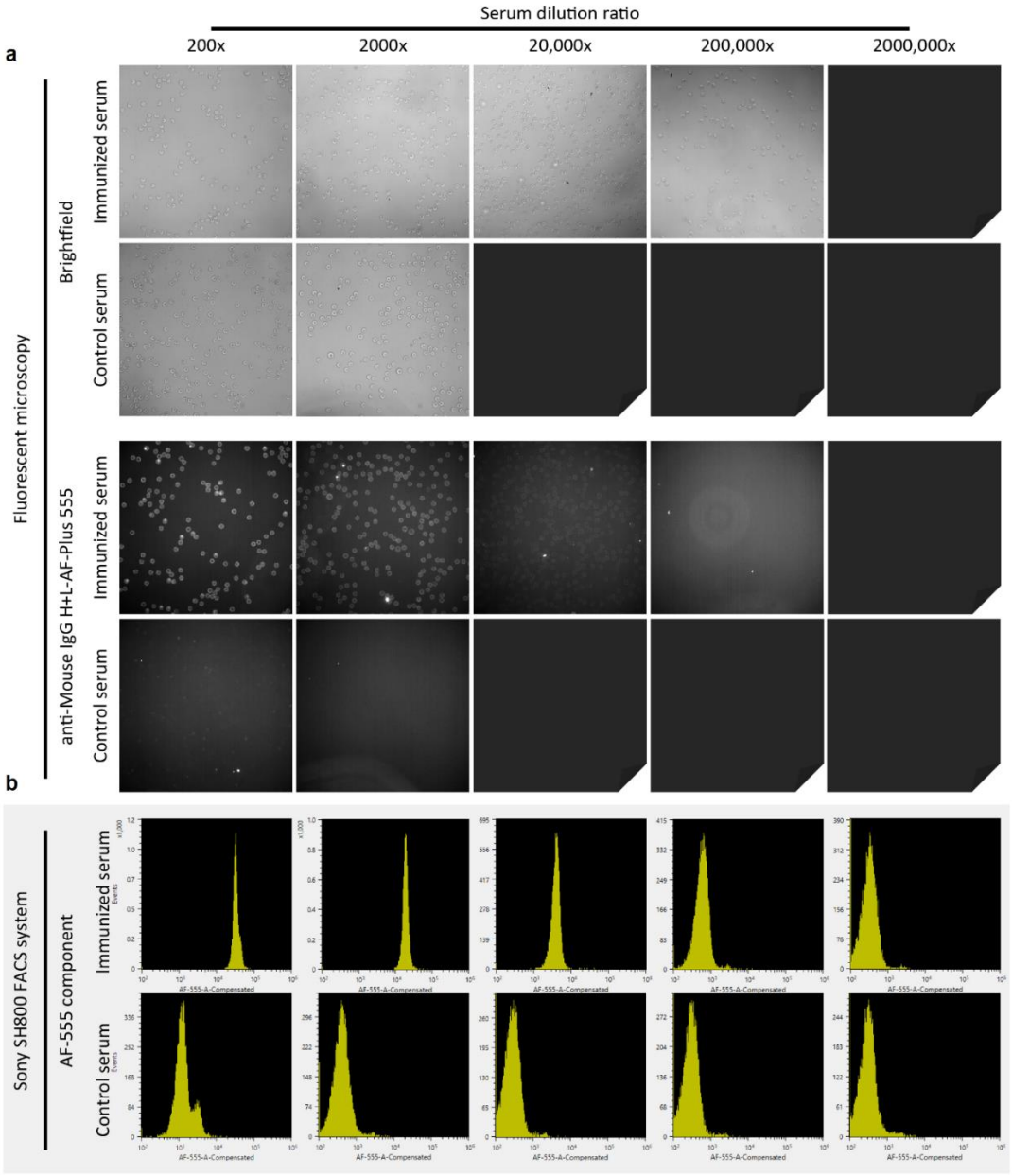

Figure C-1 Assessment of the dynamic range of nanovials for antigen specific capture and detection antibodies. Biotinylated OVA coated nanovials were incubated with serial dilutions of sera from OVA vaccinated and non-vaccinated mice and stained with Alexa Fluor Plus 555 conjugated anti-Mouse IgG H+L antibodies. (a) Nanovials can detect antigen specific antibodies in mice sera at titers down to 1:20,000. (b) Using Sony SH800 FACS system, the limit of detection of nanovials is extended to almost 1:200,000 titer, almost a ten-fold increase.

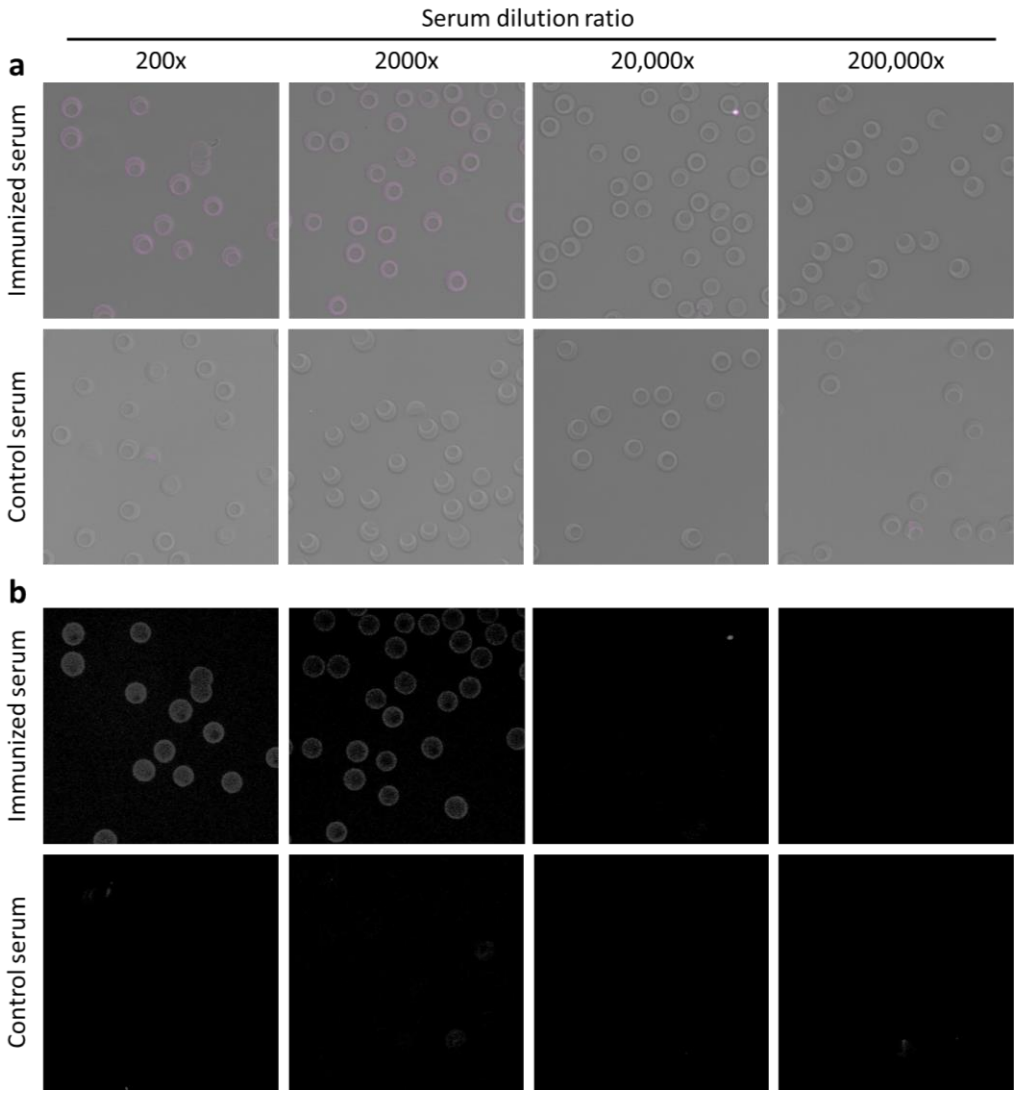

Figure C-2. Assessment of the dynamic range of nanovials for non-specific capture and antigen-specific detection of antibodies. Biotinylated anti-mouse IgG H+L antibody and biotinylated anti-mouse CD45 coated nanovials were incubated with serial dilutions of sera from OVA vaccinated and non-vaccinated mice and stained with Cy5-conjugated ovalbumin. a) Nanovials can detect antigen specific antibodies in mice sera at titers down to 1:2,000, showing no non-specific binding using fluorescent microscopy.

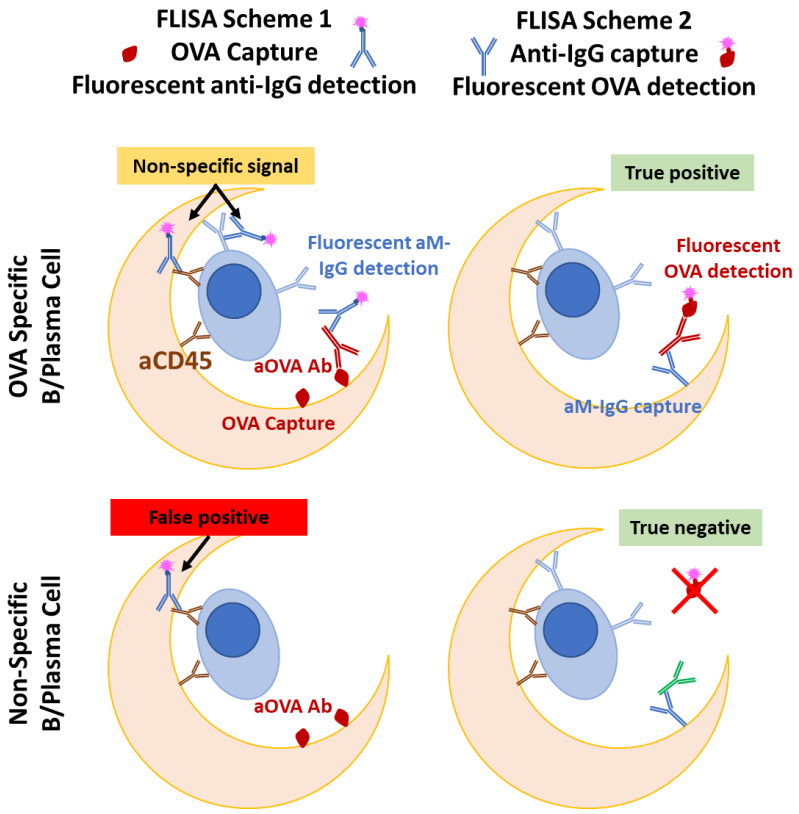

Figure 0-3 Schematic of two fluorescence-linked immunosorbent assay setups for antigen specific B/plasma cell detection. Scheme 1, while correctly identifying the positive signal, can lead to false positive signal from either cross-reactivity of detection antibody with cell capture antibodies or reaction with B cell receptors. Schematic two eliminates the chance of false positive from those unspecific or unintended bindings.